DTU Library

Electrochemical CO$_2$ Reduction to Two-Electron Products

Siig, Oliver Wischmann

Publication date:
2023

Document Version
Publisher's PDF, also known as Version of record

[Link back to DTU Orbit](#)

Citation (APA):
Siig, O. W. (2023). *Electrochemical CO$_2$ Reduction to Two-Electron Products.* Department of Physics, Technical University of Denmark.

Electrochemical CO$_2$ Reduction to Two-Electron Products

PhD Thesis
Oliver Wischmann Siig
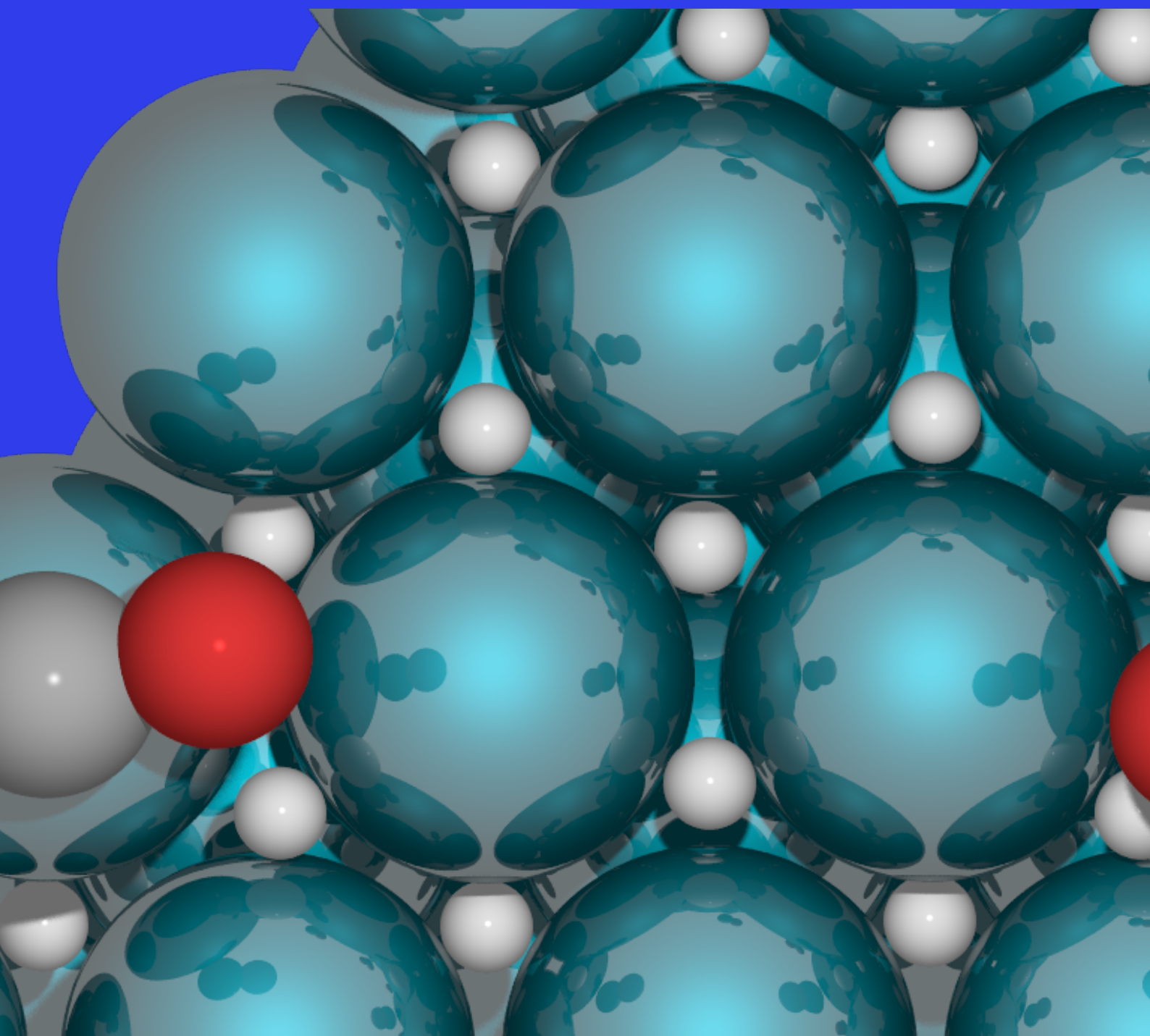
**Electrochemical CO$_2$ Reduction
to Two-Electron Products**

PhD Thesis
May, 2023

Author
Oliver Wischmann Siig

Supervisor
Professor Thomas Bligaard
Section for Atomic Scale Materials Modeling
Department of Energy Conversion and Storage
Technical University of Denmark
tbli@dtu.dk

Co-supervisor
Assistant Professor Georg Kastlunger
Catalysis Theory Center
Department of Physics
Technical University of Denmark
geokast@dtu.dk

Abstract

Climate change remains a major global challenge and with CO_2 emissions still increasing, a rapid transition towards renewables is required. Power-2-X and in this context electrochemical CO_2 reduction offers a promising solution to several issues related to this. First of all, it provides a means of storing excess energy from intermittent renewable energy sources in chemical bonds. At the same time, it also provides a viable synthesis route for the production of CO_2 neutral fuels we can use in our existing energy infrastructure. The technology still needs significant improvements both in terms of the activity and efficient use of the electrons supplied, but also in terms of improving selectivity towards desired products such as ethanol.

This thesis studies the formation of two-electron products in CO_2 reduction, to understand what guides the activity and selectivity on the different metals. We map out the selectivity for different metals and identify palladium as a clear outlier. In addition, Pd is able to produce both two-electron products with high selectivity and even switch between them across a quite narrow potential range, which makes it interesting to us as a fundamental study of what guides CO_2R product selectivity. We find that the entire Pd electrode undergoes structural changes in the presence of the electrochemical environment, forming a highly intercalated palladium hydride (PdH) structure. This changes the properties of the material and thus its ability to reduce CO_2. It has been proposed that the selectivity towards formate is driven by the *OCO binding motif, as opposed to *CO_2 driving CO production. This is not seen on PdH, instead formate is formed via a (surface) hydrogenation step. Furthermore, the electrochemical environment introduces strong differences in the driving forces between the two products, with the formate pathway initially being favored followed by a switch due to strong stabilization with potential of the CO pathway.

Next, we move on to take a more general look at the structural and environmental factors that affect the CO_2R activity. We construct a general model used to explore the possible CO_2 binding motifs. We distinguish the structural effects of chemical bonding through surface hybridization from the environmental effects of changing CO_2 binding through interactions between the electric field and the surface dipole. While the *OCO motif is initially destabilized by the field upon activation, ultimately both motifs benefit from the electric potential. The relative *OCO/*CO_2 stability becomes a competition between the hybridization/chemical bonding, which appears to favor *OCO on our model Cu(211) surface, and dipole-field interaction/-electrostatic effects, which favors *CO_2. Thus, given the right surface *OCO may become more stable even at slightly negative potentials. This was however not found to be the case for the post-transition metals known to produce formate.

Finally, as the other works of this thesis shows, the electric field is of paramount importance in CO_2 reduction, and with this in mind, we probe methods to intrinsically improve this. Specifically, we study whether curvature-induced field enhancements are large enough to drive the improved activity we observe. We find however, that the electric field effect is convoluted with structure changes in the most active systems. Ultimately, we find that the field enhancement associated with even high-curvature surfaces are negligible. Instead, we attribute the improved activity to increases in site density of step sites. The experimental data also verifies the theoretical hypothesis, that a region limited by *COOH formation exists at low overpotential, with a different potential response to that of CO_2 adsorption.

Resumé

Klimaforandringer er en global udfordring, og de stadigt stigende CO_2-emissioner, kræver en hurtig omlægning til vedvarende energi. Power-2-X og i denne sammenhæng elektrokemisk CO_2-reduktion er en lovende løsning på flere problemer relateret til dette. Først og fremmest er det et middel til at lagre overskydende energi fra vedvarende energikilder i kemiske bindinger. Samtidig er det også en levedygtig syntesevej til produktion af CO_2-neutrale brændstoffer, som kan bruges i vores eksisterende energiinfrastruktur. Der er dog stadig brug for væsentlige forbedringer både med hensyn til aktiviteten og til effektiv udnyttelse af de tilførte elektroner, men også mht. at forbedre selektiviteten imod ønskede produkter såsom ethanol.

Denne afhandling undersøger dannelsen af to-elektronprodukter i CO_2-reduktion for at forstå, hvad der styrer aktiviteten og selektiviteten på de forskellige metaller. Vi kortlægger selektiviteten for forskellige metaller og identificerer palladium som en klar outlier. Derudover er Pd i stand til at producere begge to-elektronprodukter med høj selektivitet og endda skifte mellem dem over et ganske snævert potentialområde. Det gør det fundamentalt interessant for os at undersøge, hvad der styrer CO_2R selektiviteten på Pd. Vi viser, at hele Pd-elektroden undergår strukturelle ændringer på i tilstædeværelsen af det elektrokemiske miljø og danner en stærkt interkaleret palladiumhydrid (PdH). Dette ændrer materialets egenskaber og dermed dets evne til at reducere CO_2. Det er blevet foreslået, at forskelle mellem *OCO og *CO_2 bindingsmotivernes stabilitet styrer selektiviteten mellem formiat og CO. Dette ses ikke på PdH, der i stedet danner formiat via et (overflade)-hydrogeneringstrin. Ydermere introducerer det elektrokemiske miljø stærke forskelle i drivkræfterne mellem de to produkter, hvor formiatvejen i første omgang favoriseres efterfulgt af et skifte på grund af stærk stabilisering med potentiale af CO-vejen.

Dernæst tager vi et mere generelt kig på de strukturelle og miljømæssige faktorer, der påvirker CO_2R-aktiviteten. Vi konstruerer en generel model, der bruges til at udforske de mulige CO_2 bindingsmotiver. Vi adskiller de strukturelle virkninger af kemisk binding gennem overfladehybridisering fra de miljømæssige virkninger af ændring af CO_2-binding gennem interaktioner mellem det elektriske felt og overfladedipolen. Mens *OCO-motivet først destabiliseres af feltet ved aktivering, drager begge motiver i sidste ende fordel af det elektriske potentiale. Den relative *OCO/-*CO_2-stabilitet bliver en konkurrence mellem hybridisering/kemisk binding, som ser ud til at favorisere *OCO på vores Cu(211) modeloverflade, og dipol-feltinteraktion/-elektrostatiske effekter, som favoriserer *CO_2. Givet den rigtige overflade kan *OCO således blive mere stabil selv ved svagt negative potentialer. Dette viste sig dog ikke at være tilfældet for de p-blok metaller, der producerer formiat.

Endelig, som de andre værker i denne afhandling viser, er det elektriske felt af afgørende betydning i CO_2-reduktion, og med dette i tankerne undersøger vi metoder til at forbedre dette. Specifikt undersøger vi, om krumningsinducerede feltforbedringer er store nok til at drive den forbedrede aktivitet, vi observerer. Vi konkluderer dog, at den elektriske felteffekt er blandet med strukturændringer i de mest aktive systemer. I sidste ende finder vi, at feltforstærkningen forbundet med selv højkrumningsoverflader er ubetydelig. I stedet tilskriver vi den forbedrede aktivitet til en stigning i tætheden af step sites. De eksperimentelle data verificerer også den teoretiske hypotese, at et område begrænset af *COOH-dannelse eksisterer ved lavt overpotentiale, med en anden potentialrespons end den for CO_2-adsorption.

Acknowledgements

This thesis is the result of roughly 3 and half year of working as a PhD student at CatTheory, DTU. Academia is a fast-paced and constantly changing field to work in, and I have crossed paths with a number of great people along the road.

First of all, I would like to thank my first supervisor Karen Chan, who took me in at CatTheory and was an immense source of knowledge and support throughout her time at DTU. I would also like to say a sincere thank you to my supervisor, Thomas Bligaard, for his mentorship and support throughout my project and for always being available and willing to share his vast knowledge. I also owe a special thanks to my co-supervisor Georg Kastlunger, who stepped into a more formal role along the road, but was there from the beginning, and I am grateful for his many good suggestions and invaluable input in our many scientific discussions.

In addition to the people I have worked with close at DTU, I also had the pleasure of working with several other groups around the globe. I want to thank Hong Li and Junyu Ge for our collaboration on electric fields and nanostructures, and the many interesting and thought-provoking discussions we have had over the course of the collaboration. I would also like to give a special thanks to Drew Higgins and Ahmed M. Abdellah for our very productive and intriguing collaboration in our palladium study.

I am also thrilled that I was able to complete my external stay at SLAC and Stanford with Frank Abild-Petersen and the rest of the theoretical group at SUNCAT. In-between pandemics and parental leave and what other obstacles thrown in, I am grateful for the fruitful collaboration and to Frank and the rest of the group for making me feel welcome and at-home in the group.

I would also like to thank all the many different people I have crossed paths with at CatTheory and for all the indespensible feedback I have received in countless group meetings and, just as importantly, over a cup of coffee in the lounge. I could mention all of you, but I would like to first and foremost thank Sudarshan Vijay for his many good inputs, countless discussions and for his participation and aid in our collaboration with the Hong Li group.

Finally, I would like to thank my family for their support and interest along the way. They have always encouraged me to believe in myself and follow that belief where ever it takes me and I am happy it took me here. And to the most understanding, supportive and loving, my wife Camilla Wischmann Siig, I am immensly grateful I had you with me every step along the way. I don't know what I should have done without you. Thank you.

Preface

This thesis is submitted in partial fulfillment of the degree of PhD at the Technical University of Denmark (DTU). The work of this thesis was carried out at the Catalysis Theory Center (CatTheory) at the Department of Phyics between the 1st of December 2019 and the 3rd of May 2023. The studies have been supervised by Karen Chan, Thomas Bligaard and Georg Kastlunger. The project received funding from VILLUM FONDEN for the VILLUM Center for the Science of Sustainable Fuels and Chemicals (V-SUSTAIN, grant 9455).

Oliver Wischmann Siig

....
Signature

May 3, 2023

....
Date

List of Publications

Paper I

In-Situ Liquid Phase Transmission Electron Microscopy and Electron Diffraction Provides Mechanistic Insight into Electrochemical CO2 Reduction on Palladium/Palladium Hydride Catalysts

Ahmed M. Abdellah, Fatma Ismail, Oliver W. Siig, Jie Yang, Carmen M Andrei, Liza-Anastasia DiCecco, Amirhossein Rakhsha, Kholoud E Salem, Kathryn Grandfield, Nabil Bassim, Robert Black, Georg Kastlunger, Leyla Soleymani, Drew Higgins

Submitted to Nature Materials

Paper II

Quantifying and Optimizing Electric Field Enhancement Effect on Carbon Dioxide Electroreduction

Junyu Ge[†], Oliver Wischmann Siig[†], Yang Yang, Liying Deng, See Wee Koh, Sudarshan Vijay, Manlin Luo, Xingli Wang, Donguk Nam, Georg Kastlunger, Hong Li
[†]*equal contribution*

To be submitted

Contents

Nomenclature

AFM   Atomic Force Microscopy

CHE   Computational Hydrogen Electrode

DFT   Density Functional Theory

DoS   Density of States

ECSA Electrochemical Surface Area

FD   Finite Difference

FE   Faradaic Efficiency

MEP   Minimum Energy Path

NEB   Nudge Elastic Band

PAW   Projector Augmented Wave

PCET Proton Coupled Electron Transfer

PDoS Projected Density of States

PES   Potential Energy Surface

PW   Plane Wave

PZC   Potential of Zero Charge

RHE   Reversible Hydrogen Electrode

SHE   Standard Hydrogen Electrode

SJM   Solvated Jellium Method

TOF   Turnover Frequency

TS   Transition State

List of Figures

List of Tables

Electrochemical CO$_2$ Reduction to Two-Electron Products

1 Introduction

1.1 Climate Change and Carbon Management

Climate change is one of the most pressing issues facing the world today. We are simply letting out more greenhouse gases than what our environment can sustainably handle, and it is affecting our climate globally. The problem has been well known and acknowledged for more than a generation [1], but the emission of CO_2 and other greenhouse gases continue to increase [2]. The Intergovernmental Panel on Climate Change (IPCC) estimated in 2021 that the global average temperature from 2011-2020 had already risen $1.1\,°C$ above the average temperature of the pre-industrial area (1850-1900) and that we have at least a 50% chance of reaching the $1.5\,°C$ set forth in the Paris Agreement in the near term (2021-2040) [3]. The changes in global mean temperature and atmospheric CO_2 concentration, shown in Figure 1.1, shows a rapid increase especially within the last 50 years and no significant slowdown seems to be taking place.
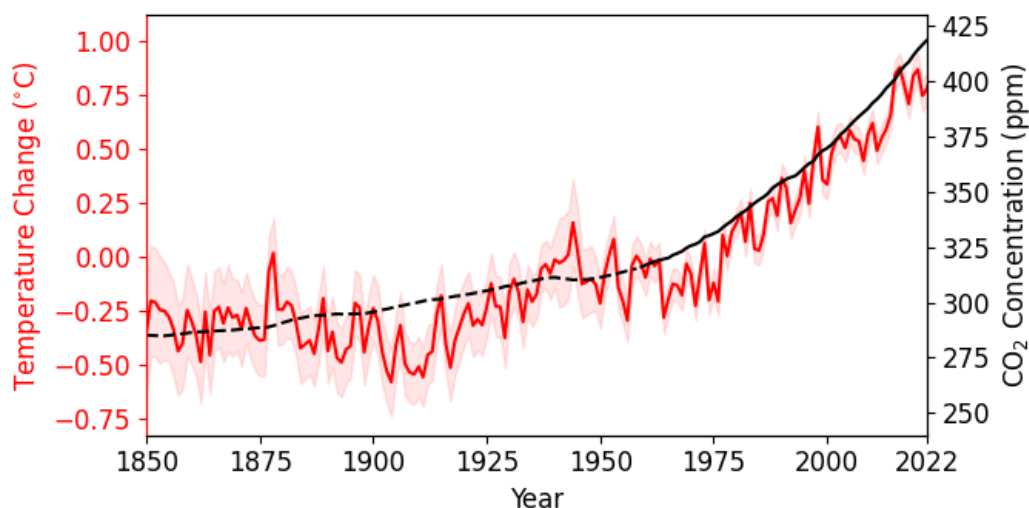
Figure 1.1: Variation in temperature and CO_2 concentration from 1850-2022

The data plotted in red is the mean annual temperature, with 97.5% confidence intervals, from 1850-2022 relative to the average temperature from 1961-1990 [4]. The black line is data for the mean annual CO_2 concentration from 1850-2022. The data shown with a dashed line (1850-1958) is concentration estimated from ice core measurements [5], while the data for 1959-2022, shown in solid black, are measurements from the Mauna Loa measurement station [6].

Nonetheless, it is paramount that this trend is reversed and swift action needs to be taken. The International Energy Agency has concluded that global CO_2 emissions must peak before 2025 and then rapidly decrease to 2030, and beyond to 2050 to maintain a chance to stay below the $1.5\,°C$ or even $2\,°C$ mark [7].

Now, if we look at where all this CO_2 comes from, there is one giant oily elephant in the room: The energy sector (including transport and energy emissions from manufacture and industry), which account for upwards of 70% of global emissions [8]. We are simply used to burning coal or gas to stay warm, drive our cars around on dead dinosaurs and burn off fossil fuels to heat up anything that builds nice things for us. And while there are mitigation strategies already in play for many of the energy-related emissions, there are also certain areas that are lacking behind.

1.2 Power-2-X: The Why and the How

That bring us to Power-2-X and why this a technology that has been identified by the IPCC [9], along with other methods of Carbon Capture and Storage, as one of the cornerstones in the transition towards a society based on renewables. While parts of the transport industry such as cars (and trains) have viable and popular electrified solutions, the heavy transport industry such as ships, aviation and to some extent trucking are not readily electrified. And it essentially boils down to some quite simple math. Let us take a step back and look at the combustion process that has served us well in internal combustion engines for generations, here for octane:

$$2\,C_8H_{18}(l) + 25\,O_2(g) \longrightarrow 16\,CO_2(g) + 18\,H_2O\,(g),\ \Delta H_r^\circ \approx 10.8\,\text{MJ/mol [10]}$$
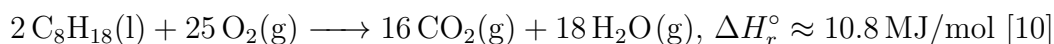
This is nice, give us a bit of oxygen and we can produce a fair bit of heat. Now, one of the advantages of our liquid hydrocarbons is that they have high energy densities, both volumetric and gravimetric. And if we take a closer look at the reactants above, we see why. The total mass of octane burned off in the reaction above is roughly $228\,\text{g/mol}$. The total mass of oxygen burned however is roughly $800\,\text{g/mol}$! And since we can just pull oxygen out of the air, this means we can save almost 80% in weight relative to a hypothetic fuel that did not get reactants from any external sources. If we compare this to a battery, we easily see why they are fundamentally different; in the case of the battery, we are constantly carrying around the entire cell, even when it's empty, and we are moving around essentially weightless electrons in a closed loop of heavy metals. If we compare the energy density of different fuels and batteries in Figure 1.2, the difference is striking; there is an almost two orders of magnitude difference between gasoline/diesel and the two battery types.

For cars, their low weight still make it doable to run on batteries, but a ship for instance would need to reserve a large part of its cargo space for the battery. For long-distance airplanes it is not even physically possible; for a plane flying a route from e.g. the US to Europe the required battery would be several times the entire weight of the plane. This is where Power-2-X becomes attractive. With Power-2-X we can take electrons generated from renewable energy sources such as wind and solar and store them in chemical bonds [14]. This could for instance be by converting CO_2 from a waste product to a fuel that we can then use in those situations where we really have no alternative [15], in a process that is overall CO_2 neutral after burning the fuel. Alternatively, we could use the electrons to turn nitrogen into the ammonia we need in large quantities for fertilizer production [16]. A process which is responsible for roughly 1.4% of the global energy consumption [17]. In either case, through Power-2-X we solve to complex challenges in the transition to renewable. First of all, we have a way to store excess energy, when the intermittent energy
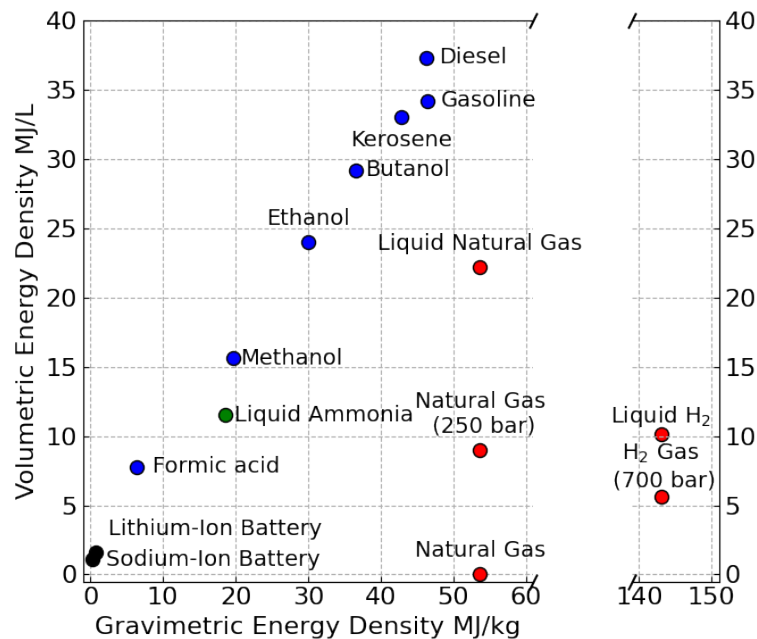
Figure 1.2: Energy densities for various fuels and batteries

Overview of the volumetric and gravimetric energy densities of various fuels and batteries (black). Fuels that are gas phase at 1 bar are colored red, liquid hydrocarbons blue and other liquid fuels green. Design courtesy of Scott Dial, data from **Thomas2000OverviewProgram**, [11]–[13].

source produces more energy than we need. Secondly, we can use the cheap/excess green energy to turn a low value or unwanted reactant into a valuable chemical and in addition to that, make an otherwise CO_2 heavy processes CO_2 neutral.

1.3 Electrochemical CO$_2$ Reduction

As outlined above, electrochemical CO_2 reduction offers a promising route towards mitigating two of the big challenges in our transition towards a society running on sustainable energy: Storing renewable energy from fluctuating energy sources such as wind and solar. And managing the carbon cycle by powering and supplying the sectors that currently rely on fossil resources, but are not readily electrified. The conversion of CO_2 takes place in an electrochemical cell, where CO_2 is reduced to lower oxidation-state products at a negatively charged cathode, while another species is oxidized in a different part of the electrochemical cell, at the positively charged cathode. In this thesis, we will focus on the half-cell reaction taking place at the cathode where CO_2 is being reduced. CO_2 can be reduced to a variety of different materials, depending on the metal, facet, potential and other reaction conditions. An overview of the product selectivity, show as Faradaic Efficieny (FE) of various metal cathodes according to Hori et al. [18] is given in Figure 1.3.

Figure 1.3: Periodic Table showing main product from CO_2RR

Selectivity is shown as FE at a given potential vs. RHE. The colors indicate main product, red is hydrogen, yellow is formate, purple is CO and turquoise is products beyond $2e^-$-reduction. Data is from Hori et. al [18], except for Au and Pd data which is from this thesis, given in Chapter 6 and 4 respectively.

For the two-electron products, the major chemical reactions are:

$$CO_2(g) + 2\,H^+(aq) + 2\,e^- \longrightarrow CO(g) + H_2O(l) \quad E^0 = -0.1\,V \text{ vs. RHE} \quad (1.3.1)$$

$$CO_2(g) + 2\,H^+(aq) + 2\,e^- \longrightarrow HCOOH(aq) \quad E^0 = -0.12\,V \text{ vs. RHE} \quad (1.3.2)$$

$$2\,H^+(aq) + 2\,e^- \longrightarrow H_2(g) \quad E^0 = 0.0\,V \text{ vs. RHE} \quad (1.3.3)$$
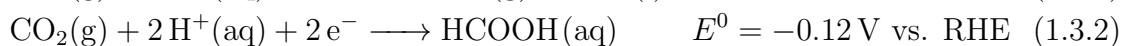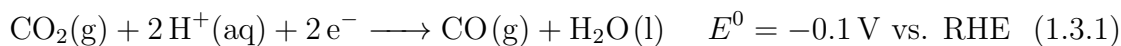
For the formation of CO, formic acid and hydrogen respectively, showing the equilibrium potential of each reaction, taken from [19]. $E^0 = 0.0$ V vs. the Reversible Hydrogen Electrode (RHE) for hydrogen formation at any pH by definition. At potentials below the equilibrium potential, the reaction is in theory spontaneous, although kinetic barriers often mean we have to apply an overpotential η against E^0 for the reaction to occur. Finally, it should be noted that at $pH > pK_{a,HCOOH} = 3.75$ the product in reaction (1.3.2) will be formate ($HCOO^-$) rather than formic acid and that the products beyond $2e^-$ are expected to pass through *CO as an intermediate, making formate/formic acid the final product of that reaction electrochemically [20].

1.4   Outline of Thesis

In this thesis, we study the electrochemical reduction of CO_2 to two-electron products, CO and formate/formic acid that is. We begin by describing the theoretical foundations for our main computational tool; Density Functional Theory (DFT) and the steps we need to take to obtain kinetics, in Chapter 2, along with the methods used in this thesis and the specific computational details.

Next, in Chapter 3 we go more in depth with the details of the electrochemical environment and what distinguishes it from a heterogeneous solid/gas interface and how we can take advantage of that. Additionally, we describe how to model the electrochemical environment, what models we have available and what the trade-offs are between the models.

In Chapter 4 we study how the electrochemical environment affect the CO_2 Reduction on Pd. We find that the reactivity is related to structural changes of the Pd

Electrochemical CO_2 Reduction to Two-Electron Products

electrode itself, and that the product distribution from CO_2R is highly dependent on the environment and particularly the ability of the electrochemical environment to promote competeting steps.

Chapter 5 focuses more broadly on the structural and environmental factors that impact CO_2R activity as well as activity. We construct a model used to explore the possible CO_2 binding motifs, and show how we can qualitatively decouple the structural/chemical effects from the environmental/electrochemical effects. Finally we conclude that the *OCO intermediate is unlikely to be stable enough to participate in CO_2R on copper, and likely even more oxophilic metals.

Finally, in Chapter 6 we probe methods to intrinsically improve one of the key activity drivers in electrochemical CO_2 Reduction; the electric field. Specifically, we study whether curvature-induced field enhancements are large enough to drive improved activity observed. We find however, that the electric field enhancement associated with even high-curvature surfaces are negligible. Instead we attribute the improved activity to increases in site density of step sites.

2 Theory & Methods

2.1 Density Functional Theory

The foundation of our computational modeling of atomistic systems the Density Functional Theory (DFT). DFT is derived from fundamental quantum mechanical theories, with some important approximations. One of the fundamental variables in the framework is the *electronic wavefunction*. The wavefunction is able to fully describe the electrostatics as well as the dynamics of a state of a given system/particle. The wavefunction plays a central role in a number of the most fundamental equations of quantum mechanics, among these perhaps one of the most fundamental off all, the *Time-Independent Schrödinger Equation* (TISE), initially proposed by Erwin Schrödinger in 1926. For a single particle in a 3-dimensional system, TISE is essentially an eigenvalue problem given in cartesian coordinates as:

$$-\frac{\hbar^2}{2m}\nabla^2\psi + V(x,y,z)\psi = E\psi \tag{2.1.1}$$

Where V is the potential energy, $\hbar$ is the Planck constant (h) divided by 2π while m is the particle mass. ψ is the particle *wavefunction*, describing the state of the system with E being the energy associated with the state ψ. ∇^2 is the Laplacian operator, given in cartesian coordinates as:

$$\nabla^2 = \frac{\partial^2}{\partial x^2} + \frac{\partial^2}{\partial y^2} + \frac{\partial^2}{\partial z^2} \tag{2.1.2}$$

If we consider a system of N particles and i different states, we can write the TISE a given eigenstate (wavefunction, ψ_i) and eigenvalue (energy, E_i):

$$\hat{H}\psi_i\left(\vec{x}_1, ..., \vec{x}_N\right) = E_i\psi_i\left(\vec{x}_1, ..., \vec{x}_N\right) \tag{2.1.3}$$

Where $\vec{x}_i$ is a vector of the coordinates of particle i, ψ_i is thus a function of all positions of all particles through $\vec{x}_1, ..., \vec{x}_N$ and E_i the energy of that exact state ψ_i. $\hat{H}$ is the total energy operator, known as the Hamilton operator, which changes (or can be written in different ways) depending on the system. For a molecule with no external field containing M nuclei and n electrons $\hat{H}$, given in a.u.[1], becomes [21]:

$$\hat{H} = -\frac{1}{2}\sum_{p=1}^{N}\nabla_p^2 - \frac{1}{2}\sum_{A=1}^{N}\frac{1}{m_A}\nabla_A^2$$

$$-\sum_{p=1}^{N}\sum_{A=1}^{M}\frac{Z_A}{|\vec{r}_p - \vec{R}_A|} + \sum_{p=1}^{N}\sum_{q>p}^{N}\frac{1}{|\vec{r}_p - \vec{r}_q|} + \sum_{A=1}^{M}\sum_{B>A}^{M}\frac{Z_A Z_B}{|\vec{R}_A - \vec{R}_B|}$$

$$\Downarrow$$

$$\hat{H} = \hat{T}_{elec}(\vec{r}) + \hat{T}_{nuc}(\vec{R}) + \hat{V}_{ext}(\vec{r}, \vec{R}) + \hat{V}_{elec}(\vec{r}) + \hat{V}_{nuc}(\vec{R}) \tag{2.1.4}$$

---

[1]Setting $\hbar = m_e = e = 1$, where m_e is electron mass and e is elementary charge.

Capital letters (A,B) and subscripts are used for nuclei and lowercase letters (p,q) and subscripts are used for electrons. m_A and Z_A is the mass, respectively the number of protons in nuclei A. $\vec{r}_k/\vec{R}_K$ are coordinate vectors of electrons and nuclei. The first two terms are terms for the classical kinetic energy for electrons and nuclei respectively, denoted $\hat{T}$. The final 3 terms are interaction potentials of coulombic repulsion or attraction between electron/nuclei, electron/electron and nuclei/nuclei respectively, denoted $\hat{V}$. Except for the third term, these terms are either unique determined by the positions of either the electrons or the nuclei. The third term is then a measure of the interactions between electrons and nuclei and, from the perspective of either the nuclei or the electrons separately, the only term that couples the *internal* energy of either of the two, to variables external to either the electrons or nuclei, namely the position of the other particles. We thus denote it $\hat{V}_{ext}$. As the Hamiltonian is written above, it is a many-body problem that almost immediately becomes impossible to find exact solutions for. This is in fact the case for any systems larger than the hydrogen atom.

A common approach is simplify the many-body problem is through the *Born-Oppenheimer approximation*, which assumes that the positions of the nuclei is independent of the movement of the electrons [22]. The assumption here, is that the electrons can be seen as mass-less relative to the nuclei. I.e., when the electrons move around, their *movement* does not affect the positions of the nuclei[2]. As a consequence, $\hat{V}_{ext}$ is now only a function of $\vec{r}$, while $\vec{R}$ is now merely a parameter in $\hat{V}_{ext}$. This is also the reasoning behind the 'ext'-notion; looking only at the electronic system, the nuclei appear in the equation merely as a constant field of fixed charges. Additionally, these are the only parameters external to the electronic contributions to the total energy of the system as $\hat{T}_{elec}$ and $\hat{V}_{elec}$ are only a function of $\vec{r}$.:

$$\hat{H} = \hat{H}_{elec}(\vec{r}; \vec{R}) + \hat{H}_{nuc}(\vec{R}) \tag{2.1.5}$$

$$\hat{H}_{elec}(\vec{r}; \vec{R}) = \hat{T}_{elec}(\vec{r}) + \hat{V}_{ext}(\vec{r}; \vec{R}) + \hat{V}_{elec}(\vec{r}) \tag{2.1.6}$$

$$\hat{H}_{nuc}(\vec{R}) = +\hat{T}_{nuc}(\vec{R}) + \hat{V}_{nuc}(\vec{R}) \tag{2.1.7}$$

Where we have left out the subscript 'i', but it is still implicitly assumed that this holds for any eigenfunction ψ_i and eigenstate E_i. Similarly, we split the wavefunction into two separate parts, the electronic and the nuclear wavefunction, with the total wavefunction being a product of the two, and the former taking $\vec{R}$ as a parameter in $\hat{V}_{ext}$:

$$\psi(\vec{r}, \vec{R}) = \psi_{elec}(\vec{r}; \vec{R}) \cdot \psi_{nuc}(\vec{R}) \tag{2.1.8}$$

Inserting this into (2.1.3), dividing both sides by the (RHS of) eq. (2.1.8) and subtracting the nuclear contribution gives:

$$\frac{\hat{H}_{elec}(\vec{r}; \vec{R})\psi_{elec}(\vec{r}; \vec{R})}{\psi_{elec}(\vec{r}; \vec{R})} = E - \frac{\hat{H}_{nuc}(\vec{R})\psi_{nuc}(\vec{R})}{\psi_{nuc}(\vec{R})} \tag{2.1.9}$$

---

[2]The electron *positions* still affects the nuclei positions, but we've effectively decoupled the nuclei positions from the dynamics of the moving electrons and now only depend on the electrostatics.

The RHS is only a function of $\vec{R}$, and we let this equal $\varepsilon(\vec{R})$, which is essentially a constant from the perspective of the electronic Hamiltonian:

$$\frac{\hat{H}_{elec}(r; \vec{R})\psi_{elec}(\vec{r}; \vec{R})}{\psi_{elec}(\vec{r}; \vec{R})} = \varepsilon(\vec{R}) \tag{2.1.10}$$

$$\hat{H}_{elec}(r; \vec{R})\psi_{elec}(\vec{r}; \vec{R}) = \varepsilon(\vec{R})\psi_{elec}(\vec{r}; \vec{R}) \tag{2.1.11}$$

Essentially reproducing the TISE, but with $\hat{H}_{elec}$ as the Hamiltonian operator for the electronic energies, ψ_{elec} for the electronic eigenstates and $\varepsilon(\vec{R})$ for the eigenvalues for the electronic energy.

Setting the RHS equal to the same $\varepsilon(\vec{R})$, now a function $\vec{R}$ the total energy can be found:

$$E - \frac{\hat{H}_{nuc}(\vec{R})\psi_{nuc}(\vec{R})}{\psi_{nuc}(\vec{R})} = \varepsilon(\vec{R}) \tag{2.1.12}$$

$$\left(\hat{H}_{nuc}(\vec{R}) + \varepsilon(\vec{R})\right)\psi_{nuc}(\vec{R}) = E\psi_{nuc}(\vec{R}) \tag{2.1.13}$$

Comparing eq. (2.1.13) to eq. (2.1.1), we see that electronic energy $\varepsilon(\vec{R})$ essentially acts as a potential energy surface to the nuclear Hamiltonian, adjusting its value as the nuclei move around. This decoupling of the electron and the nuclei movements is what form the basis of the iterative 3-step solving approach employed in molecular modelling; (1) the electronic Schrödinger equation is solved for a fixed set of nuclei, (2) this gives an electronic energy $\varepsilon(\vec{R})$ which is then used to (3) solve for the nuclear positions and total energy before loading the coordinates into (1). This loop goes on according to some optimization scheme until convergence is reached by satisfying certain criteria.

However, in order to solve the electronic Schrödinger equation given in (2.1.6), we of course have to evaluate the separate terms. Of the three terms in $\hat{H}_{elec}$ only V_{ext} is system specific as it contains information about the nuclei with the parameters Z_A and $\vec{R}_A$. The remaining two are universal; distributing equal and indistinguishable particles across a volume, maximizing kinetic energy and minimizing charge repulsion. Unfortunately, the wavefunction itself does not correspond to any physical quantity we can measure in any traditional sense. However, following the Born Interpretation, we can get the *probability density* of the particle from the square modulus of the wavefunction, $|\psi^2|$. And if we integrate over a volume $d\tau$ gives the probability of finding the particle in this volume [23]. The first Hohenberg-Kohn Theorem proved that V_{ext} can be uniquely determined by the ground state of this electron density, $\rho_0(\vec{r})$ and that V_{ext} uniquely determines $\hat{H}_{elec}$ [24]. The electron density is proportional to the probability density integrated over all possible spins and the coordinates of all but one of the electrons, corresponding to the probability of finding electron 'i' within the volume element $d\vec{r}_i$. As the electrons are indistinguishable, N times this value gives the probability of finding *any* of N electrons with the volume element $d\vec{r}_i$, thus reducing the 3N variables of the wavefunction to just 3 for the electron density. In addition to the description of $\hat{H}_{elec}$ from V_{ext}, an energy

minimization functional was proposed [25]:

$$E_0[\rho_0] = \int \rho_0 V_{ext} \, \mathrm{d}r + F[\rho_0] \qquad (2.1.14)$$

Which specifies a functional $F[\rho]$ that searches for the ground state electron density by minimizing the two part of the electronic Hamiltonian, $\hat{T}_{elec}$ and $\hat{V}_{elec}$, that are not system specific (i.e. dependent on the nuclei/V_{ext}. While this still does not have any exact solution, the Kohn-Sham Equations split $F[\rho]$ into 3 terms [26]:

$$F[\rho] = T_S[\rho] + J[\rho] + E_{XC}[\rho] \qquad (2.1.15)$$

With $T_S[\rho]$ defined as the kinetic energy of a non-interacting system, $J[\rho]$ being the electron-electron Coulomb interaction and $E_{XC}[\rho]$ simply being an umbrella or a garbage can collecting all of the errors made in the assumptions about the classical behavior of the kinetic and electrostatic energy. Of these three, the former two are trivial to solve, while the latter contains a number of tricky non-classical effects such as electron exchange and correlation effects and self-interaction. While (2.1.15) is in theory an exact solution using the coordinates of just one single particle, and could potentially lead us to the true ground state energy, $E_{XC}[\rho]$ is unknown and must be approximated. It is the approximation of this term, often split into separate approximations of exchange and correlation effects, that has led to the design of a wide variety of competing and complimentary functionals.

2.1.1 Application of DFT

In order to utilize DFT in an efficient and meaningful manner we have to take a number of decisions that are often a choice between the efficiency of the calculation and the accuracy. One of the choices with the largest impact is the choice of the exchange and correlation functional(s).

It is important to be aware of the design choices made, often choosing between efficiency and accuracy. One of the most significant choices is the choice of the exchange and correlation functional(s). Generally we can group them into five different levels of increasing sophistication and accuracy, but also computational costs, according to the so-called Jacob's ladder [27]. The levels range from simply using the electron density, $\rho(\vec{r})$ directly, at given positions (Local Density Approximation), over models that also incorporate the first derivative of the density, $\nabla \rho(\vec{r})$ to methods that include full expressions for the exchange energy ('exact exchange') and unoccupied orbitals. This report uses functionals from the second rung of the Jacob's ladder for computational efficiency.

Additionally, two general approaches to functional design exists, regardless of the level of sophistication. One approach is to simplify the calculations and functionals by imposing constraints on the exact density functional based on the laws of physics and analytical observations. The PBE functional [28], coined 'the first parameter-free GGA' and its revisions [29], [30] are notable examples of this approach. Alternatively, we can parameterize one or more of the variables, fit the functional to perform well against one or a number of different data sets with relevant properties in such as structural or energetic data. Usually a subset of data from a specific

category, thus optimizing the functional to perform well withing a given area of chemistry. A famous or, according to some, infamous example of this is the class of Minnesota Functionals, which are fitted to upwards of 60 different parameters [31].

An example of a parameterized functional often used in catalysis is the BEEF-vdW functional. The functional uses test data sets involving energies of reaction and formation of molecules, including barriers, chemisorption energies on solids in addition to solid state properties of e.g. the bulk and surface. These are fitted to number of Legendre Polynomials to construct the functional [32]. Another important feature of this functional is that is includes van der Waals dispersion interactions which is crucial in describing the stability of large molecules in particular, near or on a surface. Finally, the search for functionals produces an entire ensemble of functionals that are minimized according to a cost-function, which selects the best functional. This will additionally produce range of different functionals with errors that are close to the errors of the chosen functional and thus should yield similar energetics. By comparing the energy difference of two states, that we get with the functional selected as the best, to energy differences estimated from the "next-best" choices, we get an estimate of how well the states are described by the BEEF-vdW functional, known as a *Bayesian Error Estimate* [33]. The BEEF-vdW functional is used throughout this report.

2.2 GPAW - Using the DFT Calculator

For this project, we use the open source GPAW grid-based DFT code based on the Projector-Augmented Wave method [34], to perform our computational catalysis, in some cases along with the Solvated Jellium Method (SJM) described in depth in Chapter 3. The full details of the parameters etc. used in the computations is given in Section 2.5.

When performing DFT calculations, we have to make a number of choices in addition to the functional discussed in Section 2.1.1. Another important choice is how we expand the wavefunctions. The wavefunctions have a large spatial variation in shape, depending on whether they are close to the nucleus, where oscillations and nodal points appear, or further away from the nucleus where their profile is much smoother until they vanish. This makes it a challenge to model them in a simple way, when we expand them onto a basis set. With GPAW, we can treat the wavefunction in a number of different ways:

LCAO The first model is the well known Linear Combination of Atomic Orbitals (LCAO). With this, we simply have a assembly of localized atoms orbitals, known as a *basis set*, that we can expand the wavefunction onto. And we can vary these basis sets in size with varying levels of sophistication. As an initial approximation these 3 methods all rely on basis sets to describe the wavefunction and these atomic orbitals then describe and predict a chemical bond between atoms through tail overlaps of the wavefunction. Naturally, the basis set approach will then struggle to account for delocalized effects and long-range interactions such as van der Waals forces. In GPAW the LCAO model is implemented as a crude model, used to get faster but less accurate results. This is possible because it uses relatively small basis sets in comparison the

FD and PW modes [35].

FD The finite difference (FD) approach expands the wavefunctions onto a 3D real-space grid, essentially giving us a large number of different points on this large grid separated by a constant spacing, and we can then evaluate the wavefunctions numerically at each grid point. It is coined the finite difference method because the mode uses the finite difference method for a given points and a number of the points surrounding it to calculate non-local behavior, as for instance the gradient introduced in the non-interacting kinetic energy. The number of basis sets we have available can either be set by providing a value for the grid spacing or we can directly give the number of grid points we want. The model is design for the calculations to be efficiently parallelized over several CPU's, since it, in contrast to the PW method below, saves the Fourier transform required by this method, by evaluating the functions on a real-space grid [34].

PW The final method is the Plane Wave (PW). Here, we expand the wavefunction onto a number of plane waves, given as $\vec{G} \exp^{i\vec{G}\vec{r}}$, where $\vec{G}$ is a reciprocal lattice vector of the unit cell. The number of basis functions is chosen through an energy restriction, E_{cut}, on $\vec{G}$, given as $\frac{1}{2} \left| \vec{G} \right|^2 < E_{cut}$.

For all 3 methods though, the true wavefunction is still either prohibitively expensive to describe very close to the nuclei, or we fail to fully include the long-range interactions of the system. To account for this, so-called *pseudopotentials* are used, where the atomic nuclei are regarded as perturbations of a free electron gas. These are good at representing the smooth, long range as well as the bonding parts of the wavefunction quite well but they often struggle to reproduce the correct shape, and in some cases even size of the wavefunction, close to the nuclei [36]. The *Projector-Augmented Wave* (PAW) is an approach to link the two complimentary descriptions of the wavefunction. It uses a *frozen core* approach, where we fix the core shapes around the nuclei to reference shapes found from atomic orbitals. Next, we design a basis set of smooth wavefunction, i.e. the pseudopotentials, and expand the all-electron wavefunctions onto these through a linear transformation. We run our numerical calculation and finally transform the pseudopotentials back to the all-electron wavefunctions. This approach usually works quite well, since the core electrons very seldom get involved in chemical bonding or charge transfer, rather this usually only involves the valence electrons or electrons from the next outer-most shell. This report mainly uses the FD-method for high-accuracy calculations that parallelize well. The PW method was however used to determine the unit cell parameters of relevant bulk structures, through the stress tensor, although it was routinely checked with the usual calculation setup whether these lattice parameters also represented an energy minimum when these and values around the calculated parameters were relaxed.

2.2.1 Density of States

With GPAW we can also compute the *Density of States* (DoS), describing the number of electronic state at a given energy [37]:

$$\rho(\varepsilon) = \sum_n \langle \psi_n | \psi_n \rangle \, \delta(\varepsilon - \varepsilon_n) \tag{2.2.1}$$

Where $\rho(\varepsilon)$ is the DoS as a function of energy, psi_n is the wavefunction, and ε_n is the energy of that state. The brackets is the Dirac notation. The notation corresponds to taking the integral over the square modulus of the wavefunction. The delta-function at the end takes the value 0 for all $\varepsilon \neq \varepsilon_n$ and 1 for $\varepsilon = \varepsilon_n$, essentially 'picking' out the function value at ε_n upon integration.

Next, we can project the DoS onto a set of atomic orbitals, to estimate the occupation of said orbitals giving us the *Projected* Density of States (PDoS). This is given as the density below the Fermi Level, below which the orbital is likely to be occupied [38]. The PDoS for an atomic orbital i is given as:

$$\rho_i(\varepsilon) = \sum_n \langle \psi_n | i \rangle \langle i | \psi_n \rangle \, \delta(\varepsilon - \varepsilon_n) \tag{2.2.2}$$

Where $\rho_i(\varepsilon)$ is the DoS of a specific orbital on a specific atom as a function of energy and, trivially, all the ρ_i for all orbitals and atoms, $\sum_i \rho_i(\varepsilon)$ sum up to the total DoS $\rho(\varepsilon)$. In GPAW we can calculated the PDoS and corresponding energy directly from a .gpw file by supplying the atoms number and angular momentum quantum number of the orbital of which we want to know the PDoS.

2.2.2 Optimizing lattice constants

Using the plane wave method, we can directly calculate the stress tensor acting on the crystal by minimizing the stress, we can find the optimum lattice parameters [39]. This is directly included in the Atomic Simulation Environment (ASE) [40] with two options; purely optimizing the lattice constants, i.e. cell-size, by minimizing the stress tensor, using the module `StrainFilter`, and optimizing cell size and atomic positions simultaneously, with the module `UnitCellFilter`. Both methods were tested and yielded similar results.

2.2.3 Calculating vibrational frequencies

An important property we can extract from our optimized structures is the vibrational frequencies. These are used to convert the internal energies we get directly from our calculations, into free energies through the entropy, and are thus relevant to both the kinetics and thermodynamics. We can also compare the values obtained to experimental values, bridging modelled and true systems. The vibrations are small oscillations around the equilibrium bond length(s) of two or more atoms. The rate of oscillations is denoted the frequency of vibration. A simple way to estimate the vibrations is from a Taylor expansion of the energy around the equilibrium positions of a system of N atoms, $\vec{r}_0 = (r_{1,eq}, r_{2,eq}, ..., r_{3N,eq})$. A second order expansion of the Taylor series of the ground state energy around $\vec{r}_0$, known as the *Harmonic*

Approximation, is given as:

$$E = E_0 + \frac{1}{2} \sum_{i=1}^{3N} \sum_{j=1}^{3N} \hat{H}_{ij}\Big|_{\vec{x}=0} x_i x_j \qquad (2.2.3)$$

With $\vec{x}$ being a vector of the displacement from equilibrium positions and x_i, x_j components of this vector. Since we are at the equilibrium bond distance when the structure is relaxed, the first derivative, i.e. the 2nd term of the Taylor series expansion, is zero. $\hat{H}_{ij}$ is the Hessian matrix $\hat{H}_{ij} = \dfrac{\partial^2 E}{\partial x_i \partial x_j}$, which is also used by the BFGS method used for structure optimization, but we typically estimate it from FD displacements of the atoms in question. Using the atomic displacements to diagonalize the Hession produces 3N eigenvalues λ, with the vibrational frequency given as $\nu_i = \sqrt{\lambda_i/2\pi}$ [41].

In ASE, with the `vibrations` module, the variation of atomic displacement can be computed automatically. Specifying only an atomic system and a fixed displacement d, all atoms are displaced +/-d in each direction and each eigenvalue of the Hessian is reported.

2.3 Nudge Elastic Band - Locating the Transition State

To get an accurate description of how a given system behaves we need a robust framework to describe both the *energetics* and the *kinetics* of our system. While the thermodynamics of the relative stabilities of reaction intermediates will often give us a decent idea about the behavior of this system and performance relative to other systems, the kinetic reaction barriers between intermediates are often required to fully (or at least better) understand the system behavior. A number of different theories exist to this affect, among theses for instance the empirical Arrhenius equation [42] and the crude Collision Theory model [43].

Building on these early models, and guiding the reaction rate theory towards a more stringent theoretical description, Henry Eyring, and concurrently also Meredith Gwynne Evans and Michael Polanyi, proposed another theory describing the reaction rate, a theory now known as *Transition State Theory* (TST)[44]. The essential centerpiece of this theory is the search for, and identification of, an activated complex which sits exactly on the saddle point of a given potential energy surface (PES), as defined by one (or more) reactants and products. This stationary saddle point is identified as the highest lying state along an optimum path between reactant and product known as the minimum energy path (MEP) and represents the reaction barrier [45]. This transition state (TS) is assumed to behave as a free particle along the reaction coordinate, that is the 1D line of the minimum energy path, although only motion in the forward direction is allowed once the TS has been crossed.

Given a reaction described by TST of A + B forming AB over the transition state

AB‡ we can write up the reaction as:

$$A + B \xrightleftharpoons[k_{-1}]{k_1} AB^\ddagger \xrightarrow{k_2} AB \qquad (2.3.1)$$

Where ‡ denotes the transition state.

The Nudge Elastic Band (NEB) method used to determine the minimum energy path to locate the TS and with this, the (classical) barrier height [46]. The method was initially described by Jónsson et al. [47] and since then a number of changes and improvement to the methods have been made e.g. relating to saddle-point/TS localization and the initial interpolation between reaction intermediates [48], [49]. The basic idea behind the method is easy to picture:
We start from the stable reaction intermediates (e.g. A and B as in eq. (2.3.1)) and use an interpolation method to create unstable images along a path between the two. A first attempt at this was always made with the idpp-method [49] or, if this failed, a simple linear interpolation. To make sure all these images stay along the path and not just relax to either A or B, the images are connected by springs with spring constant k, like pearls on a string or points along a flexible elastic band (hence the name!), forcing the images to stay separated along the path between the initial and final. For such a system, the force on a given structure i is given as:

$$F_i = -\nabla V(R_i) + k_{i+1}(R_{i+1} - r_i) - k_i(R_i - R_{i-1}) = -\nabla V(R_i) + F_{i,spring} \quad (2.3.2)$$

Where $\nabla V(r_i)$ is the gradient of the PES, R_i is a position vector and k_i is a spring constant.

In early attempts at using this method, the spring constant introduced a source of error and choosing the right value could be tricky; if we keep the band to stiff (high k), the structure can risk pulling so hard on each other that we end up forcing them away from the MEP and along a more direct path between A and B. If we on the other hand allow the band to be too loose, we may be able to get all the images to fall on the MEP, but we will be "stretching" the elastic long between two images over the saddle point and none of them will be close to the saddle point. If we look at the forces above, $\nabla V(r_i)$ will be the main force pushing the atoms towards the MEP, as it has minimum in energy perpendicular to the MEP. Since the forces are uphill towards the saddle-point on the PES, it will however also push the images down along MEP, away from the saddle-point and towards the end point. The effect of the spring force is opposite, as it pulls on the images along a given path, it spaces them apart without taking the uphill force towards the MEP into account. That is also why setting k too high will cause the band to 'cut corners' to be closer to each other even if that means straying from the MEP. We can mitigate this to some extent, by increasing k as we approach the TS, but as an add-on or alternative to this, a relatively simple approach to mitigate this exists, based on the tangent to what should ideally be the MEP. This either just assumes that the images are along the MEP and uses neighboring structures to estimate the tangent or introduces more sophisticated schemes to find the actual MEP and thus the right tangent [50].

This method is known as the *climbing-image* NEB and from this we project out the components of the total force that are uphill relative to the TS, in order words the components of the spring force that is perpendicular to the path and similarly, the components of $\nabla V(r_i)$ parallel to the path. For an image subject to this method the force acting on it will be:

$$F_{i,NEB} = -\nabla V(R_i)|_\perp + F_{i,spring}\tau_\parallel\tau_\parallel \qquad (2.3.3)$$

Thus, if we are exactly on the MEP, the gradient of the PES perpendicular to the MEP, $\nabla V(R_i)|_\perp$ is 0, as the structure is at a local minimum perpendicular to the MEP at any points of this. This leaves the parallel components of the spring forces, which 'nudge' the structures towards the TS until they are all in equilibrium. Typically, this climbing image method is used on the least stable image, to allow this to move freely along the path, while the rest are still rearranging to find the MEP.

2.4 Microkinetic Modeling

With the TS (or multiple transition states) identified through the NEB method we can compute the kinetics of the reaction and, if necessary also couple this to other elementary reactions into a reaction network or for a single reaction mechanism. The rate of a reaction in equilibrium is given as the product of the activities of the reactants multiplied by the forwards rate constant subtracted the product of the activities of the products multiplied by the backwards rate constant. If we assume that the reaction in eq. (2.3.1) is a surface coupling reaction, leaving behind an empty site *, we assume that the activities is given by their respective coverages and write the rate as:

$$rate = k_+\theta_A\theta_B - k_-\theta_{AB}\theta_* \qquad (2.4.1)$$

Where k_d is the rate of direction $d = [+, -]$ and θ_i is the coverage of species $i = [A, B, AB, *]$, and, if this is the only surface reaction taking place, $\sum_i \theta_i = 1$.

The rate constants generally given relative to the activation (free) energy (approximated as the free energy of the transition state identified with NEB) as:

$$k_+ = \exp\left(-\frac{G_{a,+}}{k_BT}\right) \qquad (2.4.2)$$

$$k_- = \exp\left(-\frac{G_{a,-}}{k_BT}\right) \qquad (2.4.3)$$

Where $G_{a,+}$ is the barrier height relative to the free energy of the initial state and $G_{a,-}$ is the barrier height relative to the free energy of the final state. Next, we need to find the coverages of the various species. We assume that the steps (in this case just the "step") of our reaction network are all in equilibrium at steady state, i.e. $\frac{\partial\theta_i}{\partial t} = 0$. While this particular system could essentially be solved by hand, we generally have much more complex reaction networks and instead we use the CATMAP software package [51], which performs multi-dimensional root-finding using Newton's method to determine the equilibrium coverages and from that reaction rates and activities of the steps of the reaction network.

Electrochemical CO_2 Reduction to Two-Electron Products

2.5   Computational Details

The energetics reported in this thesis have all been calculated using GPAW [34], [52]. A real-space grid basis set was applied with a grid-spacing of 0.18 Å. The BEEF-vdW functional [32] was applied for approximating the exchange-correlation contributions. All slab calculations were conducted with periodic boundary conditions in the xy-directions parallel to the slab surface and a dipole correction in the-direction perpendicular to the surface was applied. 3x4x4 unit cells were used with the bottom two layers being constrained to optimized bulk lattice constants of the metals in question. Monkhorst−Pack k-point grids of (35/x,35/y,1), where x and y were the x and y dimensions of the unit cell of the metal slab, were used to sample the Brillouin Zone of the reciprocal lattice [53]. The setup used a Fermi smearing of $0.1\,\mathrm{eV/k_B}$. Forces were converged to $0.03\,\mathrm{eV/}$ and $0.05\,\mathrm{eV/}$ for stable intermediates and transition states, respectively. Activation energies were calculated using the Climbing Image Nudge Elastic Band (CI-NEB) method [50] within the dynamic NEB (DyNEB) implementation [54].

Electronic energies are converted into free energies via a vibrational analysis within the harmonic approximation for adsorbates and an ideal gas approximation for gas phase species, as implemented in ASE [40]. Free energy corrections of $0.33\,\mathrm{eV}$ and $0.09\,\mathrm{eV}$ was added to the gas phase energies of CO_2 (g) and H_2(g) respectively, in order to correct systematic errors of DFT when applying the BEEF-vdW XC functional [55], [56]. For structures that are not chemisorbed, e.g. gas phase species or ions, their energy is given as the gas phase or bulk solution energies respectively. For structure optimizations BFGS was used for stable intermediates and transition state, until climbing was enabled and from then on FIRE was used, the latter expected to more robust, but also slower to converge [57]. Adsorbate binding configurations were generally sampled using the CatKit Surface module [58], although for the study in Chapter 5, the most stable motifs as found on copper were used directly on the other metals, unless there were several motifs close in energy at which point they were all sampled across all of the metals.

For constant potential energetics, SJM [59] was used. This in change uses an effective potential cavity solvation model (CSM) implemented into GPAW by Held and Walter [60]. This used Bondi's van der Waals radii [61], multiplied by a constant following a metal-specific benchmark of capacitance to $20\,\mathrm{\mu F/cm^2}$. The metal-specific constants were: Ag=1.12, Au=1.10, Cu=1.06, In=1.12, Pb=1.12, Pd=1.04, while the remaining metals used the vdW radii as is. Additional parameters were: Strength of the repulsion at the atomic radii controlling the cavity size, $u0 = 0.18\,\mathrm{eV}$ [60], surface tension $1.148 \times 10^{-3}\,\mathrm{Pa*m}$ [60], a (maximal) dielectric constant $\epsilon_r = 78.36$ and a temperature of $298\,\mathrm{K}$. The tolerance for the electrode potential deviation from the target potential was set to $10\,\mathrm{mV}$.

The free energy of $HCOO^-$(aq) used in Chapter 4 was calculated from its equilibrium with HCOOH(aq) at the pKa (3.75), following the relationship $G_{\mathrm{HCOO^-},aq} = G_{HCOOH,aq} - \ln 10 \cdot k_B T \cdot (pH - pK_a)$ [62].

3 Exploring and Exploiting the Electrochemical Environment

Before we get to how we should design our electrocatalyst, lets first take a step back and take a look at what governs the activity of the "classical" gas phase heterogeneous catalysis. All catalytic processes rely on manipulating a number of well known thermodynamic variables to achieve the rate and composition of desired product(s). If we just consider the variables used to describe different statistical ensembles, this includes:

N The number of particles of e.g. reactants, catalyst material, additives etc.

V The volume of (typically) a reactor where-in the reaction takes place

p The total pressure of the system, which is often broken down into partial pressures of different compounds in the system

T The temperature of the system

E The total energy of the catalytic system

μ The chemical potential of the particles

Some of these, such as the number of particles and the volume are easy to conceptualize and understand. Additionally, although the fundamental concepts of pressure and temperature are less trivial, these are still quantities we are used to measure and *feel*.

This is not to any extent an exhaustive list, and many of these can not be varied independently. If we, just as a very simple example, assume that we have closed, non-insulated container/reactor (corresponding to a so-called *Canonical Ensemble*) containing non-interacting gasses, doubling N will naturally cause p to double as well. At the same time, some of these are quantities we can easily change, and often we do use different N, V, p & T for different reactions, in order to either change the total energy of the system and/or the chemical potential, which ultimately affect the total amount of product we get out (*activity*) as well as which products we get out (*selectivity*). One way to measure the changes in the energy of the system is through changes in the free energy, ΔG:

$$\Delta G = \Delta H - T\Delta S \tag{3.0.1}$$

With H being enthalpy and S being entropy, two other state functions related to the heat and (dis)order of the system respectively.

Consider for instance the simple gas phase reaction:

$$A + B \longleftrightarrow C \tag{3.0.2}$$

Where A and B are reactants and C is the product of the forwards reaction, we can also relate the change in (forward) reaction free energy ($\Delta_r G$) to the chemical potentials at equilibrium as:

$$\Delta_r G = \sum_f N_f \mu_f - \sum_i N_i \mu_i = \mu_C - \mu_A - \mu_B \tag{3.0.3}$$

Where i, f denote initial (reactant) and final (product) states. When $\Delta_r G$ is negative, the (forwards) reaction is assumed to occur spontaneously. For ideal gases, $\mu_k \propto \ln p_k$ and we can rewrite eq. 3.0.3 as:

$$\mu_C - \mu_A - \mu_B \propto \ln \left(\frac{p_C}{p_A p_B} \right) = \ln Q \tag{3.0.4}$$

With Q being the *reaction quotient*, also denoted the *equilibrium constant*, K, at standard conditions and equilibrium. For reference, $\Delta_r G$ is related to Q as:

$$\Delta_r G = \Delta_r G^\circ + RT \ln Q \tag{3.0.5}$$
$$\Delta_r G^\circ = -RT \ln K \tag{3.0.6}$$
$$\Downarrow$$
$$\Delta_r G = RT \ln \left(\frac{Q}{K} \right) \tag{3.0.7}$$

Where R is the gas constant. From this, we see that the reaction will occur spontaneously at standard conditions when $K>1$ or more generally when $Q<K$.

Generally, if we fed in A and B from our example above into an empty chamber, Q would be zero at first, and conversion into C would occur until we reach a situation where $Q=K$ and the system has reached equilibrium. In terms of the chemical potential, this is equivalent to a starting point where the (sum of the) chemical potentials of A and B are higher than C, leading to the formation of C until $\mu_C = \mu_A + \mu_B$.

Now, if we double the total pressure of the equilibrated system, for instance by compressing the chamber to half its original volume, we actually end up in a state away from the chemical equilibrium, as the denominator of Q/reactant side of the chemical potential increases by a factor of 4, while the numerator only doubles. Similarly, $\mu_A + \mu_B$ will increase more than μ_C, and more product will be formed until the value for K is reached (i.e. $\mu_C = \mu_A + \mu_B$ once again). Thus, when the pressure is increased, this mechanism will favor the side of the reaction that has the fewest particles.

Similarly, when we can also change the conversion rate by varying the temperature. Combining 3.0.1 and 3.0.6 we can relate K to enthalpy and entropy as follows:

$$-RT \ln K = \Delta H^\circ - T \Delta S^\circ \tag{3.0.8}$$
$$\ln K = -\frac{\Delta H^\circ}{RT} + \frac{\Delta S^\circ}{R} \tag{3.0.9}$$

Assuming that $\Delta H°$ and $\Delta S°$ are independent of temperature, at least over a small change in temperature, we can quantify the change in K as:

$$\ln K_2 - \ln K_1 = -\frac{\Delta H°}{RT_2} - \left(-\frac{\Delta H°}{RT_2}\right) \tag{3.0.10}$$

$$\ln K_2 = \ln K_1 + \frac{\Delta H°}{R}\left(\frac{1}{T_1} - \frac{1}{T_2}\right) \tag{3.0.11}$$

Or, if we can measure the equilibrium constant, use this relation the estimate $\Delta H°$ and $\Delta S°$ as the slope and intercept respectively from a fit of $\ln K$ vs $1/T$:

$$\ln \frac{K_2}{K_1} = \frac{\Delta H°}{R}\left(\frac{1}{T_1} - \frac{1}{T_2}\right) \tag{3.0.12}$$

If $\Delta H°$ is negative, eq. (3.0.11) shows us, that the equilibrium constant will decrease as temperature increases. This intuitively makes sense, as changes in enthalpy at constant pressure is equivalent to the heat exchange over the course of the reaction, and we categorize reactions as either *exothermic* (exo=outside, i.e. heat given off, leaving the reaction/system) for $\Delta H° < 0$ or *endothermic* (endo=inside, i.e. heat being "taken up" from the outside) for $\Delta H° > 0$. To indicate that e.g. a reaction is exothermic as produces heat, we might rewrite eq. (3.0.2) as:

$$A + B \longleftrightarrow C + \Delta \tag{3.0.13}$$

Where the Δ signifies heat. Writing it up like this, it is obvious that increasing the temperature and thus adding heat to the system, corresponds to adding more product and as a result the equilibrium shifts to the left to compensate.

3.1 Activity in Electrochemistry

Once we are in an electrochemical environment, a number of things are different to the "usual" heterogeneous catalysts. We are still in a heterogeneous system, but in electrochemistry the reaction usually takes place at the interface of a solid and a liquid solvent, most often water, as opposed to a solid/gas interface. Additionally, if we want to maintain the liquid phase, we can only wary the temperature between at best $0\,°C$ to $100\,°C$, and even below $100\,°C$, evaporation might be an issue. Again, we typically run the reaction at ambient conditions. Instead, we have a new variable we can utilize:

ϕ The electric potential, just referred to as the potential.

Formally, the (electric) potential is defined as the line integral of the electric field $\mathcal{E}$ taken from a reference point to point $\mathbf{r}$:

$$\phi(\mathbf{r}) = -\int^{\mathbf{r}} \mathcal{E} \cdot d\mathbf{l} \tag{3.1.1}$$

Energetics of a charged species
If we attach a charge q, we can get the work required to bring this charge to the potential at $\mathbf{r}$ as:

$$W = Q\phi(\mathbf{r}) \tag{3.1.2}$$

Or, expressed differently, the potential is essentially the *potential energy* (work) per unit charge, by this definition from infinity, but we can equivalently reference it to some potential scale, such as the potential of Standard Hydrogen Electrode (SHE), the potential of a platinum electrode where unit activity H_2 is bubbled into a solution containing unit activity H^+, establishing equilibrium[1]. Simple as that, we can account for the electric potential energy in the chemical potential of a particle as:

$$\tilde{\mu}_i = \mu_i + z_i e \phi_i \tag{3.1.3}$$

Where $\tilde{\mu}_i$ is the *electro*-chemical potential, μ_i the chemical potential at standard states including at the reference potential, i.e. $\phi = 0$, z_i the unit charge of the particle, e the elementary charge (such that $z_i e = Q$). Changing the labels for simplicity, we write the electrochemical potential as:

$$\mu_i = \mu_{i,0} + z_i e \phi_i \tag{3.1.4}$$

Where μ_i is now the electrochemical potential and $\mu_{i,0}$ the chemical potential. We can however maintain the previous notation for uncharged species, e.g. for eq. (3.0.2), as $\mu_i = \mu_{i,0}$ for uncharged species.

Energetics of a dipole

Although molecular dipole (or any dipole for that matter) is net neutral in charge, the dipole can be seen as two charges separated in space by a distance $\mathbf{d}$, with $\boldsymbol{\mu} = q\mathbf{d}$ (note that μ now refers to the dipole, not the chemical potential. As the molecule is overall charge neutral, the charge at the negative end has the same magnitude as the charge at the positive end. If we assign the negative end a charge -q, the positive end a charge of q and place the negative end at r=0, we can get the total energy (work) from eq. (3.1.2):

$$E_{\boldsymbol{\mu}} = q\phi(\mathbf{d}) - q\phi(0) = q(\phi(\mathbf{d}) - \phi(0)) \tag{3.1.5}$$

This is equivalent to a line integral over the electric field, as the work we need to overcome is merely force times distance and the force acting on a charge q is related to the electric field as $\mathbf{F} = q\boldsymbol{\mathcal{E}}$:

$$E_{\boldsymbol{\mu}} = q \int_0^{\mathbf{d}} \boldsymbol{\mathcal{E}} \, \mathrm{d}\mathbf{l} \tag{3.1.6}$$

Assuming the dipole is ideal (infinitesimal) separation such that the field is uniform, the energy associated with the dipole is:

$$E_{\boldsymbol{\mu}} = q\mathbf{d}\boldsymbol{\mathcal{E}} = \boldsymbol{\mu}\boldsymbol{\mathcal{E}} \tag{3.1.7}$$

Now, the total energy of the system E is the adsorption/hybridization energy (E_0) plus the energy contribution from the dipole $E_{\boldsymbol{\mu}}$:

$$E = E_0 + \boldsymbol{\mu} \cdot \boldsymbol{\mathcal{E}} \tag{3.1.8}$$

For a system where the dipole binds via its positive end on a negative surface, $\boldsymbol{\mu}$ and $\boldsymbol{\mathcal{E}}$ are opposite in z and this is a stabilizing effect i.e. $\boldsymbol{\mu} \cdot \boldsymbol{\mathcal{E}} = -|\mu\mathcal{E}|$.

It should also be noted that the dipole is merely the first term of the adsorbate/field interaction, it can be further expanded to include the surface polarizability $\boldsymbol{\alpha}$ (as $-1/2\boldsymbol{\alpha}\boldsymbol{\mathcal{E}}^2$) [63] or even higher order terms if necessary.

---

[1] usually approximated by $p_{H2} = 1 \, \text{atm}$ and $[H^+] = 1 \, \text{M}$, known as the *Normal Hydrogen Electrode*

Electrochemical CO_2 Reduction to Two-Electron Products

3.2 Modeling Reaction Energetics in Electrocatalysis

As the potential has a massive impact on the activity of an electrocatalyst, we of course need to account for that when we calculate the reaction energetics we use to predict the catalyst performance. On a macroscopic scale, we are usually interested in knowing the catalyst performance at *constant potential*, applying a potential difference between two electrodes by supplying electrons, often referenced to a specific potential scale. Let us as an example consider a proposed mechanism for the reduction reaction of CO_2 to CO in acid:

$$CO_2(g) + * \rightleftharpoons *CO_2 \tag{3.2.1}$$

$$*CO_2 + H^+ + e^- \rightleftharpoons *COOH \tag{3.2.2}$$

$$*COOH + H^+ + e^- \rightleftharpoons *CO + H_2O \tag{3.2.3}$$

$$*CO \rightleftharpoons CO(g) + * \tag{3.2.4}$$
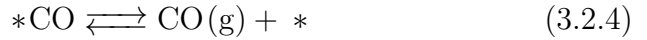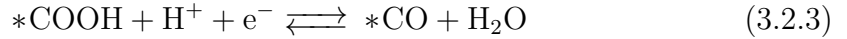
Here, the 2nd and 3rd step involves a PCET, where we transfer both an electron and a proton to a reaction intermediate.

Computational Hydrogen Electrode

A simple, yet very accurate way of calculating the energetics of a charge transfer reaction is through the Computational Hydrogen Electrode (CHE) [64]. Firstly, it is assumed that the energy of the uncharged intermediates are purely chemical in nature, i.e. $\mu_i = \mu_{i,0}$. Secondly, we can write up to the (electro)chemical potentials of the charged components using eq. (3.1.4), measuring the potential against SHE:

$$\mu_{e^-} = \mu_{e^-,0} - e\phi_{e-} \tag{3.2.5}$$

$$\mu_{H^+} = \mu_{H^+,0} + k_B T \ln a_{H+} + e\phi_{H+} \tag{3.2.6}$$

Where, as SHE is defined relative to a solution of unit activity H^+ (i.e. pH $\approx$ 0), we have included the possibility of an activity that deviates from its standard state and approximated the activity as concentration to get:

$$k_B T \ln a_{H+} = k_B T \ln [H^+] = k_B T \frac{\log [H^+]}{\log e} = -2.30 k_B T \text{pH} \tag{3.2.7}$$

Additionally, the electron is located at the surface of the metal slab with potential $\phi_{e-} = \phi_M$ (or simply ϕ_{SHE}), while the proton is located in the bulk, where the potential is equal to the reference potential $\phi_{H+} = 0V$ vs SHE.

Next, we exploit the electrochemical equilibrium at the reference electrode (SHE):

$$\mu_{H^+,0} + \mu_{e^-,0} = 1/2\mu_{H_2,0} \tag{3.2.8}$$

Combining all of this, we get:

$$\mu_{H^+} + \mu_{e^-} = \mu_{H^+,0} + \mu_{e^-,0} - 2.30 k_B T \text{pH} - e\phi_{SHE} \tag{3.2.9}$$

$$= 1/2\mu_{H2,0} - 2.30 k_B T \text{pH} - e\phi_{SHE} \tag{3.2.10}$$

With this, we have completely separated out the need to include charges explicitly in our system, instead referencing the energetics of the proton/electron couple to

easily obtainable quantities such as the energy of H_2 and properties of the system, T, pH and ϕ_{SHE}.

An alternative (and simpler) is to relate the energetics to a potential relative to the Reversible Hydrogen Electrode (RHE), setting the equilibrium potential of the reaction at the SHE to 0 at any pH. With regards to this reference, $\mu_{H^+,0}$ simply becomes:

$$\mu_{H^+} = \mu_{H^+,0} \tag{3.2.11}$$

And $\mu_{H^+} + \mu_{e^-}$:

$$\mu_{H^+} + \mu_{e^-} = 1/2\mu_{H2,0} - e\phi_{RHE} \tag{3.2.12}$$

The energy difference of a PCET such the *COOH formation in eq. (3.2.2) then becomes:

$$\Delta G = G(*COOH) - G(*CO_2) - G(H^+) - G(e^-) \tag{3.2.13}$$

$$= G(*COOH) - G(*CO_2) + e\phi_{RHE} \tag{3.2.14}$$

The amount of charge corresponding to a given potential varies depending on the metal, solvent and other components of the system [65], [66]. The potential where the total charge on the metal surface is 0 (possibly including charging related to adsorption/desorption events) is known as the Potential of Zero Charge (PZC) [67] and is highly relevant for many electrochemical processes, including CO_2 reduction [68]. In our simulations, we can connect the potential and PZC to the metal work function, and use changes in the work function as a proxy for changes in potential [69]–[71]. As a crude estimate, we can relate the change in work function relative to some experimental reference value to a potential against the same reference. We can e.g. convert it to potential vs SHE, assuming $\Phi_{SHE} \approx 4.4$ [72]:

$$\phi_{SHE} = \frac{\Phi - \Phi_{SHE}}{e} \tag{3.2.15}$$

Energetics through charging schemes

Since electrons are consumed at the cathode, where CO_2 reduction takes place, more electrons must continuously be added to keep the system at steady state, i.e. the potential constant. On a macroscopic scale many electrons are being consumed and added at the same time, controlled by a potentiostat. When we try to mimic the system with DFT and simulate the reaction(s) taking place, we unfortunately do not have this luxury by default. Instead, when we for instance want to simulate an elementary reaction involving a Proton Coupled Electron Transfer (PCET) step, we typically inadvertently change the charge on the metal in the process. An illustration of the 2nd step of CO_2 reduction to CO, eq. (3.2.2) is shown in Figure 3.1, including the transition state and the amount of charge added along each point of the MEP, calculated using SJM (see the SJM section below for details).

Now, in our periodic unit cells (e.g. Figure 3.1) we are always charge neutral and by default the number of electrons matches the number of protons from all our atoms. We also do not have any free charges floating around in vacuum, nor did we assign any positive charge to the hydrogen. Instead, what happens when we simulate the initial state, is that DFT as described in Chapter 2, places the electrons in
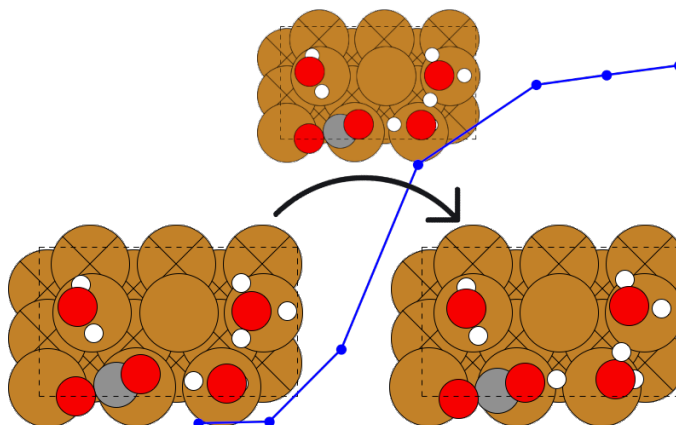
Figure 3.1: *CO$_2$ to *COOH PCET reaction

Illustration of the setup for a PCET from H$_3$O$^+$ to *CO$_2$ to form *COOH, depicting the initial state, transition state and final state, along with a band (blue) showing how the charge added to the system changes along the reaction pathway.

their lowest energy state around the atoms in the cell. This places 1[2] electron more around the metals, smeared out over the surface, resulting in a surface charge density of $\sigma = -1\,e/A$, where A is area, while the H$_3$O molecule has one electron less, making it H$_3$O$^+$. This can be translated into a potential change through the capacitor relationship:

$$\sigma = C_H(\phi - \phi_{PZC}) \tag{3.2.16}$$

$$\Delta\phi = \sigma/C_H \tag{3.2.17}$$

Assuming that the Helmholtz capacitance C_H remains constant over the potential range. With this, the surface charge has shifted the potential away from the PZC by $\Delta\phi = \sigma/C_H$. However, once the reaction occurs, the two spatially separated charges 'disappear', combining to form *COOH, shifting the potential back to the PZC (at least to a first approximation), and with that we are completely altering the driving force of the reaction. Naturally, we need to account for this, transforming the energetics from what is essentially *constant* (total) *charge* into *constant potential*. A number of different schemes exist for doing this and a sample of these are outlined in the paragraphs below.

Explicit charging (and solvent) methods

First, there are some methods based on explicitly charging the metal/solvent/adsorbate interface and through that varying the charge density on the surface. This can either be achieved through separated charges, where a solvent above the surface and the surface itself have different charges as the PCET example above, through charged co-adsorbates such as electropositive metal cations, or through variation in dipoles from different components of the system, e.g. water molecules or adsorbed CO$_2$. Although the net charge is 0, the dipoles have a partial positive end and a

---

[2]In fact, the amount of additional charge of such a setup often only corresponds to around 0.6-0.8 of an electron, although it is not entirely clear why [73].

partial negative end and will act as additional charging components, in effect small capacitors, changing the potential with their orientation relative to the surface. Especially the water layer is well known to orient relative to the charge on the metal and also impact the metal PZC [71], [74].

Cell Extrapolation

A relatively simple, but also computationally heavy method is the cell extrapolation method [69]. The general idea is to calculate the energetics of the same elementary reaction, but at varying cell size. Doing this while keeping the no. of protons constant, we distribute the extra electron across a larger and larger surface, leading to a drop in surface charge density as the area increases with cell size and thus potential / potential difference. We then measure the change in energy, ΔE, as a function of the change in work function relative to one of the states, e.g. the initial state, $\Delta \Phi$. This is extrapolated to $\Delta \Phi = 0$, i.e. an "infinite cell-size" where the consumption of a single charge doesn't change the work function/potential, similar to the experimental conditions. This has been done successfully for relatively simple processes (in terms of the components involved), such as HER and HOR [75]. This can in theory also be expanded to more complicated reactions, but more bulky intermediates introduces new challenges. As mentioned, the water dipoles have a significant impact on the potential, and thus the driving force. Unfortunately, water reorganization (or *water flipping*) between two states can be as issue that can convolute the results. An example of this is shown for the adsorption of CO_2 in Figure 3.2, where the effect of varying the charge through the unit cell size is almost completely screened from the water flipping between the different states in the same unit cell size.

(a) Energy vs. proton concentration (b) Energy vs. work function

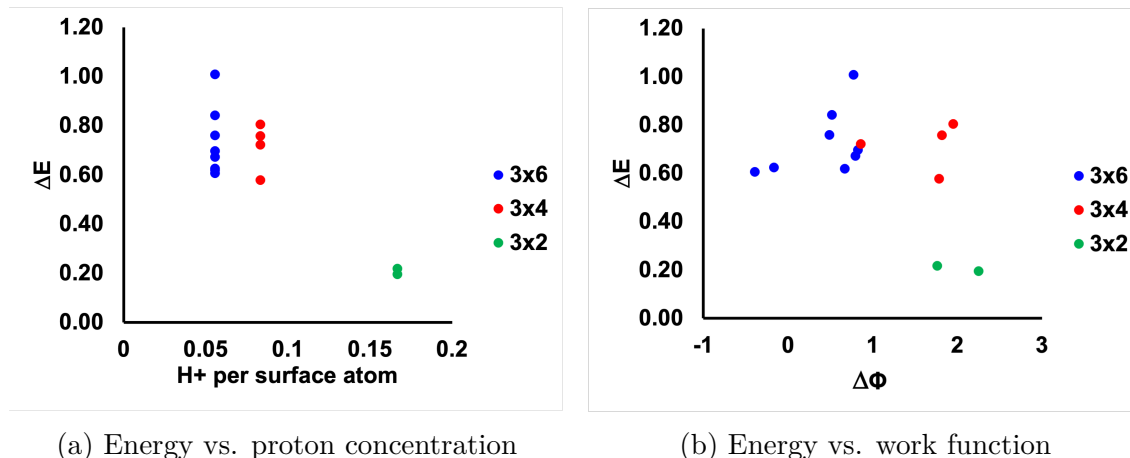Figure 3.2: Cell Extrapolation for CO_2 adsorption

Adsorption energy versus proton/surface atom ratio (a) and change in work function (b).

In the ideal case where the only change in contribution to charge in the system is the proton/electron couple, we could infer the effect of changing the charge from 3.2a. If we include the full work function of the metal as done in 3.2b, we should be able

to account for the total potential change, and extrapolate this to $\Delta\Phi = 0$. However, it is clear that the water reorganization also introduces scatter in the adsorption energies that is either making the system deviate from the simple capacitor model or is not related to changes in the potential, the effect being so large that we cannot deconvolute this from the contributions from potential.

Charge Extrapolation

The concept of charge extrapolation is to some extent similar to the cell extrapolation in the cell setup, in fact any of the cells used for the cell extrapolation could be used to perform charge extrapolation, without needing any new DFT calculations. The big advantage of this model is that we only need one the energies of one cell size to estimate the energy at a specific work function, and thus constant potential [73]. Essentially we relate the energy change to the change in work function and the change in excess surface charge, measured as the sum of Bader charges of all ions in solution (in fact the negative of that, the charge "missing" from the ions is located on the metal atoms of the slab, otherwise the system would not be net neutral).

We can predict the energy change of a reaction at the work function of the initial state as:

$$\Delta E(\Phi_1) = E_2(\Phi_2) - E_1(\Phi_1) + \frac{\Delta q(\Phi_2 - \Phi_1)}{2} \tag{3.2.18}$$

Where E are energies, Φ are work functions and $\Delta q = q_2 - q_1$, where q are charges. Or relative to the final state if we swap out the indices, then the third terms just changes sign. From this we can translate this to an energy at any arbitrary work function Φ as:

$$\Delta E(\Phi) = \Delta E(\Phi_{ref}) - \Delta q(\Phi - \Phi_1) \tag{3.2.19}$$

Similarly to the method above, this method works best for simple reactions with little dipole reorganization, where we can assume that the electrostatics are purely a consequence of the separation of the charge and the protonated solvent [76].

Implicit Charge (and solvent) methods

Rather than charging and solvating the surface with physical, atomistic components, it is also possible to mimic the effects of charge and solvent through continuum models. These include different approximations for the electrostatic effects that a solvent will present and for how it will interact with the surface. In principle, this could just involve solvation, but often there is also a charging component that will allow us to add extra charge into the system at our region of interest (i.e. on or close to the surface), while placing a (screened) counter charge at a safe distance from the surface. While the implicit solvent is supposed to mimic a "true" solvent, the continuum nature of the system means that while it captures the average effect of a solvent, it cannot necessarily account for strongly local effects, such as the field effect of an ion of finite size [77], or the strong (relative to long-range electrostatics) effect of hydrogen bonding could have on the stability of some intermediates [78].

PBE Model(s)

A prominent example of this is for instance the VASPsol module [79], which can be used with the commercial VASP DFT code [80]. This uses DFT to calculate the energy of the metal surface, and couples this through an interface region to a

simulated electrolyte, where the potential distribution is described by the Poisson-Boltzmann equation [81]. The target is to manipulate the dielectric constant of the region above the reaction to match that of a specific solvent, usually water w/o ions or other components. In effect this produces a continuous charge density "layer" that wraps around the surface and it components, both solvating/screening it from the vacuum and often also introducing a driving force for the reaction through the addition of charge. An issue with this (and other) implicit models is that we sometimes have systems, where changes in the work function does not uniquely translate into energy changes, but instead varies with system parameters. This is particularly true when we introduce an explicit charging component, such as the dipole formed upon CO_2 adsorption. If the capacitance of the two components are different, the slope of energy with work function will also vary [82].

A proposed solution to this, is to use the effective surface charge density instead [83] (recalling $= \sigma = C_H \Delta\phi$) and estimating the explicit contribution to the charge/charge density from the dipole through forces on the atom upon adsorption [84].

Solvated Jellium Method - *The Computational Potentiostat*

Another option is using the Solvated Jellium Method (SJM) [59]. SJM is not in itself an implicit solvent, but a charging scheme that requires an implicit solvent to work and as such comes with the same limitations as other implicit models. It can however be used both with and without an explicit solvent, although for some kinetics such as PCET step we would typically need to include some type of solvent as a proton donor. For this work it has been used with GPAW and the Continuum Solvent Model [60], a different PBE model. It works by placing a "jellium" slab of positive charge inside the implicit solvent region, well above the reaction plane, accompanied by a matching amount of negative charge as free electrons. This now gives the implicit solvent a dual purpose; not only does it solvate species in the reaction plane, screening them from the vacuum above, it also screens the reaction plane from the positive jellium slab. Without the implicit solvent, the gradient of potential (i.e. the electric field) would be artificially high, as we would be going from a negative charge region on the metal surface to a positive region at the counter charge. In a true system, this would correspond to placing the working and counter electrode immediately next to each other, while they are in effect well separated with a large region where the solvent is at constant (bulk) potential, and thus zero field. By screening the positive charge on the counter charge, we have a large region above the reaction plane at constant potential that we can reference our electrode potential/work function against, and both are referenced to some absolute potential/work function, e.g. the SHE potential. That is not to say that this potential will be fixed to some value independent of the system, instead it will change depending on the metal surface, but also components such as the water layer orientation. This is equivalent to how the water solvation and orientation plays a role in the metal PZC [71].

For a change in charge to correspond to a change in driving force, the charge has to accumulate on the metal slab, specifically the surface facing the reaction plane. While charges on the metal generally does accumulate on the surface, resulting in a linear response in potential across a large charge region, the work function on the

backside of the slap should be measured to ensure this does not change. Additionally, in extreme cases of very high added or removed charge, we can end up either depositing charge within the implicit solvent above the reaction plane or removing charge from both the metal and the HOMO of the water molecule. Upon probing this, it was found that changing the charge gave a linear potential response in a region between $-2.4\,\text{V}$ to $2.6\,\text{V}$ vs SHE. For energetics calculated near the boundaries of or outside this region it should be ensured that this linear response still holds. Next, the parameterizations of the implicit solvent has a tendency to place the solvent unphysically close to the surface, as it doesn't account for e.g. ion solvation shells in charged solvents [77]. To account for this, we systematically vary the van der Waals radius of the metal atoms, measuring the work function change as a function of surface charge density for each radius, finding the capacitance as the slope of this relation through eq. (3.2.16), benchmarking this to an assumed experimental double layer capacitance of $20\,\text{µF/cm}^2$ [85].

Now, with the system set up we can compute energetics at either constant charge or constant potential. In the constant potential mode we specify an initial guess on the charge. SJM will then run an electronic relaxation with DFT, place the implicit solvent relative to this structure and, having both a reliable surface potential a reference beyond the reaction plane, calculate the potential at the given charge. Next, more or less charge will be added relative to the calculated and target potential. After a few iterations we get a linear fit for the charge/potential relationship, which can be used to reach the target potential. Once the target potential has been reached, a geometric relaxation is carried out. This may change the potential slightly, and if the new potential is outside the target potential region, it is once again equilibrated and so on. Essentially, we add a new iterative loop in addition to the geometric and electronic relaxations. It should be noted however, that for small structural changes, the associated potential response is also expected to be small and typically we remain near the target potential or do 1-2 additional potential calibrations, utilizing the linear charge/potential fit from previous calculations. With this, we can cycle across a range of potentials and obtain a fit for the energy change with potential for a given structure. As discussed in Chapter 3, the chemical potential of the electron changes with potential, the energies we compare should account for this, and we should compare the Grand Canonical energies (Ω) given as:

$$\Omega = E_{DFT} + N_e e \cdot \phi_e \qquad (3.2.20)$$

Where E_{DFT} is the DFT energy we get from our relaxation, N_e is the number of electrons added, which multiplied e gives the charge, and ϕ_e is the calculated potential. This gives us a quantitative measure for the (field) stabilization of a given adsorbate with potential.

One of the strengths of this workflow is that we do not need to assume anything about the structure or e.g. sample different configurations to get dipoles from forces etc., instead we are constant updating this contribution upon changes in structure. This also leads to another major advantage of the workflow; the ability to calculate potential-dependent barriers from a single NEB calculation.

As we measure the potential as function of structure and charge, we can set a target potential for an entire band of structures, calculate the amount of charge needed to reach a given potential for each structure in the band and in this way get barriers at a constant driving force, by injecting a varying amount of charge along the band. With this, the SJM workflow works essentially as a *computational potentiostat*, controlling the potential by varying the amount of charge supplied, in order to keep the driving force constant.

Further Considerations

While these methods all give reasonable measures for energetics, there is also room for improvement. If we for instance take SJM, we rely on a number of assumptions about certain quantities, e.g. the constant value of the SHE potential, although this is known to vary and computational models to accurately reference this exist and should ideally be included [70]. The implicit solvent used in SJM (and elsewhere) could also use more robust benchmark or e.g. just be benchmarked to double-layer capacitances for each metal separately. Also, even though we have a much more physically sound system when accounting for the potential in computing the PCET barriers, the full path does not necessarily represent a physical system. When we e.g. compute barriers with water as a proton donor, our final state will contain and OH^- in the reaction plane immediately next to a negative surface. Ehile we can often account for this through referencing to the initial state with water, a very late transition state will have the characteristics of the final state. Instead, we could use methods that explicitly account for solvent dynamics [86].

4 The Power of Potential

Modeling Carbon Selectivity on Pd

This chapter studies CO_2R selectivity and activity on palladium. We discuss why this differs from the trends observed in the periodic table and what exactly sets palladium apart from the rest. We explore the effects of the electrochemical environment, which are manifold, as it shows to affect not only product selectivity and activity, but also the stability, morphology and even composition of the electrode itself. For this purpose, we employ DFT with SJM to obtain constant potential barriers and electric field responses of intermediates. Additionally, we build a microkinetic model to map out activity as well as selectivity towards the two carbon products from PdH, CO and $HCOO^-$. The project is a result of a research collaboration with experimental groups at McMaster University, Hamilton, Canada and unless otherwise noted, the experimental data referenced and illustrated was obtained there. The contents of this chapter are from the manuscript *In-Situ Liquid Phase Transmission Electron Microscopy and Electron Diffraction Provides Mechanistic Insight into Electrochemical CO_2 Reduction on Palladium/Palladium Hydride Catalysts* [87], *(submitted)*, enclosed in Section A.1.

4.1 Introduction

If we turn our attention to the periodic table in Figure 1.3 showing product selectivities in CO_2RR, we see that the carbon selectivity is quite nicely grouped into different sections. Starting from the bottom right, the post-transition metals in the bottom rows, 5 and 6, produce formate. Then, once we go to the left and up, we arrive at the CO producers until we reach the top corner of the CO_2RR active materials with copper which, as the only pure metal, is able to produce significant amounts of C_{2+} products. There is one metal which clearly does not seem to fit the trend however; palladium. Here, palladium is shown to produce formate, while all the metals next to it produces either H_2 or CO with more than 80% FE. Formate (in its protonated form as formic acid) is a high-value carbon product and although the market for formic acid is currently small [19], the potential uses include usage as a green fuel in direct formic acid fuel cells [88], a market that is expected to play a crucial role in the transition away from fossil fuels. Even beyond this, the selectivity between $HCOO^-$ and *CO/CO is of fundamental interest, as this selectivity determines whether we can further reduce CO_2 to other fuels [20], [89]. And while it is true that Pd produces formate at low overpotentials [90], the product selectivity rapidly changes over a few 100 mV, to first produce H_2 and then CO [91]. Understanding this selectivity switch might help us gain a better general understanding of this selectivity and guide us in the search for new materials. The change in selectivity is illustrated in Figure 4.1, using our own experimental data. Another well known is the morphology change that palladium undergoes, transforming into palladium hydride (PdH_x) with the application of a potential bias [90]. These PdH_x structures are usually divided in to two regimes, the *α-phase*, with a (bulk) H/Pd ra-

tio of $0 < x \leq 0.03$ and the *β-phase* with $0.58 \leq x$, with $0.03 < x < 0.58$ containing a mix of the two phases [92]. The formation of the α-phase starts at slight positive potentials vs. RHE (at pH=6.8, so slightly negative vs. SHE), followed by a short interim at neutral to slightly negative potentials until the β-phase is finally complete at around $-0.1\,V$ to $-0.2\,V$ vs RHE [93]. This transformation of the electrode is also in contrast to neighboring metals that do not readily form hydrides. Whether this morphology change plays a role in the CO_2 reduction activity, and what role it plays, remains elusive and several mechanisms have been proposed. It has for instance been proposed, that the low H-loading α- and mixed phases are selective for formate production, while the high-loading β-phase is selective towards CO [94]. This work probes the morphology changes in Pd to PdH, characterizes the surface and its active phase and relates it to activity and selectivity changes on the metal.
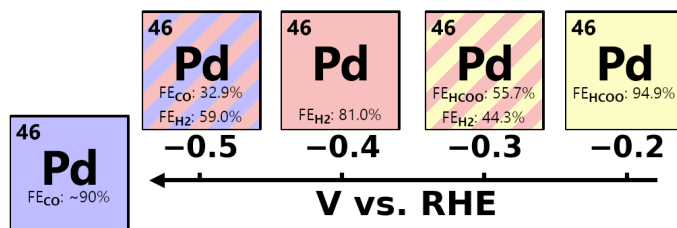

Figure 4.1: CO_2R selectivity changes on PdH

Schematic giving an overview of the selectivity changes that occurs on Pd as a function of potential vs. RHE. Color scheme is similar to Figure 1.3, i.e. yellow is formate, red is hydrogen and blue is CO. The panel furthest to the left signifies potentials below -0.5 V vs. RHE, where PdH has been found to produce formate with up to $90\,\%$ FE [94].

4.2 Structure and morphology of Palladium (Hydride) nanoparticles.

For this work, palladium nanoparticles were synthesized and deposited onto a working electrode. Upon applying a bias vs. RHE (pH=6.8), we were able to directly measure the bulk lattice constant, as a proxy for the palladium phase present, through STEM from 1.2 down to $-0.5\,V$ vs. RHE. We observed relatively small changes in the lattice constant for the formation of the α-phase, followed by a sharp increase in the lattice constant, as the β-phase was formed until it plateaus once the formation of the β-phase is completed. These experimental results are shown in Figure 4.2. The total lattice expansion is compared with calculations of the lattice constants using DFT. Here, the (111) and (100) facets of the fully hydrogenated β-phase PdHx were studied and compared to the pure palladium metal. Hydrogen atoms were located in the octahedral sites of bulk Pd, corresponding to hollow sites on the surface of Pd[1]. The lattice parameters of the β-PdHx bulk structure were optimized by varying the lattice parameters until the forces and energies were minimized, leading to a 0.12 Å increase in the (111) d-spacing compared to metallic

---

[1]Adding Hydrogen to the tetrahedral sites was also tested, and although the DFT energies were comparable, once accounting for ZPE, the octahedral sites were ultimately the most stable, in line with other findings from electronic structure methods [95].

Pd, as shown in Figure 4.3, in line with the experimental observations presented in Figure 4.2.
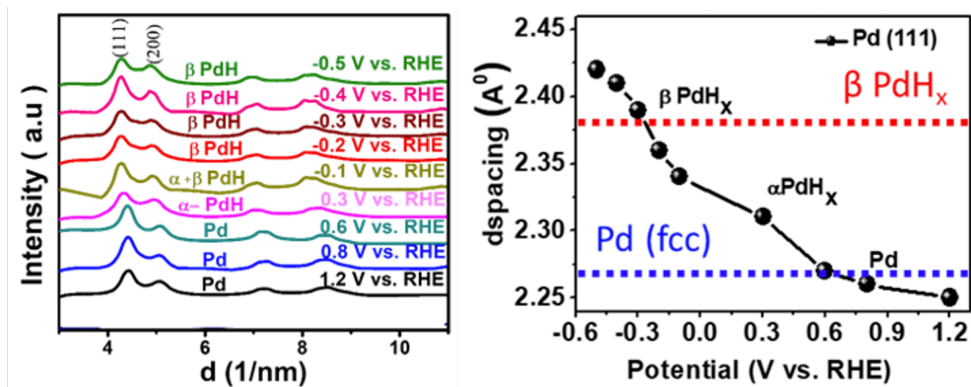
(a) Radial intensity with potential (b) Average d-space values, $PdH_x(111)$

Figure 4.2: Changes to the radial profile of Pd(H) metal-metal distances

(a) shows radial intensity profiles (metal-metal distances) from analysis of STEM images. (b) shows the average d-spacing (layer distance) of a Pd(111) surface as function of potential, along with experimental references for Pd (blue) and β-PdH (red). *Experimental data, reprinted from manuscript in Section A.1* [87].
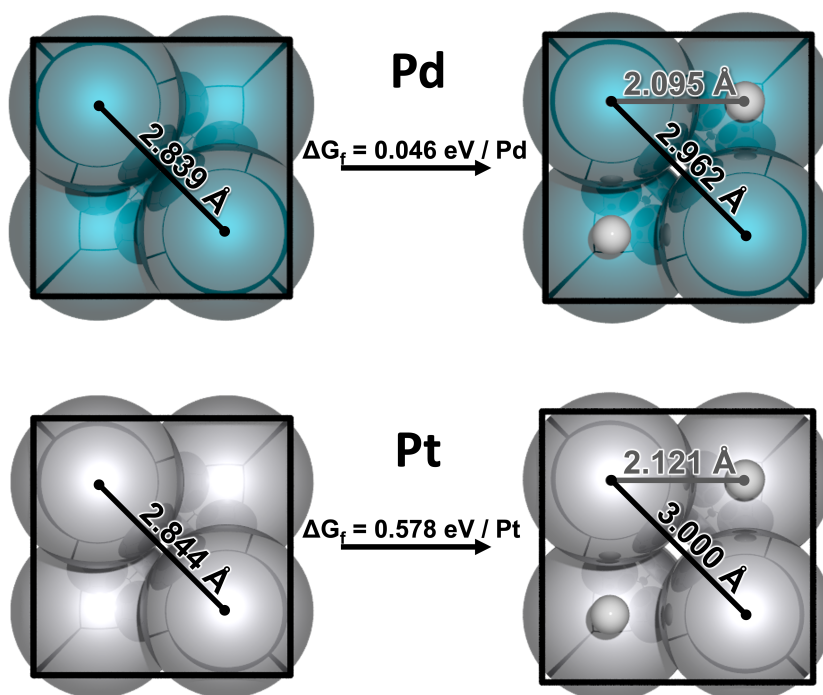

Figure 4.3: Lattice expansion under hydride formation

Illustration of the structural changes that Pd and Pt undergoes during hydride formation. The distances shown on the figure are metal-metal (black) and metal-hydrogen (grey) distances of the bulk structure.

In an attempt to understand why palladium exhibits this unique ability to form hydrides, a platinum hydride bulk structure was produced in a similar manner. An illustration of the structural changes is given in Figure 4.3 including bond lengths. The formation free energy (ΔG_f) of the palladium and platinum hydrides, according to eq. (4.2.1)

$$\text{M} + 1/2\text{H}_2(\text{g}) \longrightarrow \text{MH, M=[Pd,Pt]} \qquad (4.2.1)$$
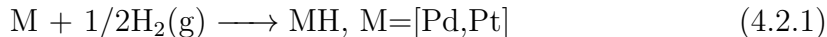
This gives $\Delta G_f = 0.046\,\text{eV/atom}$ for PdH and $\Delta G_f = 0.578\,\text{eV/atom}$ for PtH, i.e. more than an order of magnitude difference between the two. Comparing the geometries, we find that they initially have roughly the same lattice constant, but that the lattice expansion is significantly larger in PtH than in PdH, in fact 25% (0.159 vs. 0.123 Å). We attribute this to the slightly larger van der Waals radius of Pt, compared to Pd [61], [96], since the M-H distances are very close to their respective vdW radii. This means, that the octahedral hole on PdH is just small enough to accommodate and bind a hydrogen atom strongly, without being so small that the lattice has to expand too much, as is apparently observed on Pt. In addition to the bulk structure of Pd, we also calculated the stability of the surface hydrogens, measured as the differential hydrogen adsorption energy, i.e. calculating the energy change, ΔE, of adding in the next hydrogen at each possible hydrogen coverage, measured as numbers of hollow sites on a 4x3 slab:

$$\text{Pd}_{12}\text{H}_{m-1} + 1/2\text{H}_2 \longrightarrow \text{Pd}_{12}\text{H}_m \text{ for } m = [1..12] \qquad (4.2.2)$$
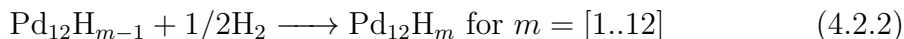
This gives us a rough estimate of the surface stability of *H and thus the coverage.
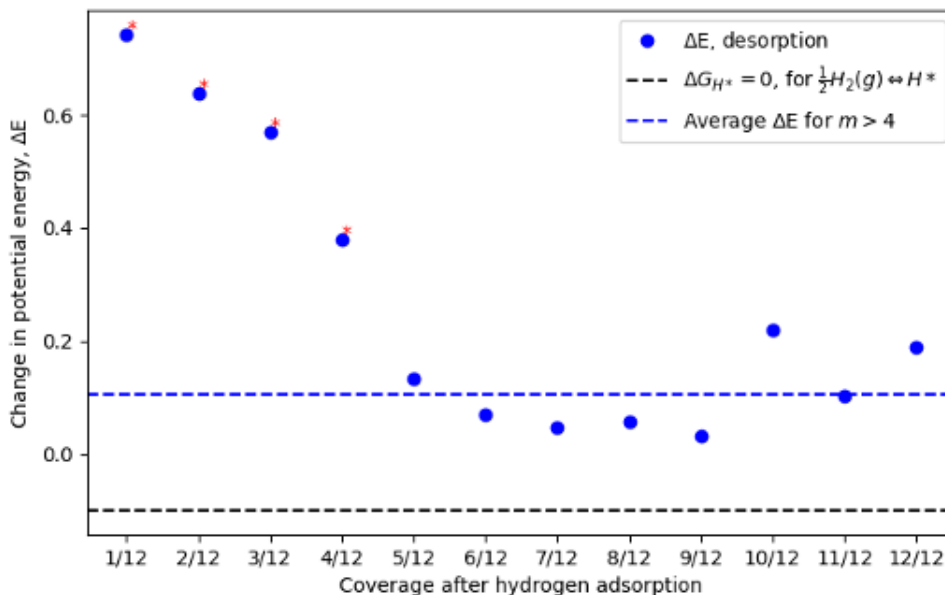
Figure 4.4: Differential adsorption energies for hydrogen adsorption onto PdH(111) Hydrogens were adsorbed into hollow sites of the PdH surface. In the structures marked with an asterisk, there is hydrogen migration from the subsurface to the surface, which convolutes the adsorption energy picture. For the remaining 8 coverages, the average change in potential energy (blue line) is roughly 0.1 eV. The black line approximates the entropy loss of hydrogen adsorption as roughly 0.1 eV.

From the results of this, shown in Figure 4.4, we see that the hydrogen binding in nearly thermoneutral up to a coverage of roughly 3/4 ($\Delta E_{avg} \approx 0.05\,\text{eV}$), and at very low coverage we even see subsurface to surface migration of *H, reestablishing this coverage. The last few hydrogen adsorptions are a bit less energetically favored, but we still expect a full monolayer of hydrogen to be present at roughly $-0.3\,\text{V}$ vs. RHE.

4.3   CO$_2$R on facets and phases of Palladium

The experimental CO$_2$R (and HER) selectivity and activity is shown in Figure 4.5 as faradaic efficiency and total current respectively.
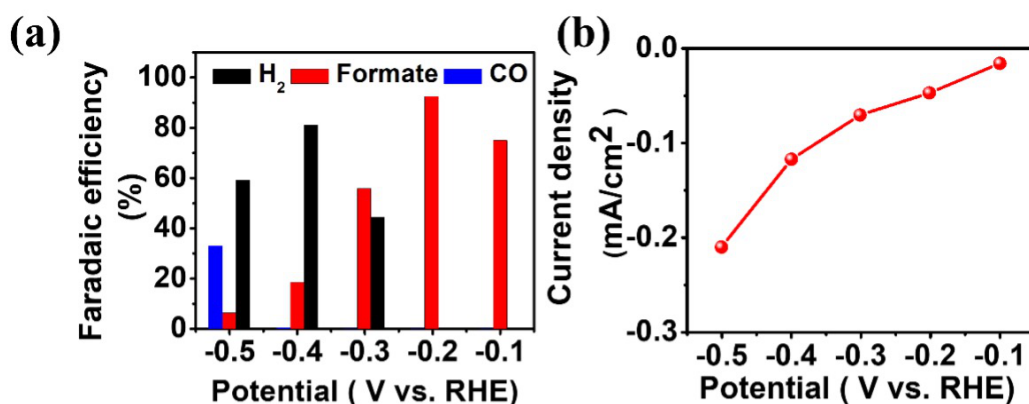
Figure 4.5: Electrocatalytic selectivity and activity of Pd nanoparticles

(a) Shows selectivity, as Faradaic effeciency, towards HCOO$^-$ (red), CO(blue) and H$_2$(black) as a function of applied potential vs RHE. (b) Shows activity, as the total current density, as a function of applied potential vs RHE. *Experimental data, reprinted from manuscript in Section A.1* [87].

For the CO$_2$ reduction activity on the Pd nanoparticles, we investigate the reaction mechanisms on the two main facets found experimentally, (111) and (100), and on both the α- and β-phases of the facets. Since the hydrogen loading and the lattice change is very small for the α-phase, we use to pure palladium slab as a proxy for this phase. For the β-phase we used the fully hydrogenated surface of PdH, in accordance with our hydrogen adsorption data above, and the measured lattice expansion. As a first approximation, we carry out simple gas phase calculations using GPAW. The results of this is shown in Figure 4.6 and Figure 4.7 for the 100 and 111 facets respectively. From this, we identify most of these systems to be CO poisoned. CO poisoning has previously been proposed in palladium CO$_2$R [90], [97] and we also see CV peaks when sweeping to positive potentials, believed to be stemming from this. In fact, the only system that is not CO poisoned is the β-phase of PdH(111). Since the β-phase starts partially forming at slightly positive potentials vs. RHE and is near-complete at $-0.1\,\text{V}$, where the first CO$_2$R current is measured, we propose that the electrochemically active phase and facet is β-PdH$_x$(111), modeled as stoichiometric PdH(111).
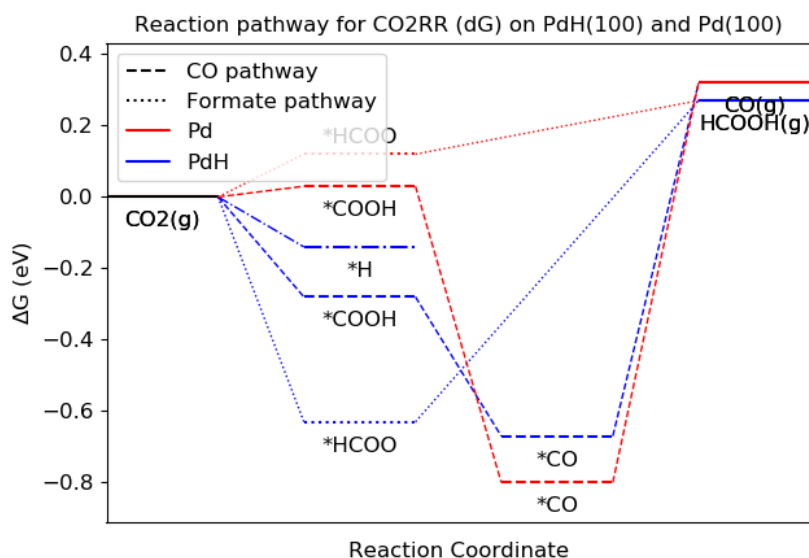
Figure 4.6: Proposed pathways to CO and HCOO⁻ on Pd and PdH(100) facets CO route is shown with dashed lines, HCOO⁻ with dotted. Red is Pd, blue PdH.
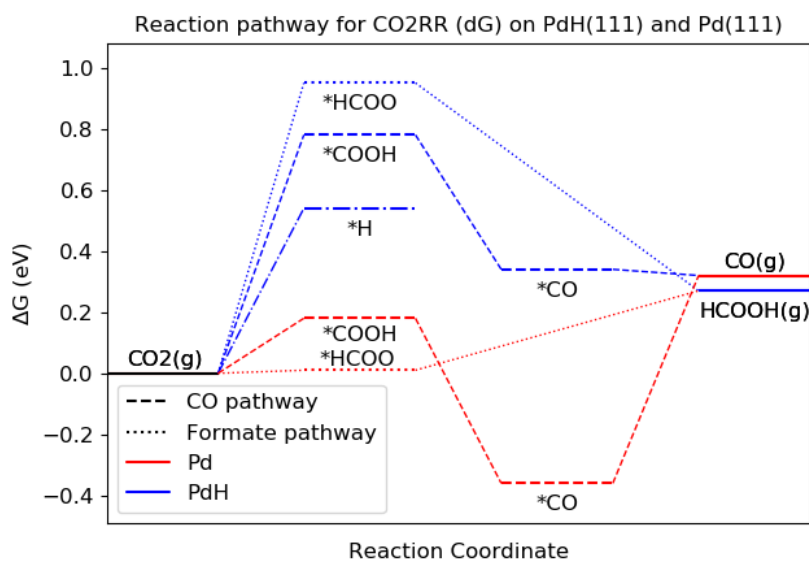
Figure 4.7: Proposed pathways to CO and HCOO⁻ on Pd and PdH(111) facets CO route is shown with dashed lines, HCOO⁻ with dotted. Red is Pd, blue PdH.

Even so, the FED for PdH(111) does not look promising either. In fact, both the CO and the HCOO⁻ pathway is quite uphill in energy based on the gas phase data. And *HCOO, which is usually more stable than *COOH is less stable here, making the formate pathway difficult to realize at low potentials. To get a better understanding of the energetics, we employed SJM to get constant-potential energetics and to be able to compute energetics for field-stabilized intermediates such as *CO$_2$. With SJM, we find that the *HCOO is in fact so unstable, that once we charge the

Electrochemical CO$_2$ Reduction to Two-Electron Products

surface, it desorbs as an ion, i.e. the final product, formate. Instead, we find that the formation of formate goes through a surface-bound hydrogen in an Eley-Rideal/Heyrovsky like mechanism with CO_2 being activated near the surface, or as a surface reaction with $*CO_2$. This mechanism is in stark contrast to mechanisms proposed for formate production on more oxophilic post-transition metal, as e.g. Pb [98] and Sn [99]. Here, it has been proposed that their oxophilicity allow them to stabilize CO_2 via the oxygen atoms ($*OCO$) and subsequently protonate the carbon to produce formate [100][2]. On PdH however, we were not able to stabilize $*OCO$ at any potential despite rigorous sample of possible adsorption sites. This is consistent with the strong destabilization of $*HCOO$ observed when going from Pd to PdH. Instead, the reaction mechanism involving CO_2 hydrogenation towards formate was identified as an outcome of the transition state searches starting from both solvated (planar) and adsorbed (bent) CO_2. The transition states are similar in nature, as the (partially) activated CO_2 reacts with a surface $*H$, but relative barriers of the two changes slightly due to $*CO_2$ having a larger dipole than the CO_2 activated from its dissolved state. The relative barriers of the $*H$-CO_2 state are shown in Figure 4.8, with a change in RDS around $-0.7\,V$ vs RHE. This means that formate is produced exclusively through the solvated CO_2 as a nucleophilic attack by a surface hydrogen on the desorbed carbon, at the potentials where formate is shown to be formed experimentally. This transition state has a potential response of $0.2\,eV/V$, with most of the charge injection leading to the formate occurring after the transition state, as shown in Figure 4.9 (b). In a sense, the RDS is almost *quasi*-chemical in nature, akin to a chemical (near) surface reaction, with only a very low field response. Of course that is only half of the truth, as there is still a stabilizing effect from the dipole interacting with the field, and the reaction relies on the electrochemical environment through the PdH formation to happen.
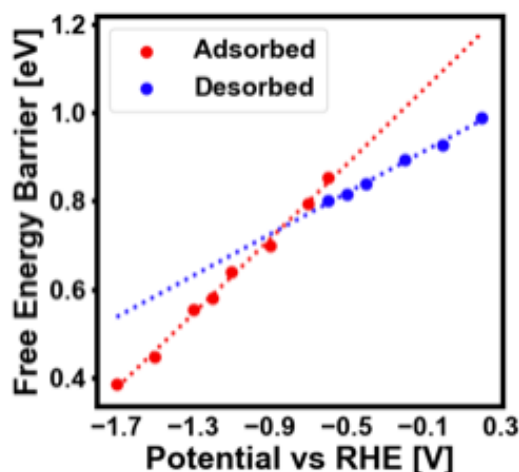
Figure 4.8: Competition between barriers starting from desorbed vs adsorbed CO_2. Barriers computed with SJM for two possible mechanisms, either starting from desorbed (blue) or adsorbed (red) CO_2, reacting with a surface proton and desorbing as $HCOO^-$. The former has a potential response of $0.20\,eV/V$, the latter $0.42\,eV/V$.

---

[2]The CO_2 binding motif is the topic of interest of another part of this thesis, see Chapter 5.
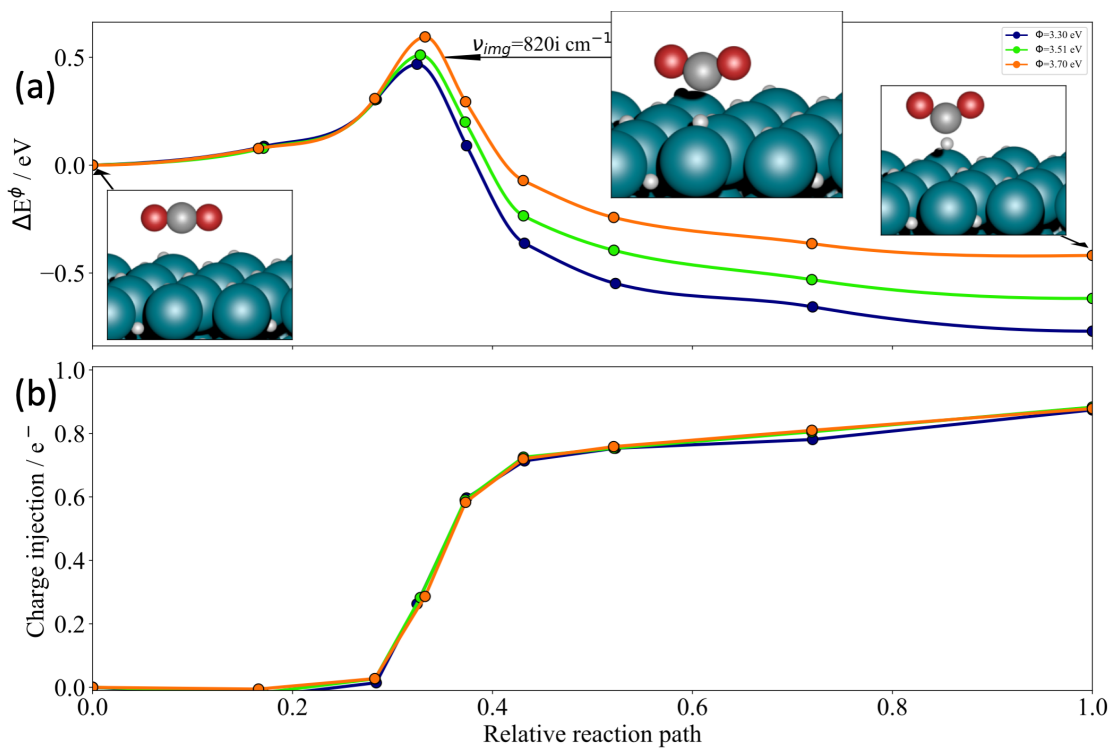
Figure 4.9: Minimum energy path and charge injection for HCOO$^-$ formation on PdH

(a) Calculated minimum energy pathways of the CO_2 hydrogenation step towards formate, along with inserts of initial, transition and final state structures. (b) The accompanied electron injection into the unit cell in the course of the reaction in order to keep the potential constant. Three different potentials are shown with varying colors.

The formation of CO was found to proceed through *CO_2 bent on the surface, binding via the carbon, followed by two PCET steps to first *COOH then *CO followed by CO desorption. We assume that the PCET step from *CO_2 to *COOH has no kinetic barrier, as the negative oxygens on the *CO_2 allows for facile oxygen protonation [83]. The full reaction pathways towards both CO and HCOO$^-$ is shown in Figure 4.10. At low overpotentials, the formation of *COOH is identified as the rate limiting step. This however exhibits a relatively strong potential response of 1.13 eV/V, and eventually CO_2 adsorption is expected to be rate limiting. Comparing the pathways at 0 V, we find formate to be the preferred product, as the barrier to formate is roughly 0.3 eV lower in energy than the *COOH state. However, as we go to increasingly negative potentials the competition between the electrochemical PCET step to *COOH and the hydrogenation towards formate leaves no hope for formate. Instead, with a difference in potential response of almost 1 eV/V, CO production quickly dominates, as the FED also shows and at -0.5 V, the CO pathway is already more stable than the HCOO$^-$ pathway.

Based on the reaction energetics described above, we design a microkinetic model using CatMAP [51] to quantify the selectivity and activity changes with potential,

Electrochemical CO_2 Reduction to Two-Electron Products
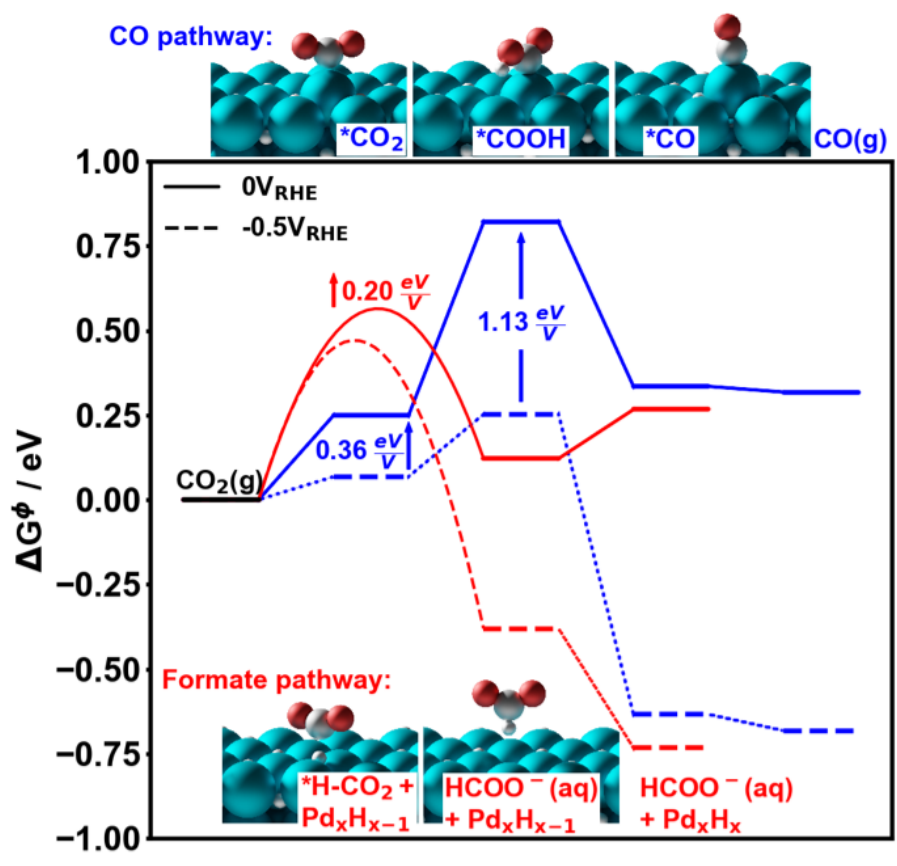
Figure 4.10: Free Energy Diagram for CO_2 to CO and $HCOO^-$

Free Energy Diagram for CO_2 reduction to CO (blue) and $HCOO^-$ (red), at 0 (full line) and -0.5 (dashed line) V vs RHE, along with potential responses of select intermediates. Inserts with illustrations of reaction intermediates are shown for the respective pathways.

shown in Figure 4.11. The model shows the CO_2R activity as turnover frequencies (TOF) and selectivity as the TOF of product i over the sum of the two TOF's. Since we cannot expect perfect, quantitative agreement between theory and experiment [101], especially for electrochemical barriers that are notoriously tricky, we show how both activity and selectivity would change if the *H-CO$_2$ barrier was changed by up to ± 0.1 eV, indicated by the blue ribbons n Figure 4.11. The kinetics show that the total activity (given as the sum of the TOF's) increase at more negative potentials, while $HCOO^-$ is predicted to be the main product at potentials less cathodic than -0.35 V. The increase in TOF for CO is significantly larger than for $HCOO^-$ and thus this analysis indicates the CO_2R selectivity towards CO should increase at more negative potentials. This is driven by the difference in potential-dependent stabilization of the RDS described above. The results obtained from this model are in good agreement with the experimental data shown in Figure 4.5, although the model predicts CO to dominate at slightly less negative potentials than the experimental data shows. However, as the uncertainty bands in the kinetic model shows, a difference in energy of ± 0.1 eV, leads to a roughly 0.2 V difference in the selectivity switch. Qualitatively, we see exactly the same trend though, that the

CO₂R on PdH will initially exclusively produce formate but over a few 100 mV a rapid shift occurs and beyond that we selectively produce CO.
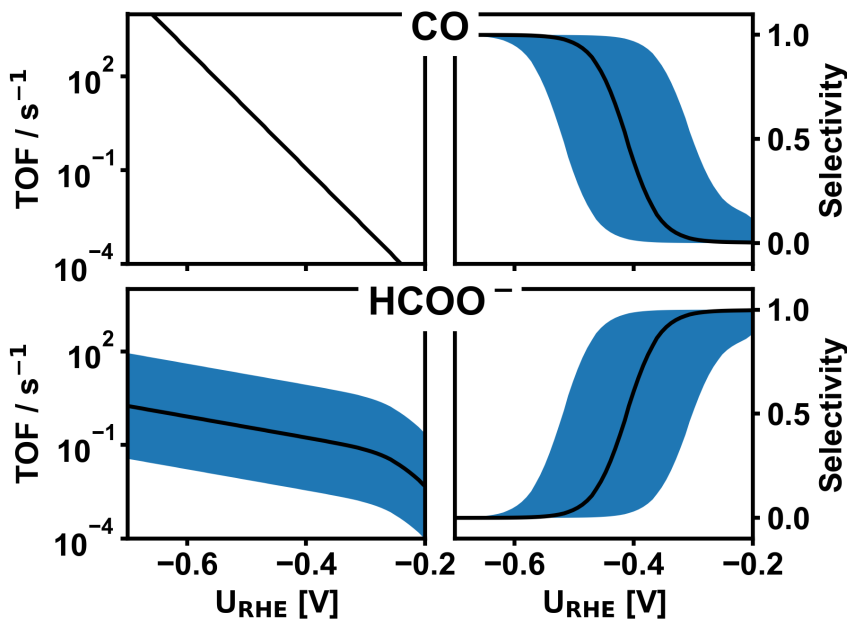
Figure 4.11: Activity and selectivity towards CO and HCOO⁻

CatMAP data showing turnover frequencies (TOF) (left) and selectivities (right) for CO (top) and HCOO⁻ (bottom), as a function of potential vs. RHE. The blue shaded region shows the uncertainty in TOF and selectivity calculations from a variation of the barrier for CO_2 surface hydrogenation by $+/- 0.1eV$.

4.4 Conclusion

With this study, we show that the palladium electrode undergoes massive structural changes at reaction conditions, essentially forming a new material, palladium hydride, which theory predicts to be much more active in CO₂R than the pure metal. We characterize the phase changes as the potential changes and describe what makes palladium unique in its ability to form hydrides in contrast to otherwise similar metals. We estimate the *H coverage and identify the β-phase of PdH(111) to be the catalytically active surface and show why CO poisoning is observed in CO₂R on palladium. For the CO₂R activity, we show that the proposed reaction mechanism to formate on post-transition metals is not feasible on PdH and identify an alternative reaction mechanism based on CO_2 hydrogenation from the hydrogen-rich PdH surface. Additionally, we show how the quasi-chemical nature of this step makes the competition with the electrochemical PCET step an impossible task, which leads to a rapid shift in selectivity from HCOO⁻ to CO. Overall, this study truly shows the massive influence that the electrostatic potential has on the electrochemical environment. From a materials science perspective, it shows the importance of characterizing and understanding your material *at reaction conditions*, as it might be fundamentally transformed under these. From an (electro)chemistry

and catalysis perspective, it shows what a powerful driving force the potential can be and competing step with large differences in potential stabilization can lead to very rapid changes in selectivity. This reaction is almost a text-book example of this, as we completely change the product distribution over a few 100 meV, thus highlighting the importance of being able to control and manipulate the potential in electrocatalysis.

Electrochemical CO$_2$ Reduction to Two-Electron Products

5 Getting Active With CO₂

CO₂ Adsorption and Conversion

In this chapter we explore the binding motif of CO_2, how it can be stabilized and what role CO_2 binding plays in terms of not only the activity but also the selectivity further down the reaction pathway. This chapter is the outcome of a collaboration with the SUNCAT Center for Interface Science and Catalysis with Co-Director Frank Abild-Pederson. Parts of this research was conducted at SLAC/Stanford as part of an external research stay.

5.1 Background

The selectivity of CO_2 Reduction is a topic of considerable interest in CO_2 reduction, and many different reaction mechanisms have been proposed to explain what governs this selectivity. It is generally accepted, that the initial reduction of CO_2 will either lead to the formation of formic acid (or formate depending on the pH) or carbon monoxide, and that the latter can then be further reduced to form other C_1 and/or C_{2+} products, while formate, at least in electrochemistry, is not believed to be readily reducible [20], [89]. What best describes this selectivity split, and just as importantly *why*, remains elusive however. Experimentally, CO and $HCOO^-$ have similar onset potentials and both increase at low overpotentials, until $HCOO^-$ production dies down again and CO is reduced further at lower potentials [102]. One suggestion is to use the *COOH as a descriptor for the CO production rate and *OCHO as the descriptor for formate, as shown in Figures 5.1a and 5.1b [100].

(a) Volcano plot for CO   (b) Volcano plot for $HCOO^-$
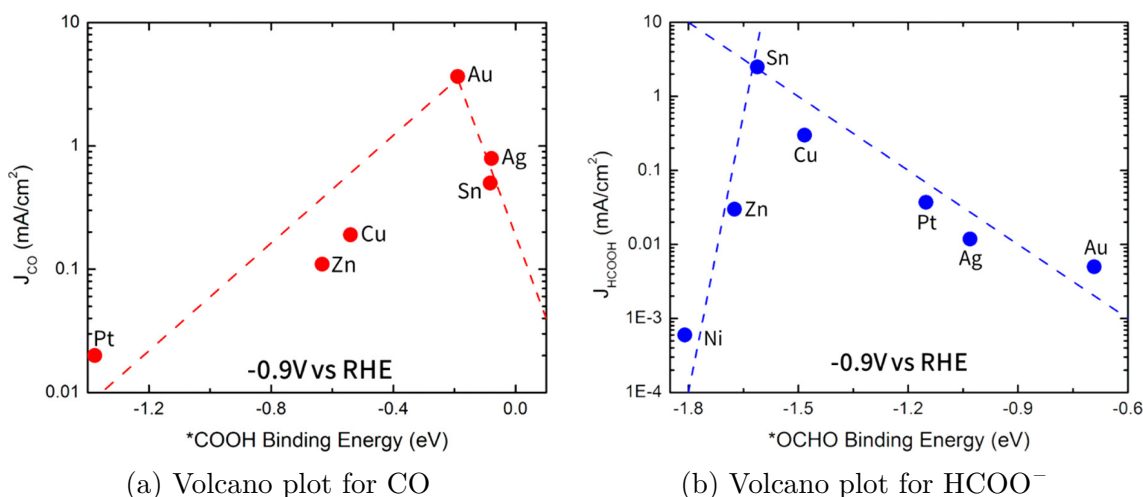
Figure 5.1: Possible 2e- product descriptors, *OCHO/*COOH

Volcano plots using *COOH as a descriptor for CO production and *OCHO for $HCOO^-$ production. Reprinted with permission from [100]. Copyright 2017 American Chemical Society.

As the figures show, the activity towards CO nicely correlates with the binding energy of *COOH, with an optimum around $-0.2\,\mathrm{eV}$, while the activity towards formate correlates well with the *OCHO binding energy. This would indicate that the oxygen-bound intermediates play a crucial role in the CO_2 reduction to formate. One thing that is clear however, is that the thermodynamics of these two states are not enough to understand why some metals predominantly produce formate and why some produce CO (or other products that go through to *CO intermediate. This is clear when we look at just a simple parity plot to see how the *COOH and *HCOO/*OCHO binding energies scale, as shown in Figure 5.2a. This shows, that the binding energy of *OCHO is lower than that of *COOH for all the metals that are classified as CO_2 reduction catalysts, that is blue for CO, yellow for formate and turquoise for further reduced species. Red is H_2 production. Thus, if the kinetics leading up to this was similar, we would expect all of CO_2 reducing metals to produce formate. But only a little more than half of them do, and from the plot we cannot distinguish the carbon products based on these two energies alone, so clearly there is something that we are missing. And indeed there is, as we both need to activate (bend) the CO_2 molecule, bring it to the surface and protonate/hydrogenate it before we reach the *COOH and/or *OCHO states. Additionally, when we look at the scaling of the *COOH and *H binding energies, seen in Figure 5.2b we see a better product separation, where the metals that bind H the best do HER, followed by Cu (the only metal here that makes further reduced products), then CO producers and ultimately formate producers. Notably, all the carbon reducers have relatively similar *COOH binding energies, except for Hg, but ultimately this plot would suggest that the weakening of the *H binding will aid in producing formate rather than CO, if these are indeed the relevant for CO_2 reduction [103].

(a) *HCOO and *COOH scaling (b) *COOH and *H scaling
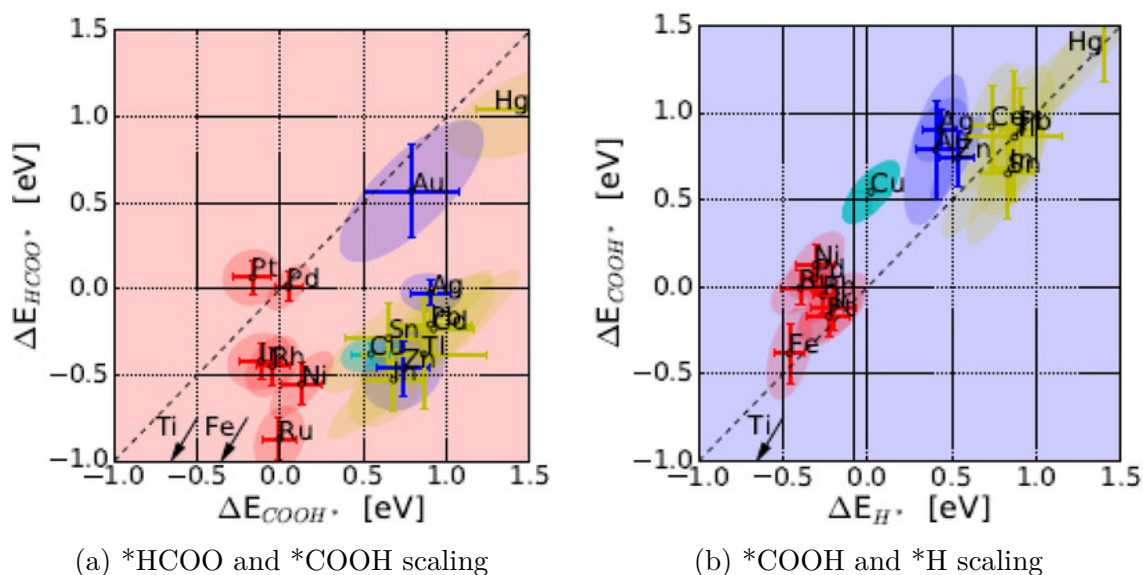
Figure 5.2: Possible 2e- product descriptors, *HCOO/*COOH and *COOH/*H Plots of scaling lines for product separation of products fromCO_2R on various metals. Red is hydrogen, yellow is formate, blue is is CO and turquoise is carbon products beyond 2e- products. Reprinted with permission from [103]. Copyright 2017 John Wiley and Sons.

These two separate findings have been unified to some extent by the proposal to use *CO/*H binding energies, as these scale[1], against *OH binding energies, which scales with *OCHO. Under the assumption that *OCHO formation is rate limiting and completely chemical in nature, we can distinguish regions of formate producers from CO/*CO producers, as we can now stabilize *COOH formation with potential, to the extent that it ultimately becomes more stable than *OCHO [20].

This is not in any ways an exhaustive listing of the possibilities and crucially, we are in all three examples basing our descriptors on species involving protons, skipping the kinetics of CO_2 adsorption entirely, in spite of the fact that CO_2 adsorption is believed to be the rate limiting step on several of the most interesting CO_2RR catalysts including gold and copper [83], [104], [105] A schematic outline of just some of the possible routes from CO_2 to *COOH/*OCHO is given below in Figure 5.3.
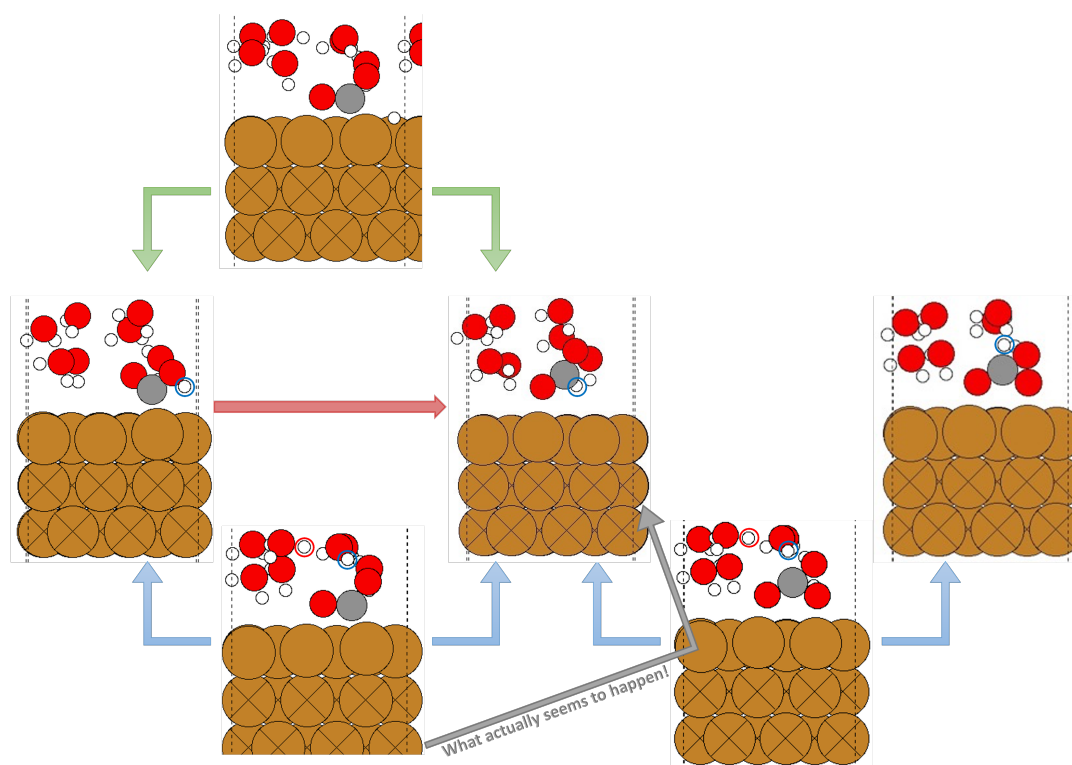
Figure 5.3: Possible hydrogenation/protonation routes

Green arrows is for hydrogenation (chemical), blue for protonation through PCET (electrochemical) and red is neither, but instead an internal rearrangement of the hydrogen on CO_2.

Experimentally, a study applying surface-enhanced Raman spectroscopy on Cu was only able to detect peaks believed to stem from the *CO_2 motif shown on the bottom left of Figure 5.3 [106], indicating the *OCO shown on the bottom right might not be present on the surface, or at least that the lifetime of *OCO on the surface

---

[1]This is not true for the post-transition metals that produce formate. Instead, we once again see that the formate producers bind *CO similar to the CO producers, but bind hydrogen worse.

is very low, indicating that it is rapidly reduced upon formation. At the same time, kinetic isotope labeling experiments concluded that the RDS to $HCOO^-$ does not involve H, which would rule out surface hydrogenation from the top left structure as the RDS [104]. This could lead us to conclude that the pathway to $HCOO^-$ should go through a PCET step from the bottom left $*CO_2$ structure to the structure in the center of Figure 5.3. However, this is really not a very facile reaction. First of all, the oxygen not bound to the surface has a partial negative charge and would readily accept a proton, while protonating the carbon would require breaking its bond with the surface and rotating the $*CO_2$, and even so, the carbon would be more positive than the oxygen. This is something that should be very kinetically unfavorable both in terms of the steric effect and electrostatics. In fact, when we attempted to simulate this barrier with SJM, the minimum energy path appeared to pass through a local minimum corresponding to the $*OCO$ state, with the main barrier being $*CO_2$ to $*OCO$. It should be noted that we could not ultimately converge this full path, so this is merely meant to serve as a qualitative assessment of the kinetics of CO_2 to $*OCHO$.

5.2   Accounting for the CO_2 kinetics

To expand on the previous works, our aim is to describe the chemical as well as electrochemical steps that lead up to the presence of $*OCHO/*COOH$ on the surface. First, let us take a step back and discuss *why* we often start from the protonated species. One of the main reasons is that it is not trivial to bind CO_2 on some of these surfaces, in fact on most pure metals, CO_2 would prefer not to chemisorb, at least not at low potentials (which is also why its adsorption is the RDS on several of the metals). It is a quite stable linear molecule with two strong double bonds and as it is activated by bending and adsorbing on a surface, the energy we gain from hybridizing with the surface may not be large enough to offset the energy penalty we pay in terms of loss of bond order when we bend it. Thus, we often need *something* in our system to aid the activation, adsorption and stabilization of CO_2.

Luckily for us, the CO_2 adsorbed state is one of the few states in CO_2R that has a strong interaction with the interfacial field which contributes to stabilizing the adsorbed state [83], [107], and with this we can model the $*CO_2$ state in different ways. Either by using explicit charging components such as ions or protons or by using a charged implicit solvation model. For this project we have used GPAW [34], [52] to design a simplified model for the adsorption and then the SJM module [59] included in ASE [40] to get potential/field dependent adsorption energies.

The goal of this project is to better understand and describe the CO_2 adsorption process on transition and post-transition metals. More specifically, we would like to probe the hypothesis, that the oxygen-binding intermediates are crucial to the formate production. Since the binding energies of $*OCHO$ is generally quite negative, we assume that one of the steps leading up to $*OCHO$ is the RDS, probing whether it is possible that formate is produced via CO_2 bound via the oxygens, labeled $*OCO$, as opposed to the most frequently looked-at configuration of CO_2

bound via the carbons. Intuitively, we would expect the dipole to be opposite and with this, that *OCO would be destabilized at cathodic potentials. In gas phase, just looking at the dipole of the molecule, that should certainly be the case, as it is dependent on orientation. On the surface, the interaction might change behavior. We would like to probe that and see if we can understand the binding process on the basis of a simple model.

5.3   Modeling CO_2 on a surface

Since we cannot stabilize CO_2 on the surface directly from gas phase calculations containing just the metal slab and CO_2, we set up a model where we systematically vary the bonding angle of CO_2, fixing the O-C-O angle, but allowing the rest of the system to freely relax, apart from the fixed atoms in the bottom of the slab. Upon bending, several different components of the system may contribute to the overall stability:

Loss of bond order in CO_2: Upon bending, we break the symmetry of the CO_2 molecule and the internal bond order of the molecule decreases, weakening the C=O bonds, destabilizing the molecule.

Gain of adsorbate/surface interactions: Upon bending, the destabilized (or, *activated*) molecule will start interacting more strongly with the surface, hybridizing with the surface, stabilizing the system.

Interaction between E-field and CO_2 dipole: Upon bending, the partial positive charge on the carbon atom and the partial negative charges on the oxygen atoms creates a dipole within the CO_2 molecule. This dipole will interact with an electric field with the size and sign of the effect depending on the orientation of CO_2 relative to the field.

Interaction between E-field and surface dipole: In addition to the molecular dipole that appears upon bending, it is also possible that the hybridization between the surface and the CO_2 molecule will create a total surface dipole of the system that is different from the molecular dipole. The magnitude and direction of this dipole is not clear and will possibly depend on the orientation of *CO_2.

More factors likely play a role such as polarizability and solvation, and several of these effects may change once we for instance change the charge of the metal by going to more cathodic potentials. Treating this however, would require more sophisticated methods that increase the computational costs and may introduce other sources of uncertainty, so this is meant to serve as a simplified model capturing the main energetic contributions and trends.

Next, to sample CO_2 adsorption, we set up three distinct systems, two where we bent the two oxygens upwards in the z-direction in vacuum and adsorbed on a copper step respectively, and one where we bent them downwards on a copper step, going from 180° to 120° in steps of roughly 6°.

The first relationship we get is stability as a function of angle. The gas phase is destabilized a lot, adsorbates less as we expected given the hybridization as shown in Figure 5.4(a) and Figure 5.5(a-b) for gas phase and adsorbed species respectively. *OCO is destabilized less than *CO$_2$, but both are significantly destabilized to the point where bonding seems quite unfeasible. Additionally, we get out dipoles. For CO$_2$ (g), this is nicely linear as shown in Figure 5.4(b). For the adsorbates, the fit of the raw data, seen in Figure 5.5(c-d) is less clear. The orientation of CO$_2$ means that the dipole of *OCO initially increases while *CO$_2$ is constant decreasing, with a kink however, when the effect of hybridization becomes significant. Both dipoles eventually become negative with enough bending/hybridization. Finally, the molecule-metal distances in Figure 5.5(e-f) show that CO$_2$ will be completely desorbed when the angle is close to 180°. In fact, below a bending of 25°, both *CO$_2$ and *OCO show a jump in bond length and leave the surface.
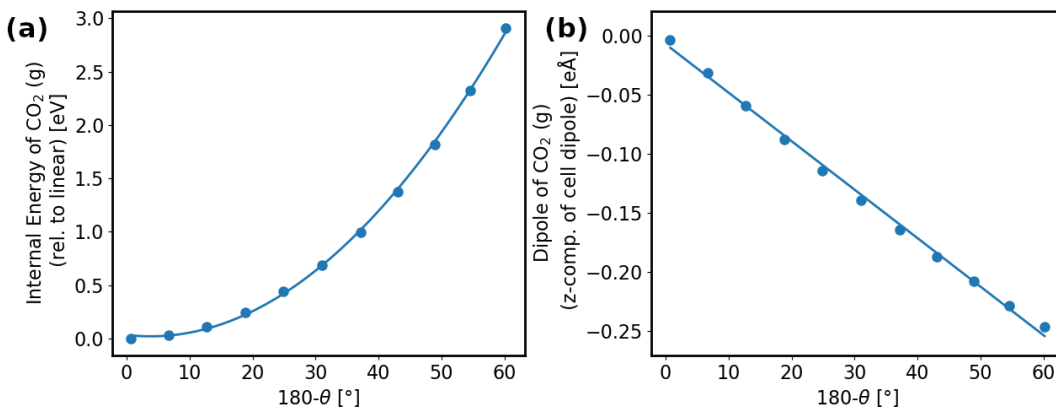
Figure 5.4: Energies and dipoles for CO$_2$ (g)

(a) is energy change relative to linear and (b) is total system dipoles in the z-direction for CO$_2$ (g).

To isolate the effect of adsorbate/surface hybridization, we subtract out the energy and dipole changes associated with the CO$_2$ molecule, from the gas phase calculations as $E_{hyb} = E_{tot} - E_{gas}$ for the energies and $\mu_{hyb} = \mu_{tot} - \mu_{gas}$, where $\mu_{gas,OCO} = -\mu_{gas,CO_2}$ as the rotation of CO$_2$ on *OCO relative to CO$_2$ means that the contribution from the molecular dipole in *OCO is equal in size but opposite in sign. This hybridization contribution to energy and dipole is shown in Figure 5.6, along with E_{tot}, E_{gas} and μ_{tot}, μ_{gas} for energies and dipoles respectively.

As the figures show, the hybridization does help stabilize both *CO$_2$ and *OCO significantly, relative to the gas phase molecule and in the absence of a field, *OCO is more stable on the Cu(211) surface than CO$_2$. Neither of them are more stable at any given angle than the reference of the desorbed/physisorbed linear CO$_2$ however. This once again underlines the significance of the electric field in activating and adsorbing CO$_2$. Additionally, upon hybridizing with the surface both configurations obtain favorable surface dipoles as charge is transferred from the metal to the adsorbate. And even in the case of *OCO, the dipole of *OCO on the surface becomes larger than the molecular CO$_2$ dipole alone, even in its most favorable ori-
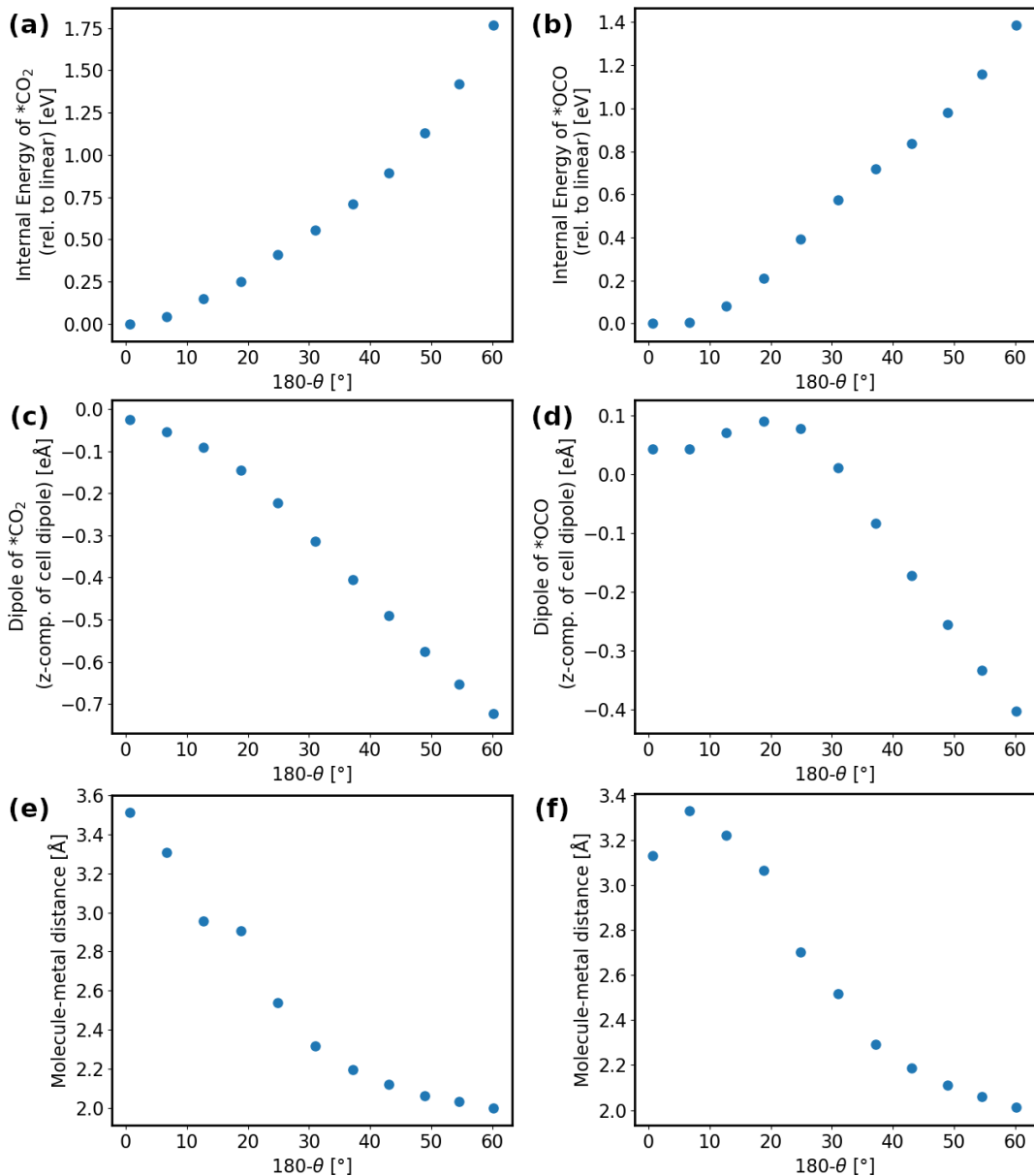
Figure 5.5: Energies, dipoles and distances for *CO$_2$ and *OCO

Left column is data for *CO$_2$ (a,c,e), right is *OCO (b,d,f). From top to bottom the rows show data for energy change relative to linear CO$_2$ (a-b), total system dipoles in the z-direction (c-d) and distances from the surface for *CO$_2$ (calculated as M-C distance) and *OCO (calculated as average M-O distance) (e-f).

entation (aligned with the field in the z-direction). From this we conclude that both configurations are possible in theory, given a strong enough field, and that the competition between *CO$_2$ and *OCO will depend on the relative contributions from hybridization, which favors the formation of *OCO, similarly to what is observed for *OCHO vs *COOH, and dipole-field interactions which favors CO$_2$ due to the orientation of the molecule on the surface.

We split the total energy into contributions from the molecular bond order loss,
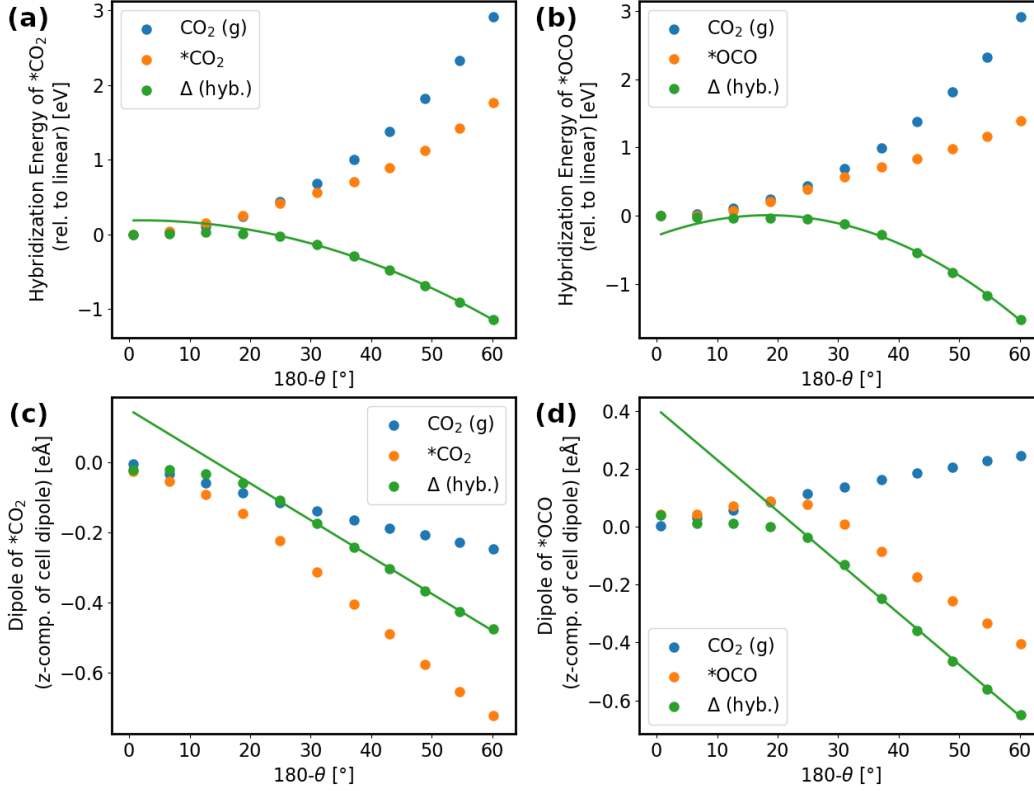
Figure 5.6: Relative energies and dipoles for *CO_2 and *OCO
Left column is data for *CO_2, right is *OCO. Top show hows change in hybridization energy relative to linear CO_2, bottom shows dipoles in the z-direction induced by surface hybridization.

given by the gas phase energies, and the energy gain from hybridization and fit both to a 2nd order polynomial, using only the adsorbed *CO_2 and *OCO structures for the calculation of the hybridization energies. This line of best fit for each of $CO_2(g)$, *CO_2 and *OCO is shown on Figure 5.4(a), 5.6(a) and 5.6(b) respectively.

$$\Delta E_{BO,CO_2(g)} = A_{BO}\tilde{\theta}^2 + B_{BO}\tilde{\theta} + C_{BO} \tag{5.3.1}$$

$$\Delta E_{hyb,i} = A_{hyb,i}\tilde{\theta}^2 + B_{hyb,i}\tilde{\theta} + C_{hyb,i} \tag{5.3.2}$$

Where $\tilde{\theta}$ being the bending angle (i.e. $180° - \theta$) and $E_{hyb,CO_2} = E_{tot} - E_{BO,CO_2(g)}$.

Using a similar approach, we make a linear fit for the dipoles, fits shown in Figure 5.4(b), 5.6(c) and 5.6(d) respectively.:

$$\Delta\mu_{gas} = b_{gas}\tilde{\theta} + c_{gas} \tag{5.3.3}$$

$$\Delta\mu_{hyb,i} = b_{hyb,i}\tilde{\theta} + c_{hyb,i} \tag{5.3.4}$$

With $\mu_{hyb} = \mu_{tot} - \boldsymbol{\mu}_{gas}$. For *OCO, the molecular dipole is opposite relative to z than the gas phase calculation, meaning $\boldsymbol{\mu}_{gas,OCO} = -\mu_{gas,OCO}$. The coefficients of the different fits are shown in Table 5.1.

Table 5.1: Coefficients for energy and dipole fits.

	A[eV] / a[eÅ]	B[eV] / b[eÅ]	C[eV] / c[eÅ]
$\Delta E_{BO,CO2}$	$8.968 \cdot 10^{-4}$	$-0.6823 \cdot 10^{-2}$	0.0335
$\Delta E_{hyb,CO2}$	$-3.956 \cdot 10^{-4}$	$0.1645 \cdot 10^{-2}$	0.1867
$\Delta E_{hyb,OCO}$	$-8.888 \cdot 10^{-4}$	$3.2775 \cdot 10^{-2}$	-0.2944
$\Delta \mu_{gas,CO2}$	-	$-0.7308 \cdot 10^{-2}$	-0.0073
$\Delta \mu_{hyb,CO2}$	-	$-1.0502 \cdot 10^{-2}$	0.1504
$\Delta \mu_{hyb,OCO}$	-	$-1.7722 \cdot 10^{-2}$	0.4093

In order to quantify the energetic contribution from the dipole, we must first consider the coupling of a dipole to an electric field. The dipole on CO_2 appears when it is bent, as the vector sum of the bond dipoles of the two C=O bonds, making the carbon partially positively charged and the oxygens partially negatively charged. At 180° they offset, but at θ<180°, the vector sum is $\neq 0$, but has length **d** and associated dipole moment **μ**, as seen in Figure 5.7.
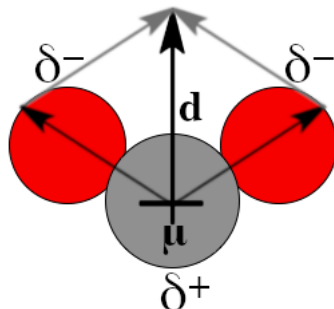
Figure 5.7: Illustration of *CO_2 dipole

Schematic of the bent CO_2 molecule showing the partial charges on the atoms as ∂^+ and ∂^- for carbon (positive) and oxygens (negative) respectively. Bond dipoles are indicated with black arrows, grey arrows indicate the vector sum that results in a total dipole moment **μ** of length **d**, with the magnitude and direction illustrated by the crossed black arrow, cross/plus indicates positive end.

The dipole can be seen as two charges separated in space by a distance **d**, with **μ** = q**d**. As the CO_2 molecule is overall charge neutral, the charge at the negative end has the same magnitude as the charge at the positive end. The work required to bring a point charge into a potential at point **r** is given as:

$$W = Q\phi(\mathbf{r}) \tag{5.3.5}$$

If we assign the negative end a charge -q, the positive end a charge q and place the negative end at r=0, we get a total energy of:

$$E_{\boldsymbol{\mu}} = q\phi(\mathbf{d}) - q\phi(0) = q(\phi(\mathbf{d}) - \phi(0)) \tag{5.3.6}$$

This is equivalent to a line integral over the electric field, as the work we need to overcome is merely force times distance and the force acting on a charge q is related

to the electric field as $\mathbf{F} = q\boldsymbol{\mathcal{E}}$:

$$E_{\boldsymbol{\mu}} = q \int_0^{\mathbf{d}} \boldsymbol{\mathcal{E}} \, \mathrm{d}\mathbf{l} \tag{5.3.7}$$

Assuming the dipole is ideal (infinitesimal) separation such that the field is uniform, the energy associated with the dipole is:

$$E_{\boldsymbol{\mu}} = q\mathbf{d}\boldsymbol{\mathcal{E}} = \boldsymbol{\mu}\boldsymbol{\mathcal{E}} \tag{5.3.8}$$

Now, the total energy of the system E is the adsorption/hybridization energy (E_0) plus the energy contribution from the dipole $E_{\boldsymbol{\mu}}$:

$$E = E_0 + \boldsymbol{\mu} \cdot \boldsymbol{\mathcal{E}} \tag{5.3.9}$$

$$\Downarrow asm. \ \boldsymbol{\mu} \ and \ \boldsymbol{\mathcal{E}} \ opposite \ in \ z\text{-}direction$$

$$= E_0 - \mu\mathcal{E} \tag{5.3.10}$$

As we usually do not measure the field directly, but rather the potential ϕ_M, which is related to the field through the surface charge density σ as:

$$\sigma = \epsilon_0 \mathcal{E} \qquad \textcolor{blue}{\textbf{\textit{Gauss' Law}}} \tag{5.3.11}$$

$$c_H = \frac{\mathrm{d}\sigma}{\mathrm{d}\phi_M - \phi_{PZC}} \qquad \textcolor{blue}{\textbf{\textit{Helmholtz Capacitance}}} \tag{5.3.12}$$

$$\Downarrow Assuming \ constant \ c_H$$

$$\sigma = c_H \left(\phi_M - \phi_{PZC} \right) \tag{5.3.13}$$

$$\Downarrow comb. \ (5.3.11) \ and \ (5.3.13)$$

$$\mathcal{E} = \frac{c_H \left(\phi_M - \phi_{PZC} \right)}{\epsilon_0} \tag{5.3.14}$$

Where ϕ_{PZC} is the potential of zero charge and ϵ_0 is the vacuum permittivity.

If we assume a capacitance of 20 µF/cm^2, we get $\mathcal{E} = 1.196\Delta\phi[\text{Å}^{-1}]$ and with this can compute and compare values for the *CO$_2$ vs. *OCO energies. If we for instance are at a potential 1V below the PZC, and we assume a bond angle of 130°, the energy contribution from the *CO$_2$ system dipole would be $1.196\,\text{V}/ \cdot (-0.480\,\text{e}) = -0.574\,\text{eV}$, meaning that we stabilize the system with roughly 0.6 eV/V. For the *OCO system, which has a destabilizing effect from the molecular dipole, this contribution is only $-0.316\,\text{eV}$. The contributions from hybridization and bond order loss are 1.21 eV and 1.06 eV for *CO$_2$ and *OCO respectively, so ultimately *CO$_2$ is the most stable of the two at this potential and angle, and in fact for any potential cathodic of $\approx$-0.4V below the PZC, for this chosen angle. We conclude, based on this model, that due to charge transfer during hybridization it is in fact possible to stabilize the *OCO binding motif on a metal surface, through the interfacial field. For this specific surface however, we can also conclude that although the adsorbate/surface hybridization favors the *OCO motif over the *CO$_2$, the inclusion of the dipole/field interactions will favor CO$_2$ when going cathodic. Additionally, the *OCO motif will inevitably have to pass through a state upon bending, where the

total system dipole is positive, which would be destabilized with field at cathodic potentials, meaning it needs to cross a barrier from the linear state, that the *CO$_2$ motif does not. This could make CO$_2$ the kinetically preferred product even when the thermodynamics are similar.

As an addendum, it is worth noting, that even though we can decouple the contributions here to some extent and qualitatively describe the relative stabilities, this model does not quantitatively describe *CO$_2$. Even at potentials where CO$_2$ reduction is expected to occur, this model predicts both *CO$_2$ and *OCO to be less stable than the linear, desorbed state. Refining the model to be more quantitative might require accounting for factors such as polarizability or changes to the hybridization energy upon charging of the surface.

5.4   Modeling CO$_2$ with SJM

In addition to the analytical model, we have also computed constant-potential energetics using the SJM module to get a more quantitative understanding of the CO$_2$ adsorption. For the Cu(211) facet, we adsorb both motifs of CO$_2$ across the available top, hollow and bridge sites and find that the undercoordinated top sites bind CO$_2$ most favorably for both motifs. We also compute 15 binding energies for each intermediate across a potential range from 0 V to -1.4 V vs. SHE, in steps of 0.1 V, to get the stabilization of each intermediate with potential. Linear fits are shown for *CO$_2$, *OCO and *COOH in Figure 5.8. At low negative potentials both *CO$_2$ and *OCO desorb, once again showing the importance of including the field. The desorbed states have not been included in the adsorbate fits. With the linear fit, we assume that we can neglect polarizability, which seems to hold for both *CO$_2$ and *OCO, while *COOH does appear to show some polarizability at negative potentials. The fits show that *CO$_2$ has the largest field stabilization with 0.63 eV/V, followed by *OCO with 0.52 eV/V and finally *COOH with 0.36 eV/V. It should be noted however, that *COOH also benefits from the destabilization of the proton/electron couple, giving it a total stabilization with potential of 1.36 eV/V.

With the potential dependence, we can construct free energy diagrams at varying potentials, using CHE to account for the change in chemical potential of the proton-electron pair with potential. In terms of the suggested competing mechanisms, we are interested in the selectivity between *COOH formation, which is assumed to exclusively reduce to *CO/CO(g) and HCOO$^-$ formation. For the *COOH formation we assume the reaction mechanism is a CO$_2$ adsorption step followed by a PCET step to from *COOH. It is assumed that the barriers of the PCET steps are negligible in both pathways as the partially negative *CO$_2$/*OCO adsorbates enables facile protonation [83].

For HCOO$^-$ formation, a similar pathway is proposed through *OCO to form *OCHO, which desorbs as HCOO$^-$ as the final product rather than formic acid, as CO$_2$ reduction usually takes place around pH=7, well above the formic acid pKa of 3.75. As the simplified model suggested that *OCO might not adsorb strong
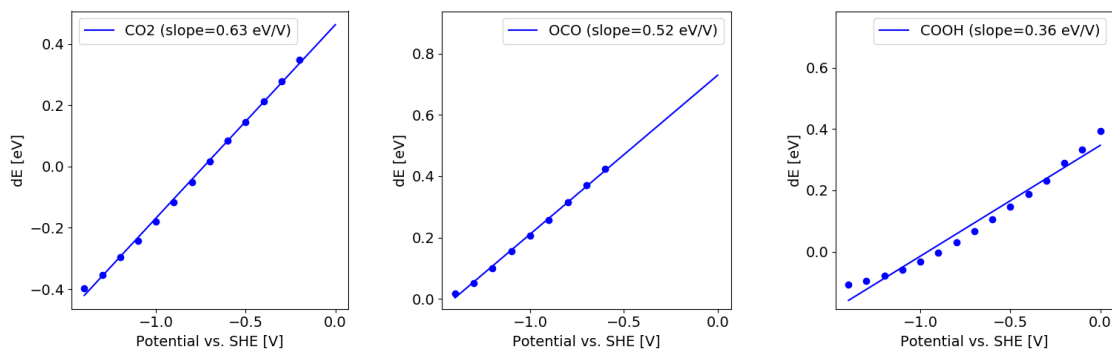
(a) Linear fit of ΔE *CO$_2$ (b) Linear fit of ΔE *OCO   (c) Linear fit of ΔE *COOH

Figure 5.8: Linear fits for carbon adsorbates

Linear fits of *CO$_2$, *OCO and *COOH from -1.5 to 0 V vs. SHE. For desorbed structures, the line of best fit has been extrapolated to 0 V vs. SHE.

enough to compete with *CO$_2$, we also consider an alternative route where HCOO$^-$ is formed through a reaction with *H, either through a Langmuir-Hinshelwood step with *CO$_2$ or through an Eley-Rideal/Heyrovsky type step directly from desorbed *CO$_2$. This is similar to the step found to be the RDS for formate production from PdH, as discussed in Chapter 4. The competition between the two steps is shown in Figure 5.9a with formation free energies for both transition states. The dots indicate calculated values, while the lines are fits. The barriers of the adsorbed step are initially higher close to 0 V, also indicated by the lack of data points at low potentials where we struggle to stabilize *CO$_2$. However, the field stabilization of the transition state of the adsorbed pathway is slightly larger, so with potential the adsorbed route becomes favored. But ultimately the barriers remain close in energy for the potential region considered.

Finally Figures 5.9(b-d) show the reaction pathways at varying potential from 0.0 V to -1.0 V vs. RHE. From this, we can see that although the *OCO and *COOH are quite close in energy at 0 V vs. RHE, *OCO is still above *COOH in energy and is never expected to be the preferred CO$_2$ reduction pathway. Both of the *H routes are however below the *COOH at 0 V, so from this we would expect this facet to produce formate over CO at low potentials. Once we reduce the potential to -0.4 V, we enter a region where *H is stable on the surface as the only intermediate. Both *CO$_2$ and *COOH are very close to thermoneutral however, and under the assumption that the PCET's remain facile at these potentials, the CO production could very well be competitive. At the final potential considered, -1 V, all intermediates, except for *OCO, are expected to be negative in formation energy on the surface. Here, there would be a strong driving force for the protonation steps, while the two steps towards formate still have non-negligible barriers. Whether these are still competitive with the PCET barriers has not been quantified here. But it is clear that with potential we stabilize the electrochemical pathway towards CO. At the same time, the electrochemistry in the formate production mainly takes place before the RDS, with the *H stabilization, while the chemical *H+CO$_2$ barriers are less

Electrochemical CO$_2$ Reduction to Two-Electron Products

affected by potential.

(a) Relative barriers

(b) FED at 0.0 V vs. RHE

(c) FED at -0.4 V vs. RHE

(d) FED at -1.0 V vs. RHE
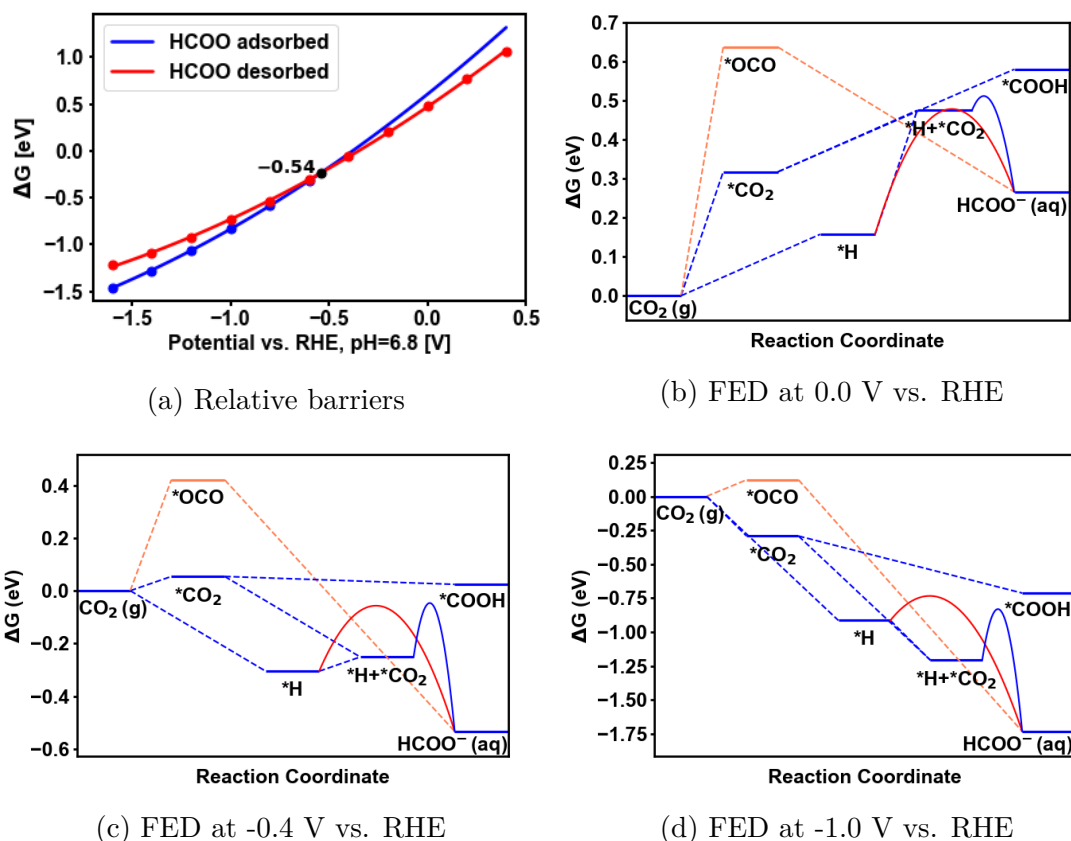
Figure 5.9: Reaction energetics for CO_2 reduction on Cu(211)
(a) shows the competition between the adsorbed and desorbed pathway to $HCOO^-$ through *H. (b-d) show free energy diagrams for the reduction of CO_2. The pathways that go through CO_2 are shown in blue, while the pathway through *OCO is shown in orange and the pathway through *H and desorbed CO_2 is shown in red.

Qualitatively, we observe the same trends with SJM as we did we our simplistic model, namely that neither *CO_2 nor *OCO are stable on the surface without field stabilization, but that they both benefit to some extent from potential and that this effect is significantly larger for *CO_2, making this the preferred binding motif on the metal step. Quantitatively we even predict largely the same field stabilization for *CO_2 with -0.57 eV/V for the model versus -0.63 eV/V with SJM. Our model does not however describe the energetics quantitatively, instead the energies of bent CO_2 are significantly higher in our model than what we calculated with DFT and SJM. This may be due to the artificial constraint of the O-C-O, which does not allow the system to relax freely. Finally, the hypothesis that the binding motif for adsorbed CO_2 controls the selectivity towards formate does appear to be possible in theory, subject to competition between surface hybridization and field stabilization, as both species are stabilized by both contributions. For this particular metal surface however, the energetics do not support the idea that the formate is produced via the *OCO motif.

5.5   Expanding the search for CO₂ motifs

If we revisit the periodic table of CO$_2$R products (Figure 1.3), we find a number of other metals that produce formate. Palladium is treated in a separate chapter of this thesis, but we attempt to probe the binding motif hypothesis for some of the remaining metals, the (100) facet of the BCT structure of Sn, the (211) and (100) facet of Cu, the (211) facet of the FCC structures of In, Pb and Ni. Although Ni almost exclusively produces hydrogen, except for 1.4% of HCOO⁻ around −1 V vs. RHE [102], it is included as a relatively oxophilic metal, to see if its oxophilicity can stabilize *OCO relative to *CO$_2$/*COOH. Additionally, we were not able to stabilize *OCO on the Pb step, so this was ultimately left out. The binding energies of *CO$_2$, *OCO and *COOH are shown in Figure 5.10, as a function of potential, to map out their relative stabilities in different potential regions and probe what the dominant pathway is expected to be at different potentials.

The fits show that the *OCO motif is *always* less stable that *CO$_2$ for the potential region and metals considered. Additionally, the other possible RDS of *CO/CO, the *COOH intermediate, is also more stable at most potentials, although *OCO is more stable on some metals at slightly positive potentials. But since the equilibrium potential of CO$_2$ reduction to HCOO⁻ is around −0.1 V vs. RHE, we do not expect to see formate production in this region. All this indicates, that the *OCO intermediate is not expected to play a major role in HCOO⁻ production and that the exact kinetics of HCOO⁻ production remains elusive. Additionally, making formate through a PCET to CO$_2$ was ruled out due to sterical and electrostatic hindrance while the formation of HCOO⁻ through a surface hydrogenation is difficult to reconcile with the fact that the improvement in HCOO⁻ selectivity over CO is correlated with a weakening of *H binding or the kinetic isotope experiments that indicate that *H is not involved in the kinetics of the RDS. Based on our findings it does however remain the most probable explanation that HCOO⁻ is formed through a surface hydrogenation step starting from either desorbed CO$_2$ or *CO$_2$. To further elucidate the kinetics of formate production, the possible PCET steps could be mapped out in greater detail, competition with HER could be included, while ultimately the barriers of all the electrochemical steps should calculated including solvent dynamics to account for solvent reorganization during the reaction [86].
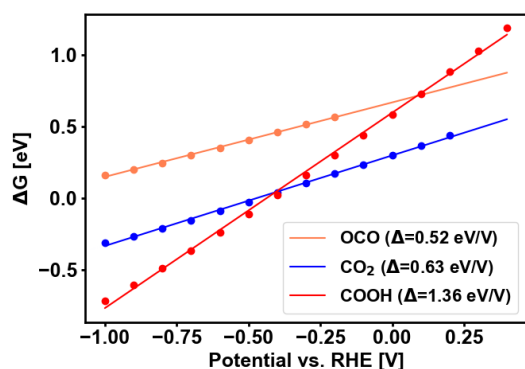
(a) Cu(211)
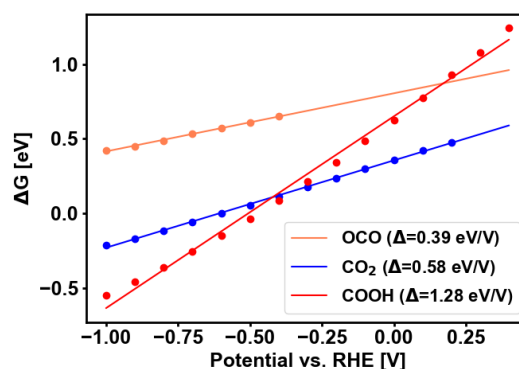
(b) Cu(100)
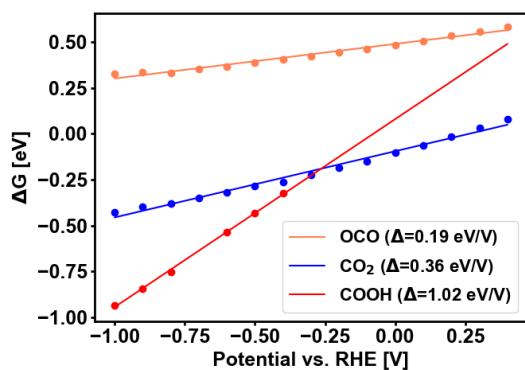
(c) Ni(211)
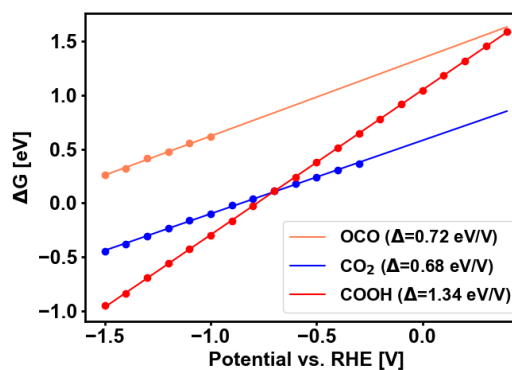
(d) In(211)
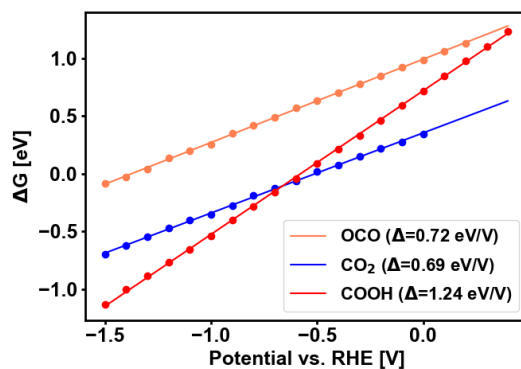
(e) Sn(100)

Figure 5.10: CO_2R adsorbate fits across a range of metals

Energy vs. potential for 3 CO_2R intermediates, $*CO_2$ (blue), $*OCO$ (orange) and $*COOH$ (red) on a range of metals. The slope (Δ) of each adsorption energy is shown in the respectively figure legends. Calculated energies are shown as points, with a line of best (linear) fit. Energies are calculated from $-1.0\,\mathrm{V}$ to $0.4\,\mathrm{V}$ vs. RHE, except for In(211), where lower potentials were required to stabilize $*OCO$.

Electrochemical CO$_2$ Reduction to Two-Electron Products

6 Going for Gold

Will Playing the Field Get Us There?

In this chapter we explore the intrinsic CO_2R activity of gold surfaces. On the basis of carefully synthesized size-controlled nanorods we explore their surface structure as well as intrinsic electrostatic properties, namely the electric surface field, how both of these vary, what effect changing them has on CO_2R activity, and how we can decouple the effects we observe. To achieve this, we compute surface-dependent energetics using DFT with SJM to include potential effects and electric field responses of reaction intermediates. To complement this, we design a continuum model using COMSOL Multiphysics, to explicitly model the fields of the different gold cylinders to observe any trends in field enhancement with nanostructure size. Finally, we link the electric field to activity and compute expected activity enhancements relative to the electric fields. This project has been carried out in collaboration with experimental groups at Nanyang Technological University, Singapore and the experimental data referenced and illustrated was obtained there. The contents of this chapter are from the manuscript *Quantifying and Optimizing Electric Field Enhancement Effect on Carbon Dioxide Electroreduction, (to be submitted)*, enclosed in Section A.2.

6.1 Introduction

The electric field represents a strong potential driving force in electrocatalysis, and, as the previous chapters have outlined, plays a large role in CO_2 reduction in particular, changing both how much and what product is formed. The *CO_2 state is one of the few states with a strong field response [107], but it is at the same time crucial to the CO_2 reduction activity on many metals [108]. Particularly at increasingly negative potentials, where the charge response, through destabilization of the proton/electron couple, stabilize reduced intermediates relative to *CO_2. Although the electric field is a property of the electrochemical environment, which appears "naturally" at the electrochemical interface following changes in potential, it can be tuned and enhanced through e.g. varying the cation size [109]. It has also been proposed by Sargeant et al., that high curvature facets can induce strong local fields that can drive CO_2 reduction on gold [110]. This interpretation was based on the observation of significant activity increases between quite different structures although the effect varies for different metals. Similar trends were shown on Cu by Liu et al. [111]. At the same time, a review of nanostructured coinage metals by Smith et al. found no intrinsic improvement of high curvature nanostructures for Au and Cu when normalized by the ECSA, and even found the activity of Ag to increase with cylindrical radius [112]. These results, and the discrepancy between them, is fundamentally interesting and calls for a well-defined platform to quantify the enhancement effect and decouple it from other effects of e.g. structure and synthesis method across different geometries. In theory, the electric field at a given potential should primarily depend on the physical dimension of the nanoneedle, except for

some degree of atomistic effects as e.g. the Smoluchowki effect which can induce a small local field on steps/defects [113]. However, the synthesized nanoneedles are very heterogeneous in terms of structure and dimensions, and with highly porous geometries we might also have significant mass transport limitation. Thus, it is challenging to quantify electric field contribution on such a system and decouple it from other local or non-local effects which might be present.

Our aim with this study is to do just that; through a physical molding process highly ordered gold cylinders were produced with a diameter down to 30 nm, retaining the same surface structure for all systems and cylinders. In order to probe thinner rods, chemical etching was employed, for set time intervals until well defined, thin nanorods and needles could be produced with a homogeneous size and structure. The structures we obtain are shown in Figure 6.1. From the gold nanorods we carry out CO_2 reduction to CO and normalize the results both by the electrochemical surface area (ECSA) and by an estimate of the physical surface area, from Atomic Force Microscopy (AFM) measurements. To couple the experimentally obtained activities to the electric field, we construct a continuum model of the electrical double layer with the COMSOL simulation software, using a Poisson-Boltzmann approach. Additionally, we compute surface-dependent FED's to find the active facet(s), their rate determining step(s) and their respective field response.
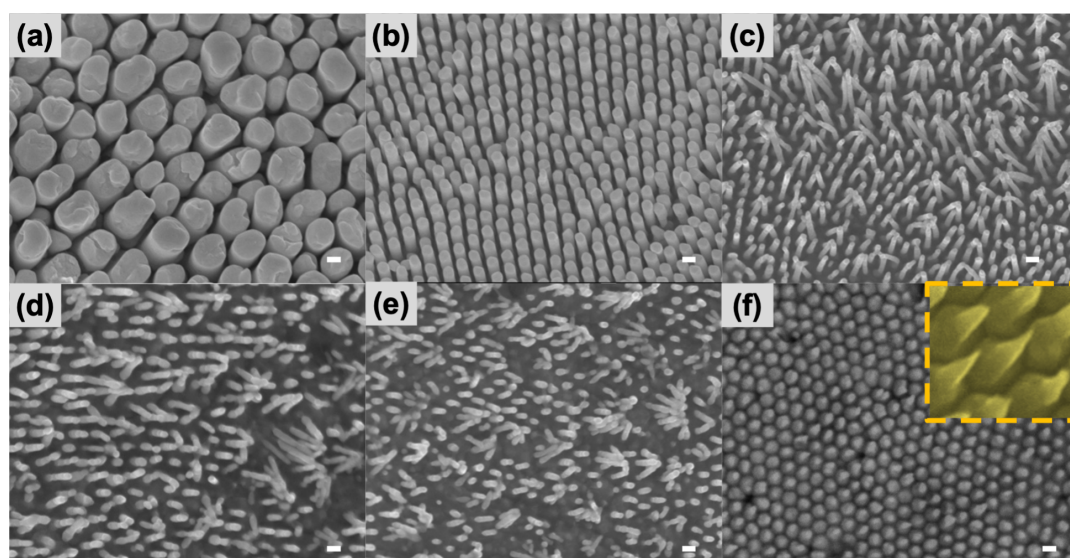
Figure 6.1: Surface morphologies of Au nanostructures

Scanning electron microscopy images of the Au nanostructures. (a)-(e) are nanorods with diameters of 200, 100, 30, 20 and 10 nm, respectively. White scale bars=100 nm (f) are Au nanoneedles, including an insert with an enlarged image of the needles. All are synthesized using the same molding technique, (d)-(f) are 30 nm molds etched for 3, 5 and 7 seconds respectively. *Experimental data, reprinted from manuscript in Section A.2.*

6.2 Modeling the Electric Field

The electric field will be modeled as the gradient $\nabla\phi$ of the electrostatic potential ϕ. The potential is found using Poisson's Equation:

$$\nabla^2\phi = -\frac{\rho}{\epsilon_r\epsilon_0} \tag{6.2.1}$$

Where ∇^2 is the Laplace operator, ρ is the charge density and ϵ_r, ϵ_0 is the relative and vacuum permittivity respectively. For water $\epsilon_r = 78.36$ at $25\,°\mathrm{C}$.

For a z:z charge electrolyte, the charge density ρ is found from Boltzmann statistics as:

$$\rho = z\cdot e\cdot n\cdot\left(\exp\left(-z\cdot e\cdot\beta\cdot\phi\right) - \exp\left(z\cdot e\cdot\beta\cdot\phi\right)\right) \tag{6.2.2}$$

Where z is the unit charge, e is the elemental charge, n is the number density and β is the inverse thermodynamic temperature, $\beta = \dfrac{1}{k_BT}$.

Inserting eq. (6.2.2) into (6.2.1) we find that:

$$\nabla^2\phi = -\frac{z\cdot e\cdot n(\exp\left(-z\cdot e\cdot\beta\cdot\phi\right) - \exp\left(z\cdot e\cdot\beta\cdot\phi\right))}{\epsilon_r\epsilon_0} \tag{6.2.3}$$

$$= \frac{2\cdot z\cdot e\cdot n}{\epsilon_r\epsilon_0}\cdot\sinh\left(z\cdot e\cdot\beta\cdot\phi\right) \tag{6.2.4}$$

For a 1:1 electrolyte we then have:

$$\nabla^2\phi = \frac{\kappa^2}{e\cdot\beta}\cdot\sinh\left(e\cdot\beta\cdot\phi\right) \tag{6.2.5}$$

With κ being the *inverse Debye length*, $\left(\kappa = \sqrt{\dfrac{2\cdot e^2\cdot n\cdot\beta}{\epsilon_r\epsilon_0}}\right)$

In cylindrical coordinates, the Laplacian is given as:

$$\nabla^2\phi = \frac{1}{r}\frac{\partial}{\partial r}\left(r\frac{\partial\phi}{\partial r}\right) + \frac{1}{r^2}\cdot\frac{\partial^2\phi}{\partial\theta^2} + \frac{\partial^2\phi}{\partial z^2} \tag{6.2.6}$$

Inserting eq. (6.2.6) into eq. (6.2.5) and approximation the system as an infinite, uniform cylinder, i.e. $z\to\infty$, $\phi(r,\theta,z)\approx\phi(r)$, we arrive at:

$$\frac{1}{r}\frac{\partial}{\partial r}\left(r\frac{\partial\phi}{\partial r}\right) = \frac{\kappa^2}{e\cdot\beta}\cdot\sinh\left(e\cdot\beta\cdot\phi\right) \tag{6.2.7}$$

With this, we are effectively modeling the field/potential from/on the side of the cylinder. To solve this, we need a set of boundary conditions. The first condition is a simple Dirichlet boundary condition, where we assume to potential is constant in the bulk, as the absolute potential is equal to the potential of the reference electrode, referenced to 0:

$$\lim_{r\to\infty}\phi(r) = \phi^0 = 0 \tag{6.2.8}$$

And, by extension, this also makes the field 0 in the bulk, regardless of the chosen value for ϕ^0. The potential is referenced to the SHE scale and converted to RHE, assuming pH $= 7.2$ throughout the electrolyte. Furthermore, we need to account

for the changes in potential across the entire double layer. The capacitance across the entire double layer c_{dl} from metal to bulk is given as:

$$c_{dl} = \frac{\mathrm{d}\sigma}{(\mathrm{d}\phi^m - \phi^0)} \tag{6.2.9}$$

Where ϕ^m is the metal (electrode) potential and σ is the surface charge density We treat this double-layer through a Stern model and split the total capacitance separating the electrode from the bulk into two components in series: (i) The Helmholtz/Stern layer c_H which accounts for the (counter) ion buildup near the surface in the reaction plane and (ii) a Gouy-Chapman (*diffuse*) layer c_{GC}, where ions diffuse free relative to the electrostatics of the system. c_H and c_{GC} are defined as:

$$c_H = \frac{\mathrm{d}\sigma}{(\mathrm{d}\phi^M - \phi^{\ddagger})} \tag{6.2.10}$$

$$c_{CG} = \frac{\mathrm{d}\sigma}{(\mathrm{d}\phi^{\ddagger} - \phi^0)} \tag{6.2.11}$$

Or, relating to c_{dl}:

$$\frac{1}{c_{dl}} = \frac{1}{c_H} + \frac{1}{c_{GC}} \tag{6.2.12}$$

We insert c_{dl} from eq. (6.2.9) and c_{GC} from eq. (6.2.11) and get an expression for $\mathrm{d}\sigma$ as a function of c_H, ϕ_m, $\phi^{\ddagger}$ and ϕ_0:

$$\frac{1}{\frac{\mathrm{d}\sigma}{(\mathrm{d}\phi^m - \phi^0)}} = \frac{1}{c_H} + \frac{1}{\frac{\mathrm{d}\sigma}{(\mathrm{d}\phi^{\ddagger} - \phi^0)}} \tag{6.2.13}$$

$$\frac{\mathrm{d}(\phi^m - \phi^0)}{\mathrm{d}\sigma} = \frac{1}{c_H} + \frac{\mathrm{d}(\phi^{\ddagger} - \phi^0)}{\mathrm{d}\sigma} \tag{6.2.14}$$

$$c_H \frac{\mathrm{d}(\phi^m - \phi^0)}{\mathrm{d}\sigma} = 1 + c_H \frac{\mathrm{d}(\phi^{\ddagger} - \phi^0)}{\mathrm{d}\sigma} \tag{6.2.15}$$

$$c_H \, \mathrm{d}(\phi^m - \phi^0) = \mathrm{d}\sigma + c_H \, \mathrm{d}(\phi^{\ddagger} - \phi^0) \tag{6.2.16}$$

$$\mathrm{d}\sigma = c_H \left(\mathrm{d}(\phi^m - \phi^0) - \mathrm{d}(\phi^{\ddagger} - \phi^0)\right) \tag{6.2.17}$$

Using Gauss' law:

$$\sigma(r) = \lim_{r \to R} \epsilon \frac{\mathrm{d}\phi(r)}{\mathrm{d}r} \tag{6.2.18}$$

and assuming constant Helmholtz capacitance c_H (in this study we assume $c_H = 20 \ \mu\mathrm{F} \ \mathrm{cm}^{-2}$) in eq. (6.2.17), we can solve for $\sigma(r)$ and a Robin boundary condition emerges on the surface of the cylinder [114]:

$$\lim_{r \to R} \epsilon \frac{\mathrm{d}\phi(r)}{\mathrm{d}r} = c_H \left((\phi^m - \phi^{PZC}) - (\phi^R - \phi^0)\right) \tag{6.2.19}$$

With this, we can iteratively solve for the potential as a function of radial distance to find numerical solutions for a given cylinder radius. Below are a summary of the assumptions of this model:

z $\to \infty$ infinite length, i.e. no z-component

$\phi^{\mathbf{PZC}} = \mathbf{0.4}$ **V vs. SHE** PZC of gold

$\mathbf{c_H =20\ \mu F/cm^2}$ Experimental capacitance of water [85].

$\phi^{\mathbf{0}} = \mathbf{0}$ Bulk ϕ is reached, i.e. rods are adequately separated, no overlapping fields

- No diffusion/mass transport limitations

6.3 CO$_2$ Reduction Activity of Gold Nanorods

The CO$_2$R activity as well as selectivity towards CO was recorded for each of the nanorod systems. Figure 6.2 gives an overview over the experimental data, and as panel (a) and (c) shows, both the selectivity and activity towards CO increases as we go more cathodic in potential. The kinetics also changes significantly across the surfaces. The Tafel slopes of the cylinders are significantly lower than that of Au foil (120 mV/dec). In contrast, the current densities and Tafel slopes remain similar for the cylinders with diameters from 200 to 30 nm. Such small variations of current density and Tafel slope would suggest that the these samples have similar activity and kinetics, originated from similar types of active sites and rate determining steps (RDS). Notably, another current density leap is seen from as-imprinted (200 to 30 nm) samples to the etched samples. The current density remains similar for etched samples despite their very different diameters of 20, 10 and sub-10 nm. Moreover, the Tafel slope at low current density generally decreases with nanorod diameter combined with a reduction in onset potential (-0.4 V to -0.2 V) across the samples. As the overpotential increase a change in Tafel slope appears for every system but the foil, particularly clear for the samples with an onset potential around -0.2V. It has been suggested, that different kinetic regions exist for CO$_2$ reduction on gold, with CO production initially being limited by a PCET step (to form *COOH) at very low overpotentials, followed by a region limited by CO$_2$ adsorption at intermediate potentials, until we ultimately reach a region limited by mass transport limitations [83], [115]. The Tafel slopes and changes in slope for the low overpotential data present in this study would be consistent with this hypothesis.

In addition to the change of activity/selectivity as a function of potential, we also show how the CO$_2$ reduction varies with surface structure at a specific potential (-0.6 V vs. RHE), normalized using two different methods to determine the (relative) surface area; ECSA, the usual standard used to normalize activity, and AFM tip-probing, which we coin the "physical" surface area. The top right panel (b) shows the ECSA normalized data, (d) shows the normalized data from the AFM method, both at $-0.6\,\mathrm{V}$ vs. RHE. It has been suggested that the ECSA obtained from double layer capacitance measurements can be affected by variations in the electric field, which might convolute possible field enhanced activities [116]. As a complimentary way to access and measure the surface area, we use an AFM tip to scan across our cylinders. The cylinders we use for the CO$_2$ reduction are too tall to be used in this method, so we have measured shorter cylinders and extrapolated to the real height. This approach of fitting the roughness, R_p for the nanorod structures naturally comes with some uncertainty, but it serves as a viable benchmark for the ECSA roughness estimates, R_e. If we assume that both approaches represent the true active surface area, the ratio of R_e and R_p approaches one. If we on the other hand follow the assumption that R_e might be overestimated due to changes in the field,
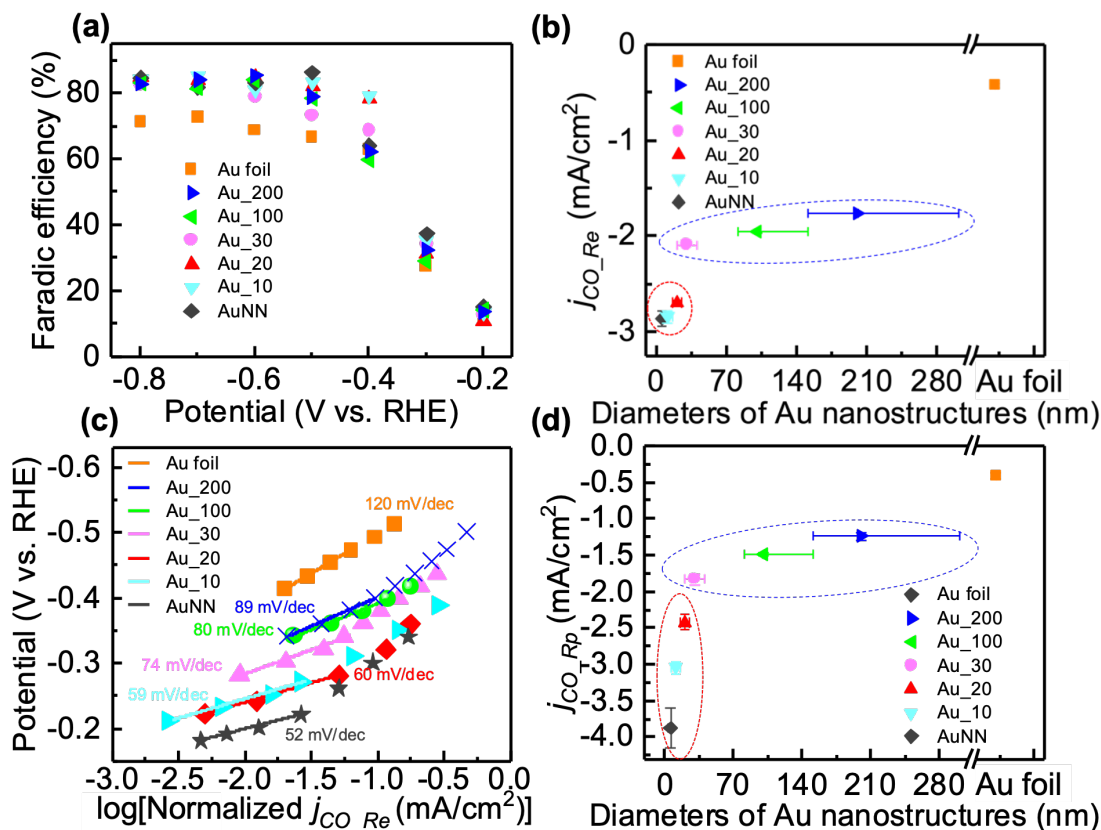
Figure 6.2: CO_2 Reduction Performance of Nanorods

(a) Faradaic efficiency of Au samples. (c) Log of current normalized to electrochemical roughness factor vs. potential for Tafel slopes. (b), (d) CO partial current density at -0.6 V vs. RHE normalized to electrochemical roughness factor and physical roughness factor, respectively. Each current density value in (b), (c), (d) was obtained by averaging the data from 3 different tests. The red and blue dashed circles in (b), (d) indicate etched and unetched samples. *Experimental data, reprinted from manuscript in Section A.2.*

this ratio should start at 1 and increase with the field enhancement. Surprisingly, we find that R_e/R_p is consistently below 1 except for the 10 nm wide nanorod and etched nanoneedles, meaning that we either underestimate Re or overestimate R_p at intermediate nanorod radii. The ratio reaches about 1.3 for the sub-10 nm sample. Nevertheless, as the two estimates are generally close (ratio going from around 0.7 to 1.3), they give us a probable range for the "true" surface area. Overall, we observe a 64.7% increase in ECSA normalized activity from the 200 to sub-10 nm structures. And for both R_e and R_p, the trend of activity with cylinder size indicates that two different activity regions exist for the cylinders; a region for the ≥ 30 nm, the one encircled in blue on Figure 6.2 (b) and (d), and a region for the sub-30-nm samples, encircled in red, that are somehow different from each other. The two regions coincide with the change in synthesis method from "just" assembling the nanorods with the physical molding, to molded structures with subsequent etching.

6.3.1 Nanorod Surface Structure

To understand what causes the jump in activity from the unetched to the etched structures, we examine nanorods from both etched an unetched samples using Transmission Electron Microscopy (TEM). The TEM images are shown in Figure 6.3 and we find that while the 100 nm rod (c,f) retains a very smooth, clean (111) facet surface throughout, both the nanoneedle (a,d) and the 20 nm rod (b,e) appear to have several defects in the form of both steps and peaks, and the zoomed-in images (d-f) show that the etched samples have a much high site density of steps surface compared to the unetched sample. The implications of the introduction of steps on the surface is evaluated in the section below.
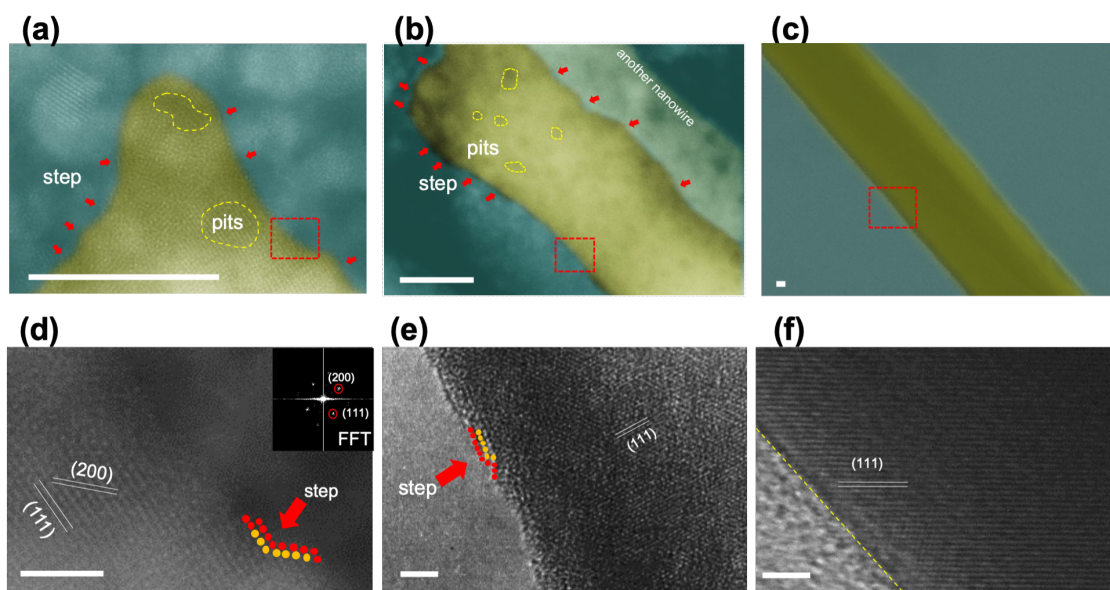
Figure 6.3: Nanorod characterization with TEM

(a-b) Show images of nanoneedle and etched 20 nm rod using ADF-STEM, with red arrows and yellow outlines that show steps and pits on the surface. (c) TEM image of 100 nm rod. (d-f) High-resolution TEM images of the region indicated with red outline in (a-c) for the nanoneedle, 20 nm rod and 100 nm rod surfaces respectively. Fast Fourier Transform (FFT) of needle shown as insert in (d) along with identification of (200) and (111) facet Scale bars, 10nm (a-c) and 2nm (d-f). *Experimental data, reprinted from manuscript in Section A.2.*

6.4 Decoupling Field and Surface Structure Effects

To determine the origin of the activity enhancements we observe, we identify two possible contributions to the activity; intrinsic enhancements of the electric field due to increasing nanorod curvature and structure-dependent activity enhancements due to increases in the site density of high-activity sites from surface morphology changes introduced by the etching process.

The model for the electric field derived in Section 6.2 is fed into the COMSOL Multiphysics software, build up from the bottom from the *Poisson's Equation interface*. This is simple to change into cylindrical coordinates by multiplying both

the diffusion coefficient and source term by a factor r. The density from Boltzmann statistics is used as the source term and the two boundary conditions are plugged in at the surface, $r = R$ and the bulk respectively. The raw output of the model is a potential profile as a function of distance from the metal surface. We take the gradient of this in Python and get a profile of the change in the electric field with surface distance.

We only need the field at the surface, $\left.\dfrac{\mathrm{d}\phi}{\mathrm{d}r}\right|_{r=R}$, i.e. essentially the first point of that field profile. Given a specific field, we need to know, how that field translates into reaction energetics and activity. The field dependence of the formation energy of CO_2R reaction intermediates has been quantified by fitting a parabola to a range of ΔE's at varying surface charge density, σ [115]. Of all the intermediates and facets probed, $*CO_2$ on a stepped (211) surface proved have the largest field response. We use this, to get a best-case value for the activity enhancement:

$$\Delta E_\sigma = \Delta E_{\sigma=0} + \Delta a_\sigma \cdot \sigma + \Delta b_\sigma \cdot \sigma^2 \tag{6.4.1}$$

$$\Delta E_\sigma = 0.74\,\mathrm{eV} + 2.98 \times 10^{-2}\frac{\mathrm{cm}^2}{\mu\mathrm{C}\cdot\mathrm{eV}}\cdot\sigma - 2.87 \times 10^{-4}\left(\frac{\mathrm{cm}^2}{\mu\mathrm{C}\cdot\mathrm{eV}}\right)^2\cdot\sigma^2 \tag{6.4.2}$$

We can directly relate the field to the surface charge density through Gauss' Law above in eq. (6.2.18). Next, we can extract activities from the reaction energetics by assuming an Arrhenius Relationship between the rate constant k and the activation energy E_A:

$$k = A\mathrm{e}^{\frac{-E_A}{k_B T}} \tag{6.4.3}$$

Where A is the pre-exponential factor. As we are looking for *enhancements* in the the activity relative to some reference, we can relate the rate constant of a cylinder with radius i to the rate constant of the foil ("∞ radius cylinder"):

$$k_{rel,i} = \frac{k_i}{k_\infty} = \frac{A_i\mathrm{e}^{\frac{-E_{A,i}}{k_B T}}}{A_\infty\mathrm{e}^{\frac{-E_{A,\infty}}{k_B T}}} \approx \mathrm{e}^{\frac{E_{A,\infty} - E_{A,i}}{k_B T}} \tag{6.4.4}$$

Next, we assume that the pre-factors are similar, i.e., $A_i \approx A_\infty$, which includes the assumption that the adsorbates are similar in structure and as a result has largely the same change in entropy. If we additionally assume that the $*CO_2$ adsorption barrier is low, such that $E_A \approx \Delta E$, we can relate the relative rate to ΔE_σ through eq. (6.4.2) and by extension to the electric field through σ:

$$k_{rel,i} \approx \mathrm{e}^{\frac{\Delta E_{\sigma(\infty)} - \Delta E_{\sigma(i)}}{k_B T}} \tag{6.4.5}$$

With this, we can calculate how the electric field of a nanorod of a given radius translate into an improvement in activity. This is shown for a number of different diameters in Figure 6.4, where the fields are shown as field enhancements relative to a flat surface[1], which has an electric field of 0.3975 V/nm at -0.6 V vs RHE. Note,

---

[1]modeled as a 2000 nm cylinder for consistency, values converge a lot earlier, 300-400 nm.

that this absolute value of the field is roughly 3 orders of magnitude above the enhancements observed, but still well in line with the field strengths we can expect at cathodic potentials [108].

We find that a significant field induced activity enhancement ($> 10\%$) can only be observed for diameters below $2\,\text{nm}$ to $4\,\text{nm}$, with a 4 nm rod having 10% higher activity than a flat surface and a 2 nm rod having 21% higher activity than a surface without curvature. Finally, for illustrative purposes, we have included a 0.2 nm "rod", which has an activity enhancement of roughly 450% relative to the flat surface. By this point, we are no longer in a regime that we can treat reliably, nor is it a physically relevant system, instead this corresponds to a single-atom string of gold atoms since the Au-Au distance of bulk Au is around 0.3 nm (we found it to be 0.3004 nm with DFT). It is included however, to show just how extreme cases we have to go to, in order to get large field induced enhancements of the activity. Being a continuum model, we have not taken any atomistic field enhancement into consideration. Theoretically, the introduction of atomistically sharp features could induce a local field through smoothening out of the electron density near these features, the so-called Smoluchowki effect [113], but the effect of this has not been quantified in this field model.
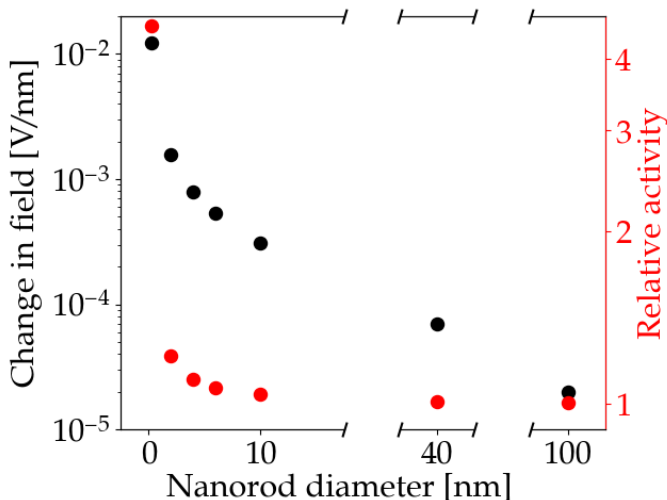
Figure 6.4: Model for the electric field and its activity improvements

This figure shows the results of the field model derived and used for this study. The change in electric field (black) and predicted activity relative to a flat surface (red) for various nanorod diameters.

Next, to understand what role the surface morphology changes play, we obtain more insight on the activity, active sites as well as rate determining step(s) through DFT calculations using the SJM module to obtain constant potential energetics. As CO was the major product for most of the potential range across all samples studied, we focus on the pathway towards CO, and compare the energetics across several different gold facets. Specifically, we study the two facets identified with FFT of the TEM images from Figure 6.3(d), (111) and (100), along with the (211) facet as a

model for steps/defects. We find that the stepped (211) facet significantly stabilize the $*CO_2$ and $*COOH$ intermediate relative to the two other facets as seen in Figure 6.5(a). This finding is in line with results from lead deposition experiments, showing that even on highly ordered surfaces the CO_2R activity on Au facets comes from a small number of kink/step defects [117]. Similarly, studies of CO_2R on different bulk grains and grain boundaries on gold, found bulk defects at the boundaries, e.g. between (111) and (100) grains, to enhance CO_2 reduction [118].
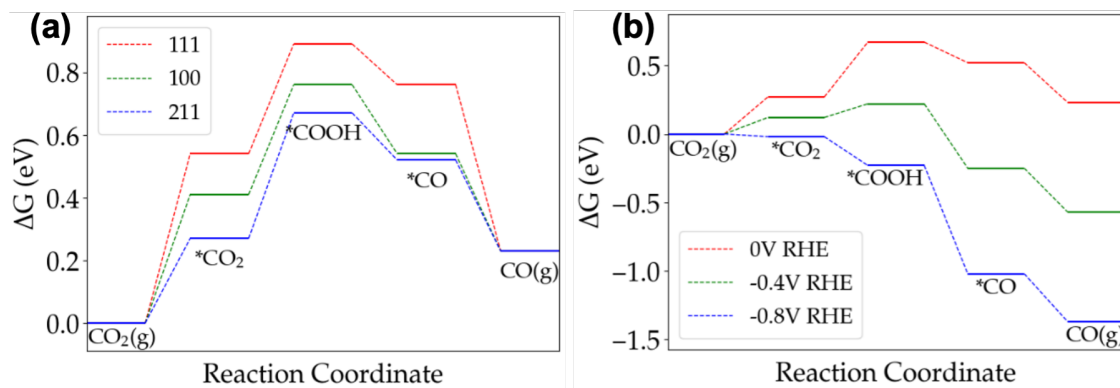
Figure 6.5: Free energy diagrams for CO_2 to CO on various gold facets and potentials (a) Comparison of formation free energies of CO_2R reaction intermediates on the 111 (red), 100 (green) and 211 (blue) facets at 0 V vs. RHE. (b) Comparison of formation free energies of CO_2R reaction intermediates on Au(211) at varying potential, 0 V (red), -0.4 V (green) and -0.8 V (blue) vs. RHE.

We then proceed to calculate field and charge responses of each of the intermediates and produce potential dependent reaction pathways for Au(211), as shown in Figure 6.5(b). Based on this, $*COOH$ is expected to be the RDS for CO production on gold at low reducing potentials, until a change in the RDS happens around -0.4 V vs. RHE and $*CO_2$ adsorption becomes rate limiting. Although $*CO_2$ has the lowest potential response, with 0.36 eV/V versus 1.12 and 1.93 eV/V for $*COOH$ and $*CO$ respectively, the majority of the potential response of the latter two is due to destabilization of the proton-electron pair with potential (the "charge response"). If we compare just the field response, from the surface dipole interacting with the electric field, this amounts to 0.36, 0.12 and -0.07 eV/V for the three intermediates. Consequently, if we were able to successfully improve the field across the nanorods, the effect on activity should be much smaller at low overpotentials where $*COOH$ is rate limiting, than at more negative potential where $*CO_2$ is the RDS. Going back to the Tafel plot in Figure 6.2(c), this does not seem to be the regardless of whether we estimate the potential of RDS change from the FED's or the Tafel slopes. If anything, the shifts seem slightly larger at low overpotentials.

Finally, we show the ECSA normalized current densities obtained from the different 30 nm nanorods along with select results from literature representing a mix of nanostructured surfaces and "ordinary" foil data in Figure 6.6. From this, it is clear that normalized to ECSA, the partial current densities are remarkably similar, not only within our own data set but also in comparison to other studies. Even for sys-
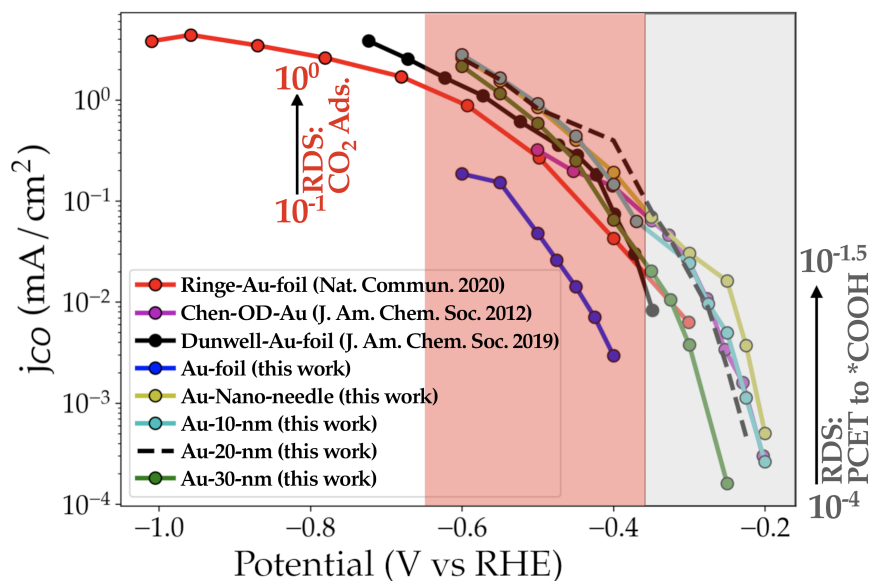
Figure 6.6: Experimental ECSA partial current densities to CO on gold

Comparison of experimental ECSA currents for CO_2 to CO on gold from this work and previous results from Ringe et al. (red) [115], Chen et al. (purple) [119] and Dunwell et al. (black) [120]. The grey shaded region indicates the region limited by *COOH formation, the red shaded indicates the region where *CO_2 is the RDS and the white region the mass transport limited region.

tems that employ synthesis methods that are distinctively different from our highly ordered nanorods, such as the highly disordered oxygen-derived structures (Cheng et. al), it all seems to fall almost on the same line. The only outlier is our foil data, although we are not quite sure why it falls below the trend. One thing we do observe, is that through the nanorods we are able to probe the low-overpotential regime of CO production (roughly $-0.2\,\mathrm{V}$ to $-0.4\,\mathrm{V}$ vs. RHE), a region with little data from the other studies, and with this, support the hypothesis from theoretical studies, that we indeed have a narrow low-overpotential region where the CO production is limited by *COOH formation rather than *CO_2 adsorption.

6.5 Conclusion

In an effort to probe the existence of activity improvements from curvature-induced field enhancements and quantify this, we synthesize a number of different gold nanostructures. Specifically, we were able to successfully produce highly ordered, crystalline gold nanorods ranging from $30\,\mathrm{nm}$ to $200\,\mathrm{nm}$, and these were all selective for *CO_2 reduction, with slight improvements of activity with decreasing radius. To further increase the curvature, we perform Au etching to a number of 30 nm systems, sharpening the rods to a varying degree by the etching from 3 to 7 seconds. While this increases the curvature, it also changes the surface morphology from highly crystalline, to a rougher surface with a significantly higher density of defect sites such as pits and steps/kinks. Notable activity improvements (on a linear scale) is observed, but it is difficult to deconvolute the field effects from the site density effects based on the experimental data alone. To achieve this, we set up a contin-

uum model for the electric field on the metal surface as a function of cylinder radius and find that the expected field enhancement is negligible for the range of nanorod diameters tested in our setup. In contrast, we find that the predicted activity on surface defects, obtained from *ab-initio* models and modeled as a step between the 100 and 111 surface (the 211 facet), is orders of magnitude higher than the activity on both the 100 and 111 facet. Thus, by increasing the density of steps/kinks, we increase the density of high-activity sites and it is this change in the site density that drives the activity enhancements we observe across the nanorods, while the electric field enhancements are very limited within the considered size ranges. With this work, we elucidate the role of the surface electric field in CO_2 reduction, a crucial parameter not only in CO_2 reduction on gold, but also on catalysts beyond Au and reactions beyond CO_2 reduction.

7 Summary and Outlook

As we transition towards a future based on renewables, electrochemical CO_2 reduction presents itself as an important tool in the green toolbelt. Not only does it have the ability to produce CO_2 neutral fuels, we can potentially do it using green, excess energy from intermittent energy sources. There is still significant work ahead both from a fundamental standpoint, in understanding and describing the factors the drive or limit the formation of various product and also further down the road with scalability and stability. The production of the desirable products require high overpotentials and have poor selectivity. In this thesis we present a number of studies on the factors that guide selectivity in CO_2 reduction to two-electron products, as well as a probe into intrinsic design improvements of the electrode.

Through our overview of the components of the electrochemical environment and the factors that drive reactions, we find the electric field (and potential) to be crucial for the activity. Something that is especially true in CO_2 reduction, as this is often limited by CO_2 adsorption, and *CO_2 has a significant field stabilization compared to other reaction intermediates. We study the CO_2 reduction to formate and CO on palladium, as palladium is able to selectively produce both products depending on the applied potential. We predict that the pure palladium metal will not produce any carbon products electrochemically. At the same time however, we find that the palladium undergoes significant morphology changes in the presence of the electrochemical environment and forms a highly hydrogen-rich palladium hydride structure, which completely changes the CO_2R energetics. It has been proposed that the selectivity between formate and CO is determined by the binding motif of CO_2, binding either via the oxygens (*OCO) for formate or through the carbons (*CO_2) for CO. On the hydride structure, we do not find this to be the case, and do not even find the *OCO state to be stable in our simulations. Instead, we identify two competing steps as the rate determining steps towards either CO or formate. Additionally, from constant-potential computations we find that these have markedly different stabilization with potential and that this is what drives the rapid shift in selectivity. To some extent, this reaction is almost a text-book example of the power of potential and the electrochemical environment. Not only do we drastically alter the electrode material itself, which changes the energy landscape to accommodate CO_2R, we also see the effect potential has on the driving force of electrochemical reactions, through the competition with a step where this effect is largely absent.

In Chapter 5 we were able to construct a model used to describe the contributions to the surface stability of CO_2 binding motifs from hybridization (the "chemical" contribution) and from dipole-field interactions (the "electrochemical" contribution). We find that there is essentially a competition between the two, where the hybridization appears to favor the *OCO motif, while the dipole-field interactions favor the *CO_2 motif. Overall, *CO_2 is more stable (on the Cu(211) surface used), in agreement

with subsequent SJM calculations and instead we suggest that formate is formed through a hydrogenation step similar the mechanism on PdH. It should be noted however, that at relevant bond angles, even *OCO has a field stabilization with potential. This is in contrast to what we would expect from a purely molecular picture, where we would expect *OCO to have a positive dipole on the carbon, thus being destabilized at cathodic potentials. But the hybridization comes with charge transfer to CO_2, which eventually makes the total surface dipole negative. Theoretically, it could then be possible for us to find a material where the hybridization is strong enough to make up for the difference in dipole. This was probed on a number of oxophilic materials, many of which produce formate, but none of the *OCO structures were more stable below the equilibrium potential of formate, which is the earliest point we would expect to see formate production.

For the final study in Chapter 6 we probe whether we can intrinsically enhance the electric field on the electrode surface by increasing the surface curvature. For this purpose we worked with an experimental group who designed highly ordered nanostructures and tested their CO_2R activity, observing some improvement of activity with decreasing radius. We model the field using a continuum (PBE) model and find no significant field enhancement within the relevant size range. Once we characterize the different surfaces through TEM we find that the synthesis method of the thinnest nanorods introduce steps and other defects on the surface. To examine whether the improved activity is a result of this process, we model the activity of the flat and stepped surface, and find that the activity of the steps is roughly 2 orders of magnitude higher than the flat surfaces. Based on this we attribute the improved activity to increases in site density of step sites. Finally, the experimental data also verifies the theoretical hypothesis, that a region limited by *COOH formation exists at low overpotentials, with a different potential response to that of CO_2 adsorption.

In summary, this thesis shows the major significance of the electric potential and field, especially for CO_2 reduction. Additionally, the hydride and the nanorod study underlines just how important knowledge of the local environment structure at reaction condition is, and we were able to quantify the CO_2R pathways on Pd down to a near-quantitative agreement with the selectivity switch down to roughly $100\,\mathrm{meV}$. The exact nature of the RDS towards formate remains elusive for the post transition metals, especially as the formate selectivity correlates with poor hydrogen binding, something that would make the hydrogenation pathway unlikely and warrants further attention. One approach could be to search for a material that is oxophilic enough to overcome the smaller field enhancement. Alternatively, it could be interesting to look at some sort of size constraint on an oxophilic metal to accommodate the bidentate binding motif better. Generally, the lattice spacing of the post transition metals is higher than on the transition metals and that may be part of the reason why we do not see the relative enhancement of *OCO we would expect. Finally, the search for intrinsic field enhancement should naturally continue. It has shown to be a viable path e.g. through cation size. One possibility could be trying to quantify and perhaps enhance the Smoluchowki effect we expect to find on steps.

Bibliography

[1] G. H. Brundtland, "Our Common Future", World Commission on Environment and Development, Geneva, Tech. Rep., 1987.

[2] M. Crippa, D. Guizzardi, M. Banja, E. Solazzo, M. Muntean, E. Schaaf, F. Pagani, F. Monforti-Ferrario, J. Olivier, R. Quadrelli, A. Risquez Martin, P. Taghavi-Moharamli, G. Grassi, S. Rossi, D. Jacome Felix Oom, A. Branco, J. San-Miguel-Ayanz, and E. Vignati, "CO2 emissions of all world countries", European Commission Joint Research Centre, Publications Office of the European Union, Luxembourg, Tech. Rep., 2022. DOI: 10.2760/730164.

[3] IPCC, *Climate Change 2021: The Physical Science Basis. Contribution of Working Group I to the Sixth Assessment Report of the Intergovernmental Panel on Climate Change.* Cambridge University Press, 2021, 260 pages.

[4] C. P. Morice, J. J. Kennedy, N. A. Rayner, J. P. Winn, E. Hogan, R. E. Killick, R. J. H. Dunn, T. J. Osborn, P. D. Jones, and I. R. Simpson, "An Updated Assessment of Near-Surface Temperature Change From 1850: The HadCRUT5 Data Set", *Journal of Geophysical Research: Atmospheres*, vol. 126, no. 3, Feb. 2021. DOI: 10.1029/2019JD032361.

[5] D. M. Etheridge, L. P. Steele, R. L. Langenfelds, R. J. Francey, J.-M. Barnola, and V. I. Morgan, "Natural and anthropogenic changes in atmospheric CO2 over the last 1000 years from air in Antarctic ice and firn", *Journal of Geophysical Research: Atmospheres*, vol. 101, no. D2, pp. 4115–4128, Feb. 1996. DOI: 10.1029/95JD03410.

[6] P. Tans and R. Keeling, *NOAA Earth System Research Laboratories Global Monitoring Laboratory.* [Online]. Available: https://gml.noaa.gov/webdata/ccgg/trends/co2/co2_annmean_mlo.csv.

[7] The International Energy Agency, "World Energy Outlook 2022", IEA, Paris, Tech. Rep., 2022.

[8] H. Ritchie, M. Roser, and P. Rosado, *CO and Greenhouse Gas Emissions*, 2020.

[9] IPCC, *Climate Change 2022: Mitigation of Climate Change. Working Group III Contribution to the Sixth Assessment Report of the Intergovernmental Panel on Climate Change.* Cambridge University Press, 2022.

[10] W. Good, "The enthalpies of combustion and formation of n-octane and 2,2,3,3-tetramethylbutane", *The Journal of Chemical Thermodynamics*, vol. 4, no. 5, pp. 709–714, Sep. 1972. DOI: 10.1016/0021-9614(72)90043-2.

[11] K. M. Abraham, "How Comparable Are Sodium-Ion Batteries to Lithium-Ion Counterparts?", *ACS Energy Letters*, vol. 5, no. 11, pp. 3544–3547, Nov. 2020. DOI: 10.1021/acsenergylett.0c02181.

[12] J. Eppinger and K.-W. Huang, "Formic Acid as a Hydrogen Energy Carrier", *ACS Energy Letters*, vol. 2, no. 1, pp. 188–195, Jan. 2017. DOI: 10.1021/acsenergylett.6b00574.

[13] *Heat Values of Various Fuels.* [Online]. Available: https://world-nuclear.org/information-library/facts-and-figures/heat-values-of-various-fuels.aspx.

[14] Z. W. Seh, J. Kibsgaard, C. F. Dickens, I. Chorkendorff, J. K. Nørskov, and T. F. Jaramillo, "Combining theory and experiment in electrocatalysis: Insights into materials design", *Science*, vol. 355, no. 6321, eaad4998, Jan. 2017. DOI: 10.1126/science.aad4998.

[15] Y. Hori, I. Takahashi, O. Koga, and N. Hoshi, "Selective Formation of C2 Compounds from Electrochemical Reduction of CO 2 at a Series of Copper Single Crystal Electrodes", *The Journal of Physical Chemistry B*, vol. 106, no. 1, pp. 15–17, Jan. 2002. DOI: 10.1021/jp013478d.

[16] S. Li, Y. Zhou, K. Li, M. Saccoccio, R. Sažinas, S. Z. Andersen, J. B. Pedersen, X. Fu, V. Shadravan, D. Chakraborty, J. Kibsgaard, P. C. Vesborg, J. K. Nørskov, and I. Chorkendorff, "Electrosynthesis of ammonia with high selectivity and high rates via engineering of the solid-electrolyte interphase", *Joule*, vol. 6, no. 9, pp. 2083–2101, Sep. 2022. DOI: 10.1016/j.joule.2022.07.009.

[17] C. J. M. van der Ham, M. T. M. Koper, and D. G. H. Hetterscheid, "Challenges in reduction of dinitrogen by proton and electron transfer", *Chem. Soc. Rev.*, vol. 43, no. 15, pp. 5183–5191, 2014. DOI: 10.1039/C4CS00085D.

[18] Y. Hori, H. Wakebe, T. Tsukamoto, and O. Koga, "Electrocatalytic process of CO selectivity in electrochemical reduction of CO2 at metal electrodes in aqueous media", *Electrochimica Acta*, vol. 39, no. 11-12, pp. 1833–1839, Aug. 1994. DOI: 10.1016/0013-4686(94)85172-7.

[19] S. Nitopi, E. Bertheussen, S. B. Scott, X. Liu, A. K. Engstfeld, S. Horch, B. Seger, I. E. L. Stephens, K. Chan, C. Hahn, J. K. Nørskov, T. F. Jaramillo, and I. Chorkendorff, "Progress and Perspectives of Electrochemical CO2 Reduction on Copper in Aqueous Electrolyte", *Chemical Reviews*, vol. 119, no. 12, pp. 7610–7672, Jun. 2019. DOI: 10.1021/acs.chemrev.8b00705.

[20] M. T. Tang, H. Peng, P. S. Lamoureux, M. Bajdich, and F. Abild-Pedersen, "From electricity to fuels: Descriptors for C1 selectivity in electrochemical CO2 reduction", *Applied Catalysis B: Environmental*, vol. 279, p. 119 384, Dec. 2020. DOI: 10.1016/j.apcatb.2020.119384.

[21] W. Koch and M. C. Holthausen, *A Chemist's Guide to Density Functional Theory*, 2nd. Wiley, Jul. 2001, 293 pages.

[22] M. Born and R. Oppenheimer, "Zur Quantentheorie der Molekeln", *Annalen der Physik*, vol. 389, no. 20, pp. 457–484, 1927. DOI: 10.1002/andp.19273892002.

[23] P. Atkins and J. de Paula, *Atkins' Physical chemistry*, 9th. Oxford University Press, 2014, 972 pages.

[24] P. Hohenberg and W. Kohn, "Inhomogeneous Electron Gas", *Phys. Rev.*, vol. 136, no. 3B, B864–B871, Nov. 1964. DOI: 10.1103/PhysRev.136.B864.

[25] Á. Nagy, "Density functional. Theory and application to atoms and molecules", *Physics Reports*, vol. 298, no. 1, pp. 1–79, 1998. DOI: 10.1016/S0370-1573(97)00083-5.

[26] W. Kohn and L. J. Sham, "Self-Consistent Equations Including Exchange and Correlation Effects", *Phys. Rev.*, vol. 140, no. 4A, A1133–A1138, Nov. 1965. DOI: 10.1103/PhysRev.140.A1133.

[27] J. P. Perdew, "Jacob's ladder of density functional approximations for the exchange-correlation energy", *AIP Conference Proceedings*, vol. 577, no. August 2001, pp. 1–20, 2001. DOI: 10.1063/1.1390175.

[28] J. P. Perdew, K. Burke, and M. Ernzerhof, "Generalized Gradient Approximation Made Simple", *Physical Review Letters*, vol. 77, no. 18, pp. 3865–3868, Oct. 1996. DOI: 10.1103/PhysRevLett.77.3865.

[29] Y. Zhang and W. Yang, "Comment on "Generalized Gradient Approximation Made Simple"", *Physical Review Letters*, vol. 80, no. 4, pp. 890–890, Jan. 1998. DOI: 10.1103/PhysRevLett.80.890.

[30] B. Hammer, L. B. Hansen, and J. K. Nørskov, "Improved adsorption energetics within density-functional theory using revised Perdew-Burke-Ernzerhof functionals", *Physical Review B*, vol. 59, no. 11, pp. 7413–7421, Mar. 1999. DOI: 10.1103/PhysRevB.59.7413.

[31] N. Mardirossian and M. Head-Gordon, "How Accurate Are the Minnesota Density Functionals for Noncovalent Interactions, Isomerization Energies, Thermochemistry, and Barrier Heights Involving Molecules Composed of Main-Group Elements?", *Journal of Chemical Theory and Computation*, vol. 12, no. 9, pp. 4303–4325, 2016. DOI: 10.1021/acs.jctc.6b00637.

[32] J. Wellendorff, K. T. Lundgaard, A. Møgelhøj, V. Petzold, D. D. Landis, J. K. Nørskov, T. Bligaard, and K. W. Jacobsen, "Density functionals for surface science: Exchange-correlation model development with Bayesian error estimation", *Physical Review B*, vol. 85, no. 23, p. 235 149, Jun. 2012. DOI: 10.1103/PhysRevB.85.235149.

[33] J. J. Mortensen, K. Kaasbjerg, S. L. Frederiksen, J. K. Nørskov, J. P. Sethna, and K. W. Jacobsen, "Bayesian error estimation in density-functional theory", *Physical Review Letters*, vol. 95, no. 21, pp. 1–4, 2005. DOI: 10.1103/PhysRevLett.95.216401.

[34] J. J. Mortensen, L. B. Hansen, and K. W. Jacobsen, "Real-space grid implementation of the projector augmented wave method", *Physical Review B - Condensed Matter and Materials Physics*, vol. 71, no. 3, pp. 1–11, 2005. DOI: 10.1103/PhysRevB.71.035109.

[35] A. H. Larsen, M. Vanin, J. J. Mortensen, K. S. Thygesen, and K. W. Jacobsen, "Localized atomic basis set in the projector augmented wave method", *Physical Review B - Condensed Matter and Materials Physics*, vol. 80, no. 19, pp. 1–10, 2009. DOI: 10.1103/PhysRevB.80.195112.

[36] J. M. Carlsson, *Pseudopotentials: From Ultrahard to Ultrasoft*, 2007. [Online]. Available: http://www.tcm.phy.cam.ac.uk/castep/CASTEP_talks_07/carlsson2.pdf.

[37] GPAW developers, *Density Of States — GPAW*. [Online]. Available: https://wiki.fysik.dtu.dk/gpaw/documentation/pdos/pdos.html.

[38] C. E. Housecroft and A. G. Sharpe, *Inorganic Chemistry, 4th Edition*, 4th. Pearson, 2012, 1256 pages.

[39] O. H. Nielsen and R. M. Martin, "First-principles calculation of stress", *Physical Review Letters*, vol. 50, no. 9, pp. 697–700, Feb. 1983. DOI: 10.1103/PhysRevLett.50.697.

[40] A. H. Larsen, J. J. Mortensen, J. Blomqvist, I. E. Castelli, R. Christensen, M. Dułak, J. Friis, M. N. Groves, B. Hammer, C. Hargus, E. D. Hermes, P. C.

Jennings, P. Bjerre Jensen, J. Kermode, J. R. Kitchin, E. Leonhard Kolsbjerg, J. Kubal, K. Kaasbjerg, S. Lysgaard, J. Bergmann Maronsson, T. Maxson, T. Olsen, L. Pastewka, A. Peterson, C. Rostgaard, J. Schiøtz, O. Schütt, M. Strange, K. S. Thygesen, T. Vegge, L. Vilhelmsen, M. Walter, Z. Zeng, and K. W. Jacobsen, "The atomic simulation environment—a Python library for working with atoms", *Journal of Physics: Condensed Matter*, vol. 29, no. 27, p. 273 002, Jul. 2017. DOI: 10.1088/1361-648X/aa680e.

[41] D. S. Sholl and J. A. Steckel, *Density Functional Theory: A Practical Introduction.* Hoboken, NJ, USA: John Wiley & Sons, Inc., Mar. 2009, 1–238 pages.

[42] A. Cooksy, *Physical Chemistry: Thermodynamics, Statistical Mechanics, & Kinetics.* 2014, 540 pages.

[43] I. Chorkendorff and J. W. Niemantsverdriet, *Concepts of Modern Catalysis and Kinetics*, 2nd. Wiley, Oct. 2007, 457 pages.

[44] K. J. Laidler and M. C. King, "The development of transition-state theory", *Journal of Physical Chemistry*, vol. 87, no. 15, pp. 2657–2664, 1983. DOI: 10.1021/j100238a002.

[45] N. E. Henriksen and F. Y. Hansen, *Theories of Molecular Reaction Dynamics.* Oxford University Press, Jan. 2008.

[46] O.-P. Koistinen, F. B. Dagbjartsdóttir, V. Ásgeirsson, A. Vehtari, and H. Jónsson, "Nudged elastic band calculations accelerated with Gaussian process regression", *The Journal of Chemical Physics*, vol. 147, no. 15, p. 152 720, Oct. 2017. DOI: 10.1063/1.4986787.

[47] H. Jónsson, G. Mills, and K. W. Jacobsen, "Nudged elastic band method for finding minimum energy paths of transitions", in *Classical and Quantum Dynamics in Condensed Phase Simulations*, World Scientific, Jun. 1998, pp. 385–404. DOI: 10.1142/9789812839664_0016.

[48] G. Henkelman, B. P. Uberuaga, and H. Jónsson, "Climbing image nudged elastic band method for finding saddle points and minimum energy paths", *Journal of Chemical Physics*, vol. 113, no. 22, pp. 9901–9904, 2000. DOI: 10.1063/1.1329672.

[49] S. Smidstrup, A. Pedersen, K. Stokbro, and H. Jónsson, "Improved initial guess for minimum energy path calculations", *The Journal of Chemical Physics*, vol. 140, no. 21, p. 214 106, Jun. 2014. DOI: 10.1063/1.4878664.

[50] G. Henkelman and H. Jónsson, "Improved tangent estimate in the nudged elastic band method for finding minimum energy paths and saddle points", *The Journal of Chemical Physics*, vol. 113, no. 22, pp. 9978–9985, Dec. 2000. DOI: 10.1063/1.1323224.

[51] A. J. Medford, C. Shi, M. J. Hoffmann, A. C. Lausche, S. R. Fitzgibbon, T. Bligaard, and J. K. Nørskov, "CatMAP: A Software Package for Descriptor-Based Microkinetic Mapping of Catalytic Trends", *Catalysis Letters*, vol. 145, no. 3, pp. 794–807, Mar. 2015. DOI: 10.1007/s10562-015-1495-6.

[52] J. Enkovaara, C. Rostgaard, J. J. Mortensen, J. Chen, M. Dułak, L. Ferrighi, J. Gavnholt, C. Glinsvad, V. Haikola, H. A. Hansen, H. H. Kristoffersen, M. Kuisma, A. H. Larsen, L. Lehtovaara, M. Ljungberg, O. Lopez-Acevedo, P. G. Moses, J. Ojanen, T. Olsen, V. Petzold, N. A. Romero, J. Stausholm-Møller, M. Strange, G. A. Tritsaris, M. Vanin, M. Walter, B. Hammer, H. Häkki-

nen, G. K. H. Madsen, R. M. Nieminen, J. K. Nørskov, M. Puska, T. T. Rantala, J. Schiøtz, K. S. Thygesen, and K. W. Jacobsen, "Electronic structure calculations with GPAW: a real-space implementation of the projector augmented-wave method", *Journal of Physics: Condensed Matter*, vol. 22, no. 25, p. 253 202, Jun. 2010. DOI: 10.1088/0953-8984/22/25/253202.

[53] H. J. Monkhorst and J. D. Pack, "Special points for Brillouin-zone integrations", *Physical Review B*, vol. 13, no. 12, pp. 5188–5192, Jun. 1976. DOI: 10.1103/PhysRevB.13.5188.

[54] P. Lindgren, G. Kastlunger, and A. A. Peterson, "Scaled and Dynamic Optimizations of Nudged Elastic Bands", *Journal of Chemical Theory and Computation*, vol. 15, no. 11, pp. 5787–5793, Nov. 2019. DOI: 10.1021/acs.jctc.9b00633.

[55] A. A. Peterson, F. Abild-Pedersen, F. Studt, J. Rossmeisl, and J. K. Nørskov, "How copper catalyzes the electroreduction of carbon dioxide into hydrocarbon fuels", *Energy and Environmental Science*, vol. 3, no. 9, pp. 1311–1315, 2010. DOI: 10.1039/c0ee00071j.

[56] F. Studt, F. Abild-Pedersen, J. B. Varley, and J. K. Nørskov, "CO and CO2 Hydrogenation to Methanol Calculated Using the BEEF-vdW Functional", *Catalysis Letters*, vol. 143, no. 1, pp. 71–73, Jan. 2013. DOI: 10.1007/s10562-012-0947-5.

[57] E. Bitzek, P. Koskinen, F. Gähler, M. Moseler, and P. Gumbsch, "Structural relaxation made simple", *Physical Review Letters*, vol. 97, no. 17, pp. 1–4, 2006. DOI: 10.1103/PhysRevLett.97.170201.

[58] J. R. Boes, O. Mamun, K. Winther, and T. Bligaard, "Graph Theory Approach to High-Throughput Surface Adsorption Structure Generation", *The Journal of Physical Chemistry A*, vol. 123, no. 11, pp. 2281–2285, Mar. 2019. DOI: 10.1021/acs.jpca.9b00311.

[59] G. Kastlunger, P. Lindgren, and A. A. Peterson, "Controlled-Potential Simulation of Elementary Electrochemical Reactions: Proton Discharge on Metal Surfaces", *The Journal of Physical Chemistry C*, vol. 122, no. 24, pp. 12 771–12 781, Jun. 2018. DOI: 10.1021/acs.jpcc.8b02465.

[60] A. Held and M. Walter, "Simplified continuum solvent model with a smooth cavity based on volumetric data", *The Journal of Chemical Physics*, vol. 141, no. 17, p. 174 108, Nov. 2014. DOI: 10.1063/1.4900838.

[61] A. Bondi, "van der Waals Volumes and Radii", *The Journal of Physical Chemistry*, vol. 68, no. 3, pp. 441–451, Mar. 1964. DOI: 10.1021/j100785a001.

[62] A. Ge, G. Kastlunger, J. Meng, P. Lindgren, J. Song, Q. Liu, A. Zaslavsky, T. Lian, and A. A. Peterson, "On the Coupling of Electron Transfer to Proton Transfer at Electrified Interfaces", *Journal of the American Chemical Society*, vol. 142, no. 27, pp. 11 829–11 834, Jul. 2020. DOI: 10.1021/jacs.0c03472.

[63] J. K. Nørskov, F. Studt, F. Abild-Pedersen, and T. Bligaard, *Fundamental Concepts in Heterogeneous Catalysis*. 2014, 196 pages.

[64] J. K. Nørskov, J. Rossmeisl, A. Logadottir, L. Lindqvist, J. R. Kitchin, T. Bligaard, and H. Jónsson, "Origin of the Overpotential for Oxygen Reduction at a Fuel-Cell Cathode", *The Journal of Physical Chemistry B*, vol. 108, no. 46, pp. 17 886–17 892, Nov. 2004. DOI: 10.1021/jp047349j.

[65] S. R. Kelly, H. H. Heenen, N. Govindarajan, K. Chan, and J. K. Nørskov, "OH Binding Energy as a Universal Descriptor of the Potential of Zero Charge on Transition Metal Surfaces", *The Journal of Physical Chemistry C*, vol. 126, no. 12, pp. 5521–5528, Mar. 2022. DOI: 10.1021/acs.jpcc.1c10362.

[66] K. Schwarz and R. Sundararaman, "The electrochemical interface in first-principles calculations", *Surface Science Reports*, vol. 75, no. 2, p. 100 492, May 2020. DOI: 10.1016/j.surfrep.2020.100492.

[67] S. Trasatti and E. Lust, "The Potential of Zero Charge", in *Modern Aspects of Electrochemistry vol. 33*, R. E. White, J. O. Bockris, and B. E. Conway, Eds., 2002, ch. 1, pp. 1–215.

[68] S. A. Akhade, I. T. McCrum, and M. J. Janik, "The Impact of Specifically Adsorbed Ions on the Copper-Catalyzed Electroreduction of CO 2", *Journal of The Electrochemical Society*, vol. 163, no. 6, F477–F484, Mar. 2016. DOI: 10.1149/2.0581606jes.

[69] J. Rossmeisl, E. Skúlason, M. E. Björketun, V. Tripkovic, and J. K. Nørskov, "Modeling the electrified solid–liquid interface", *Chemical Physics Letters*, vol. 466, no. 1-3, pp. 68–71, Nov. 2008. DOI: 10.1016/j.cplett.2008.10.024.

[70] V. Tripkovic, M. E. Björketun, E. Skúlason, and J. Rossmeisl, "Standard hydrogen electrode and potential of zero charge in density functional calculations", *Physical Review B*, vol. 84, no. 11, p. 115 452, Sep. 2011. DOI: 10.1103/PhysRevB.84.115452.

[71] P. Li, J. Huang, Y. Hu, and S. Chen, "Establishment of the Potential of Zero Charge of Metals in Aqueous Solutions: Different Faces of Water Revealed by Ab Initio Molecular Dynamics Simulations", *The Journal of Physical Chemistry C*, vol. 125, no. 7, pp. 3972–3979, Feb. 2021. DOI: 10.1021/acs.jpcc.0c11089.

[72] S. Trasatti, "The absolute electrode potential: an explanatory note (Recommendations 1986)", *Pure and Applied Chemistry*, vol. 58, no. 7, pp. 955–966, Jan. 1986. DOI: 10.1351/pac198658070955.

[73] K. Chan and J. K. Nørskov, "Electrochemical Barriers Made Simple", *The Journal of Physical Chemistry Letters*, vol. 6, no. 14, pp. 2663–2668, Jul. 2015. DOI: 10.1021/acs.jpclett.5b01043.

[74] K. Doblhoff-Dier and M. T. Koper, "Electric double layer of Pt(111): Known unknowns and unknown knowns", *Current Opinion in Electrochemistry*, vol. 39, p. 101 258, Jun. 2023. DOI: 10.1016/j.coelec.2023.101258.

[75] E. Skúlason, V. Tripkovic, M. E. Björketun, S. Gudmundsdóttir, G. Karlberg, J. Rossmeisl, T. Bligaard, H. Jónsson, and J. K. Nørskov, "Modeling the Electrochemical Hydrogen Oxidation and Evolution Reactions on the Basis of Density Functional Theory Calculations", *The Journal of Physical Chemistry C*, vol. 114, no. 42, pp. 18 182–18 197, Oct. 2010. DOI: 10.1021/jp1048887.

[76] K. Chan and J. K. Nørskov, "Potential Dependence of Electrochemical Barriers from ab Initio Calculations", *The Journal of Physical Chemistry Letters*, vol. 7, no. 9, pp. 1686–1690, May 2016. DOI: 10.1021/acs.jpclett.6b00382.

[77] J. A. Gauthier, S. Ringe, C. F. Dickens, A. J. Garza, A. T. Bell, M. Head-Gordon, J. K. Nørskov, and K. Chan, "Challenges in Modeling Electrochemical Reaction Energetics with Polarizable Continuum Models", *ACS Catalysis*, vol. 9, no. 2, pp. 920–931, Feb. 2019. DOI: 10.1021/acscatal.8b02793.

[78] G. S. Karlberg and G. Wahnström, "Density-Functional Based Modeling of the Intermediate in the Water Production Reaction on Pt(111)", *Physical Review Letters*, vol. 92, no. 13, p. 136 103, Apr. 2004. DOI: 10.1103/PhysRevLett.92.136103.

[79] K. Mathew, R. Sundararaman, K. Letchworth-Weaver, T. A. Arias, and R. G. Hennig, "Implicit solvation model for density-functional study of nanocrystal surfaces and reaction pathways", *The Journal of Chemical Physics*, vol. 140, no. 8, p. 084 106, Feb. 2014. DOI: 10.1063/1.4865107.

[80] G. Kresse and J. Hafner, "Ab initio molecular dynamics for liquid metals", *Physical Review B*, vol. 47, no. 1, pp. 558–561, Jan. 1993. DOI: 10.1103/PhysRevB.47.558.

[81] K. Mathew, V. S. C. Kolluru, S. Mula, S. N. Steinmann, and R. G. Hennig, "Implicit self-consistent electrolyte model in plane-wave density-functional theory", *The Journal of Chemical Physics*, vol. 151, no. 23, p. 234 101, Dec. 2019. DOI: 10.1063/1.5132354.

[82] J. A. Gauthier, C. F. Dickens, H. H. Heenen, S. Vijay, S. Ringe, and K. Chan, "Unified Approach to Implicit and Explicit Solvent Simulations of Electrochemical Reaction Energetics", *Journal of Chemical Theory and Computation*, vol. 15, no. 12, pp. 6895–6906, Dec. 2019. DOI: 10.1021/acs.jctc.9b00717.

[83] S. Vijay, W. Ju, S. Brückner, S.-C. Tsang, P. Strasser, and K. Chan, "Unified mechanistic understanding of CO2 reduction to CO on transition metal and single atom catalysts", *Nature Catalysis*, vol. 4, no. 12, pp. 1024–1031, Nov. 2021. DOI: 10.1038/s41929-021-00705-y.

[84] S. Vijay, G. Kastlunger, J. A. Gauthier, A. Patel, and K. Chan, "Force-Based Method to Determine the Potential Dependence in Electrochemical Barriers", *The Journal of Physical Chemistry Letters*, vol. 13, no. 25, pp. 5719–5725, Jun. 2022. DOI: 10.1021/acs.jpclett.2c01367.

[85] L. Formaro and S. Trasatti, "Capacitance measurements on platinum electrodes for the estimation of organic impurities in water", *Analytical Chemistry*, vol. 40, no. 7, pp. 1060–1067, Jun. 1968. DOI: 10.1021/ac60263a003.

[86] J. Li, J. H. Stenlid, T. Ludwig, P. S. Lamoureux, and F. Abild-Pedersen, "Modeling Potential-Dependent Electrochemical Activation Barriers: Revisiting the Alkaline Hydrogen Evolution Reaction", *Journal of the American Chemical Society*, vol. 143, no. 46, pp. 19 341–19 355, Nov. 2021. DOI: 10.1021/jacs.1c07276.

[87] A. M. Abdellah, F. Ismail, O. W. Siig, J. Yang, C. M. Andrei, L.-A. DiCecco, A. Raksha, K. E. Salem, K. Grandfield, N. Bassim, R. Black, G. Kastlunger, L. Soleymani, and D. Higgins, "In-Situ Liquid Phase Transmission Electron Microscopy and Electron Diffraction Provides Mechanistic Insight into Electrochemical CO2 Reduction on Palladium/Palladium Hydride Catalysts", *ChemRxiv*, 2023. DOI: 10.26434/chemrxiv-2023-t0b00.

[88] X. Yu and P. G. Pickup, "Recent advances in direct formic acid fuel cells (DFAFC)", *Journal of Power Sources*, vol. 182, no. 1, pp. 124–132, Jul. 2008. DOI: 10.1016/j.jpowsour.2008.03.075.

[89] Y. Hori, A. Murata, and R. Takahashi, "Formation of hydrocarbons in the electrochemical reduction of carbon dioxide at a copper electrode in aqueous solution", *Journal of the Chemical Society, Faraday Transactions 1: Physical*

Chemistry in Condensed Phases, vol. 85, no. 8, p. 2309, 1989. DOI: 10.1039/f19898502309.

[90]   X. Min and M. W. Kanan, "Pd-Catalyzed Electrohydrogenation of Carbon Dioxide to Formate: High Mass Activity at Low Overpotential and Identification of the Deactivation Pathway", *Journal of the American Chemical Society*, vol. 137, no. 14, pp. 4701–4708, Apr. 2015. DOI: 10.1021/ja511890h.

[91]   W. Zhu, S. Kattel, F. Jiao, and J. G. Chen, "Shape-Controlled CO 2 Electrochemical Reduction on Nanosized Pd Hydride Cubes and Octahedra", *Advanced Energy Materials*, vol. 9, no. 9, p. 1 802 840, Mar. 2019. DOI: 10.1002/aenm.201802840.

[92]   C. Langhammer, E. M. Larsson, B. Kasemo, and I. Zorić, "Indirect Nanoplasmonic Sensing: Ultrasensitive Experimental Platform for Nanomaterials Science and Optical Nanocalorimetry", *Nano Letters*, vol. 10, no. 9, pp. 3529–3538, Sep. 2010. DOI: 10.1021/nl101727b.

[93]   A. T. Landers, H. Peng, D. M. Koshy, S. H. Lee, J. T. Feaster, J. C. Lin, J. W. Beeman, D. Higgins, J. Yano, W. S. Drisdell, R. C. Davis, M. Bajdich, F. Abild-Pedersen, A. Mehta, T. F. Jaramillo, and C. Hahn, "Dynamics and Hysteresis of Hydrogen Intercalation and Deintercalation in Palladium Electrodes: A Multimodal In Situ X-ray Diffraction, Coulometry, and Computational Study", *Chemistry of Materials*, vol. 33, no. 15, pp. 5872–5884, Aug. 2021. DOI: 10.1021/acs.chemmater.1c00291.

[94]   D. Gao, H. Zhou, F. Cai, D. Wang, Y. Hu, B. Jiang, W.-B. Cai, X. Chen, R. Si, F. Yang, S. Miao, J. Wang, G. Wang, and X. Bao, "Switchable CO2 electroreduction via engineering active phases of Pd nanoparticles", *Nano Research*, vol. 10, no. 6, pp. 2181–2191, Jun. 2017. DOI: 10.1007/s12274-017-1514-6.

[95]   S. Setayandeh, C. Webb, and E. M. Gray, "Electron and phonon band structures of palladium and palladium hydride: A review", *Progress in Solid State Chemistry*, vol. 60, p. 100 285, Dec. 2020. DOI: 10.1016/j.progsolidstchem.2020.100285.

[96]   S. Alvarez, "A cartography of the van der Waals territories", *Dalton Transactions*, vol. 42, no. 24, p. 8617, 2013. DOI: 10.1039/c3dt50599e.

[97]   Y. Zhao, X. Tan, W. Yang, C. Jia, X. Chen, W. Ren, S. C. Smith, and C. Zhao, "Surface Reconstruction of Ultrathin Palladium Nanosheets during Electrocatalytic CO 2 Reduction", *Angewandte Chemie International Edition*, vol. 59, no. 48, pp. 21 493–21 498, Nov. 2020. DOI: 10.1002/anie.202009616.

[98]   J. S. Yoo, R. Christensen, T. Vegge, J. K. Nørskov, and F. Studt, "Theoretical Insight into the Trends that Guide the Electrochemical Reduction of Carbon Dioxide to Formic Acid", *ChemSusChem*, vol. 9, no. 4, pp. 358–363, Feb. 2016. DOI: 10.1002/cssc.201501197.

[99]   S. Zhao, S. Li, T. Guo, S. Zhang, J. Wang, Y. Wu, and Y. Chen, "Advances in Sn-Based Catalysts for Electrochemical CO2 Reduction", *Nano-Micro Letters*, vol. 11, no. 1, p. 62, Dec. 2019. DOI: 10.1007/s40820-019-0293-x.

[100]   J. T. Feaster, C. Shi, E. R. Cave, T. Hatsukade, D. N. Abram, K. P. Kuhl, C. Hahn, J. K. Nørskov, and T. F. Jaramillo, "Understanding Selectivity for the Electrochemical Reduction of Carbon Dioxide to Formic Acid and Carbon

Monoxide on Metal Electrodes", *ACS Catalysis*, vol. 7, no. 7, pp. 4822–4827, Jul. 2017. DOI: 10.1021/acscatal.7b00687.

[101] N. Govindarajan, G. Kastlunger, H. H. Heenen, and K. Chan, "Improving the intrinsic activity of electrocatalysts for sustainable energy conversion: where are we and where can we go?", *Chemical Science*, vol. 13, no. 1, pp. 14–26, 2022. DOI: 10.1039/D1SC04775B.

[102] Y. Hori, "Electrochemical CO2 Reduction on Metal Electrodes", in *Modern Aspects of Electrochemistry vol. 42*, C. Vayenas, R. White, and M. Gamboa-Aldeco, Eds., New York, NY: Springer New York, 2008, pp. 89–189. DOI: 10.1007/978-0-387-49489-0_3.

[103] A. Bagger, W. Ju, A. S. Varela, P. Strasser, and J. Rossmeisl, "Electrochemical CO 2 Reduction: A Classification Problem", *ChemPhysChem*, vol. 18, no. 22, pp. 3266–3273, Nov. 2017. DOI: 10.1002/cphc.201700736.

[104] W. Deng, P. Zhang, B. Seger, and J. Gong, "Unraveling the rate-limiting step of two-electron transfer electrochemical reduction of carbon dioxide", *Nature Communications*, vol. 13, no. 1, p. 803, Feb. 2022. DOI: 10.1038/s41467-022-28436-z.

[105] S. Verma, Y. Hamasaki, C. Kim, W. Huang, S. Lu, H.-R. M. Jhong, A. A. Gewirth, T. Fujigaya, N. Nakashima, and P. J. A. Kenis, "Insights into the Low Overpotential Electroreduction of CO 2 to CO on a Supported Gold Catalyst in an Alkaline Flow Electrolyzer", *ACS Energy Letters*, vol. 3, no. 1, pp. 193–198, Jan. 2018. DOI: 10.1021/acsenergylett.7b01096.

[106] I. V. Chernyshova, P. Somasundaran, and S. Ponnurangam, "On the origin of the elusive first intermediate of CO 2 electroreduction", *Proceedings of the National Academy of Sciences*, vol. 115, no. 40, E9261–E9270, Oct. 2018. DOI: 10.1073/pnas.1802256115.

[107] J. Resasco, L. D. Chen, E. Clark, C. Tsai, C. Hahn, T. F. Jaramillo, K. Chan, and A. T. Bell, "Promoter Effects of Alkali Metal Cations on the Electrochemical Reduction of Carbon Dioxide", *Journal of the American Chemical Society*, vol. 139, no. 32, pp. 11 277–11 287, Aug. 2017. DOI: 10.1021/jacs.7b06765.

[108] L. D. Chen, M. Urushihara, K. Chan, and J. K. Nørskov, "Electric Field Effects in Electrochemical CO 2 Reduction", *ACS Catalysis*, vol. 6, no. 10, pp. 7133–7139, Oct. 2016. DOI: 10.1021/acscatal.6b02299.

[109] S. Ringe, E. L. Clark, J. Resasco, A. Walton, B. Seger, A. T. Bell, and K. Chan, "Understanding cation effects in electrochemical CO2 reduction", *Energy & Environmental Science*, vol. 12, no. 10, pp. 3001–3014, 2019. DOI: 10.1039/C9EE01341E.

[110] M. Liu, Y. Pang, B. Zhang, P. De Luna, O. Voznyy, J. Xu, X. Zheng, C. T. Dinh, F. Fan, C. Cao, F. P. G. de Arquer, T. S. Safaei, A. Mepham, A. Klinkova, E. Kumacheva, T. Filleter, D. Sinton, S. O. Kelley, and E. H. Sargent, "Enhanced electrocatalytic CO2 reduction via field-induced reagent concentration", *Nature*, vol. 537, no. 7620, pp. 382–386, Sep. 2016. DOI: 10.1038/nature19060.

[111] Y. Zhou, Y. Liang, J. Fu, K. Liu, Q. Chen, X. Wang, H. Li, L. Zhu, J. Hu, H. Pan, M. Miyauchi, L. Jiang, E. Cortés, and M. Liu, "Vertical Cu Nanoneedle Arrays Enhance the Local Electric Field Promoting C 2 Hydrocarbons in the

CO 2 Electroreduction", *Nano Letters*, vol. 22, no. 5, pp. 1963–1970, Mar. 2022. DOI: 10.1021/acs.nanolett.1c04653.

[112] R. Kas, K. Yang, D. Bohra, R. Kortlever, T. Burdyny, and W. A. Smith, "Electrochemical CO 2 reduction on nanostructured metal electrodes: fact or defect?", *Chemical Science*, vol. 11, no. 7, pp. 1738–1749, 2020. DOI: 10.1039/C9SC05375A.

[113] M. Giesen, "An Atomistic View on Fundamental Transport Processes on Metal Surfaces", in *AIP Conference Proceedings*, vol. 916, AIP, 2007, pp. 115–135. DOI: 10.1063/1.2751912.

[114] K. Chan and M. Eikerling, "A Pore-Scale Model of Oxygen Reduction in Ionomer-Free Catalyst Layers of PEFCs", *Journal of The Electrochemical Society*, vol. 158, no. 1, B18, 2011. DOI: 10.1149/1.3505042.

[115] S. Ringe, C. G. Morales-Guio, L. D. Chen, M. Fields, T. F. Jaramillo, C. Hahn, and K. Chan, "Double layer charging driven carbon dioxide adsorption limits the rate of electrochemical carbon dioxide reduction on Gold", *Nature Communications*, vol. 11, no. 1, p. 33, Dec. 2020. DOI: 10.1038/s41467-019-13777-z.

[116] P. Connor, J. Schuch, B. Kaiser, and W. Jaegermann, "The Determination of Electrochemical Active Surface Area and Specific Capacity Revisited for the System MnO x as an Oxygen Evolution Catalyst", *Zeitschrift für Physikalische Chemie*, vol. 234, no. 5, pp. 979–994, May 2020. DOI: 10.1515/zpch-2019-1514.

[117] S. Mezzavilla, S. Horch, I. E. L. Stephens, B. Seger, and I. Chorkendorff, "Structure Sensitivity in the Electrocatalytic Reduction of CO 2 with Gold Catalysts", *Angewandte Chemie International Edition*, vol. 58, no. 12, pp. 3774–3778, Mar. 2019. DOI: 10.1002/anie.201811422.

[118] R. G. Mariano, M. Kang, O. J. Wahab, I. J. McPherson, J. A. Rabinowitz, P. R. Unwin, and M. W. Kanan, "Microstructural origin of locally enhanced CO2 electroreduction activity on gold", *Nature Materials*, Mar. 2021. DOI: 10.1038/s41563-021-00958-9.

[119] Y. Chen, C. W. Li, and M. W. Kanan, "Aqueous CO 2 Reduction at Very Low Overpotential on Oxide-Derived Au Nanoparticles", *Journal of the American Chemical Society*, vol. 134, no. 49, pp. 19 969–19 972, Dec. 2012. DOI: 10.1021/ja309317u.

[120] M. Dunwell, Q. Lu, J. M. Heyes, J. Rosen, J. G. Chen, Y. Yan, F. Jiao, and B. Xu, "The Central Role of Bicarbonate in the Electrochemical Reduction of Carbon Dioxide on Gold", *Journal of the American Chemical Society*, vol. 139, no. 10, pp. 3774–3783, Mar. 2017. DOI: 10.1021/jacs.6b13287.

A Included Publications

A.1 Paper I

***In-Situ* Liquid Phase Transmission Electron Microscopy and Electron Diffraction Provides Mechanistic Insight into Electrochemical CO2 Reduction on Palladium/Palladium Hydride Catalysts**

Ahmed M. Abdellah, Fatma Ismail, Oliver W. Siig, Jie Yang, Carmen M Andrei, Liza-Anastasia DiCecco, Amirhossein Rakhsha, Kholoud E Salem, Kathryn Grandfield, Nabil Bassim, Robert Black, Georg Kastlunger, Leyla Soleymani, Drew Higgins

Submitted to Nature Materials

In-Situ Liquid Phase Transmission Electron Microscopy and Electron Diffraction Provides Mechanistic Insight into Electrochemical CO₂ Reduction on Palladium/Palladium Hydride Catalysts

Ahmed M. Abdellah[1], Fatma Ismail[1], Oliver W. Siig[7], Jie Yang,[5] Carmen M Andrei[2], Liza Anastasia DiCecco[3], Amirhossein Rakhsha[1], Kholoud E Salem[1], Kathryn Grandfield[3,4], Nabil Bassim[2,3], Robert Black[6], Georg Kastlunger[7], Leyla Soleymani[4,5], Drew Higgins[1,2*]

1- Department of Chemical Engineering, McMaster University, Hamilton, Ontario L8S 4L7, Canada

2- Canadian Centre for Electron Microscopy, McMaster University, Hamilton, Canada

3- Department of Materials Science and Engineering, McMaster University, Hamilton, ON, Canada

4- School of Biomedical Engineering, McMaster University, Hamilton, Canada

5- Department of Engineering Physics, McMaster University, Hamilton, Canada

6- National Research Council of Canada, Energy, Mining, and Environment Research Centre, 2620 Speakman Drive, Mississauga, ON L5K 2L1, Canada

7- CatTheory, Physics Department, Denmark Technical University, Kongens Lyngby 2800, Denmark

*higgid2@mcmaster.ca

Abstract

Electrochemical conversion of CO₂ (CO₂R) offers a sustainable route for producing fuels and chemicals. Pd-based catalysts are effective for selective conversion of CO₂ into formate at low overpotentials and CO/H2 at high overpotentials. Furthermore, Pd catalysts undergo morphology and phase structure transformations under reaction conditions that are not well understood. Herein, *in-situ* liquid phase transmission electron microscopy (LP-TEM) and select area diffraction (SAD) measurements under CO₂R conditions is applied to track the morphology and Pd/PdHₓ phase

1

interconversion as a function of electrode potential, respectively. Correlating in-situ characterization with electrochemical CO_2R activity/selectivity measurements, density functional theory and micro-kinetic analyses, the change in Pd/PdH_x catalyst selectivity from formate at low overpotentials towards CO/H_2 at higher overpotentials is found to result from electrode potential-dependent thermodynamic changes in the reaction energetics and not morphological or phase structure changes, providing insight that can guide advanced understanding and design of improved performance catalysts.

Introduction

Electrochemical conversion of CO_2 using renewable electricity is envisaged as an integral component of a future sustainable energy economy by providing an avenue for producing carbon-based fuels and chemicals from non-fossil fuel feedstocks. Nevertheless, electrochemical CO_2 conversion technologies require efficient, selective, and stable electrocatalysts for CO_2 reduction (CO_2R) reactions. The activity and selectivity of catalysts for CO_2R and the competing hydrogen evolution reaction (HER) are known to depend on the binding energies of adsorbed reaction intermediates, for example, *CO or *H, respectively, where * denotes an adsorbed species.[1] The binding energies between adsorbed species and the catalyst surface are dictated by the nature of the catalytically active site structure(s) present in the catalyst and can be modulated by tuning the catalyst properties by strategies such as alloying,[2-5] surface modification or the exposure to different surface facets.[6-8]

Palladium-based electrocatalysts provide the lowest known overpotential for the CO_2R among all reported catalysts.[9,10] Particularly, Pd exhibits high selectively (> 90%) for reducing CO_2 into formate at low overpotentials (< 200 mV).[9] At higher overpotentials, Pd catalysts become selective towards the formation of H_2 and CO, including Faradaic efficiencies towards CO above 90% recorded at overpotentials of ca. 500 mV.[11] Under electrochemical CO_2R conditions, Pd undergoes transformation into Pd-hydride (PdH_x) phases.[12-25] Based on the stoichiometric ratio of hydrogen (x) in PdH_x, α- and β-phase PdH_x are formed in the range of $0 < x \leq 0.03$ and $x \geq 0.58$, respectively, while α- and β-phase PdH_x coexist in the $0.03 < x < 0.58$ region.[14,26] These phase transformations cause the surface structure, electronic properties and lattice spacing of the PdH_x catalyst to vary, thus affecting catalytic activity and selectivity.[24,25,27-29] Furthermore, the

(electro)chemical environment experienced under CO_2R conditions cause changes to the structure and properties of the electrocatalyst.[7,9,30,31] Observing these changes under reaction conditions and correlating the results with measured catalytic properties can provide crucial mechanistic insight into catalytic activity and stability.

Various techniques have been developed to investigate Pd/PdH_x phase transformations and/or quantify the resulting H:Pd ratios. Using deuterium (D) instead of hydrogen, D:Pd ratios have been quantified by electrolytically forming PdD_x structures and then liberating D_2 by heating and measuring the amount of gas released.[32,33] Such techniques are not amenable to Pd/PdH_x catalysts under CO_2 reduction conditions, which require applying external electrochemical potentials in the presence of liquid electrolytes. *In-situ* (*operando*) measurements including X-ray diffraction (XRD) and extended X-ray absorption fine structure (EXAFS) have been employed to identify the lattice parameters and interatomic distances of Pd/PdH_x phases, respectively.[34-38] Landers et al.[39] utilized *in-situ* synchrotron XRD and coulometry measurements to understand intercalation/ deintercalation processes for hydrogen in palladium, enabling determination of the electrode potentials where α- and β-PdH_x phases were formed.[39] Gao et al.[10] utilized *in-situ* XAS to demonstrate the coexistence of α- and β-phases at potentials above -0.2 V (vs. the reversible hydrogen electrode, RHE), which promoted electrochemical CO_2R into formate via a HCOO* intermediate. At potentials below -0.5 V vs. RHE, the formation of β-PdH_x was observed and claimed to promote formation of CO via a COO*H intermediate.[10] While these in-situ synchrotron-based techniques provide in-situmonitoring of phase structure transformations, they do not provide opportunity to simultaneously observe morphological changes in Pd-based catalyst particles under CO_2 reduction conditions that have necessary implications on overall catalytic activity.

In-situ liquid-phase (scanning) transmission electron microscopy (LP-(S)TEM) provided opportunity to observe morphological/compositional changes of catalysts under electrochemical conditions.[7,40,41] With appropriate instrumentation these measurements can be conducted at electron microscopy facilities, which for many researchers are more readily available and accessible than specialized research facilities, such as synchrotrons. Using *in-situ* LP-(S)TEM, advanced insight into catalyst properties with spatial resolution under reaction conditions can be achieved by correlating morphological imaging with analytical techniques such as select area diffraction (SAD) and energy dispersive X-ray (EDX) analysis. A previously *in-situ* LP-(S)TEM

study monitored the morphological evolution of Pd particles under electrochemical conditions, including during the electrodeposition of Pd particles[42] or their morphological evolution under potential cycling,[43] but this work was not done in the context of electrocatalysis and the formation of PdH_x phases was not probed. The formation of PdH_x phases has been imaged previously by in-situ TEM, however these studies were conducted using either an *in-situ* environmental gas cell[44] or via LP-(S)TEM electron energy loss spectroscopy (EELS) measurements[45]. These measurements were done in the absence of electrode potential and are therefore not pertinent to electrochemical CO_2R investigations.

Despite advancements in *in-situ* LP-(S)TEM capabilities, detailed investigations of morphological changes in Pd-based catalysts under CO_2R conditions have not been investigated. Furthermore, implementation of *in-situ* SAD measurements under electrochemical conditions during LP-(S)TEM workflows has never been reported, yet provides opportunity to simultaneously measure and track phase structure transformations in catalysts under reaction conditions. Herein, *in-situ* LP-(S)TEM measurements on electro-deposited Pd/PdH_x catalysts were employed to track morphological changes under electrochemical CO_2R conditions alongside LP-TEM/SAD patterns collected to probe the interconversion between metallic Pd and PdH_x phases. Distinct morphological changes occurring in the catalyst structures under electrochemical CO_2R conditions were observed alongside a phase transformation from metallic Pd to PdH_x at electrochemical CO_2R relevant potentials. Increasing lattice expansion due to increased absorption of H atoms occurred at more negative electrode potentials, seemingly giving rise to dramatic CO_2R selectivity changes from nearly exclusive production of formate at -0.2 V vs RHE towards the production of CO and H_2 at -0.5 V vs RHE. However, density functional theory (DFT) calculations complemented by micro-kinetic analyses ascribed the CO_2R selectivity shift to changes in reaction energetics resulting from the applied electrode potential and not due to the phase structure transformations. Ultimately, *in-situ* LP-(S)TEM imaging coupled with SAD analysis under electrochemical CO_2R conditions has been demonstrated for simultaneously observing morphology and phase structure changes, and has been coupled with electro-catalytic activity/selectivity measurements and computational analysis to provide new mechanistic insight into Pd-based catalysts for the electrochemical CO_2R.

Results and discussion:

Electrode preparation:

Figure 1 shows schematics of the two CO_2 electrolysis configurations used in this work. The first is the Protochips Poseidon Select *in-situ* LP-TEM electrochemical liquid cell microchip reactor (**Figure 1a**) employing a glassy carbon working electrode decorated with Pd particles for *in-situ* characterization under CO_2R conditions. The second is a two-compartment cell consisting of a large-format working electrode (**Figure 1b**) decorated with Pd particles to measure catalytic activity and selectivity towards CO_2R. Pd particles were deposited on the microchip glassy carbon working electrode (**Figure 1c**, and **Figure S1**) by electrodeposition after assembling the *in-situ* electrochemical TEM liquid reactor, and the same electrodeposition procedure was used for preparing large-format electrodes (**Figure 1d**). Electro-deposition of Pd particles on both the microchip (**Figure 1c**) and the large format electrode (**Figure 1d**) was observed by SEM imaging. Cyclic voltammetry measurements were collected in N_2 saturated 0.1 M $KHCO_3$ for the Pd particle decorated microchip glassy carbon working electrode (**Figure 1e**) and the Pd decorated large-format electrodes (**Figure 1f**), demonstrating similar features that suggest similar local chemical environments at the Pd-decorated working electrode in the two different electrochemical reactors. The redox characteristics observed via cyclic voltammetry were characteristic of Pd-based catalysts.[9] By comparing the cyclic voltammetry features of Pd, the Pt reference electrode employed in the microchip reactor was calibrated to the RHE scale, whereby 0.76 V vs. Pt corresponds to 0 V vs. RHE (**Figure S2**), in close agreement with previously reported values.[46,47] All subsequent potentials will be reported versus RHE.
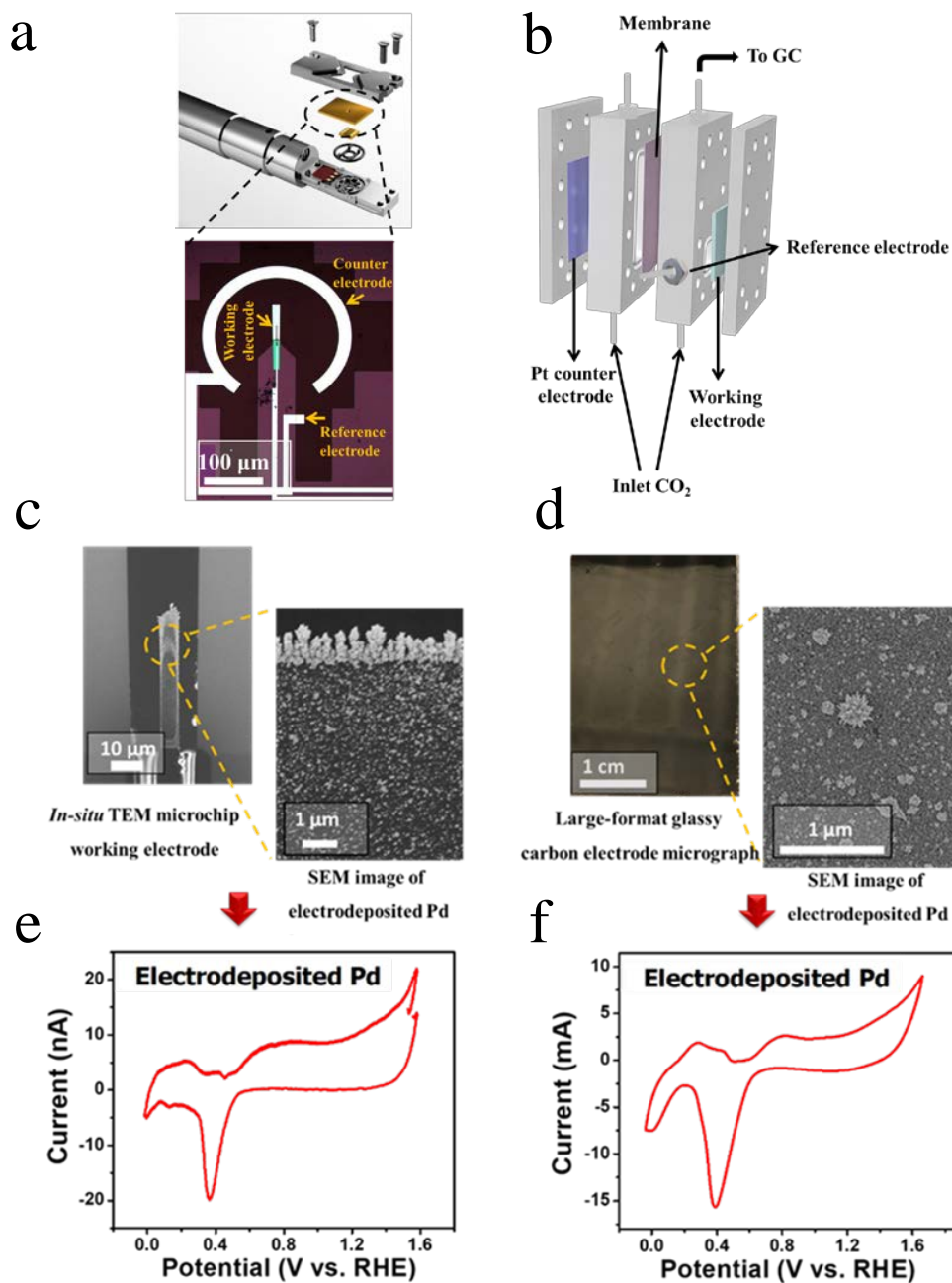
Figure 1. Schematics of the two CO₂ electrolysis cells utilized in this work: **a,** Protochips Poseidon *in-situ* LP-(S)TEM holder consisting of a Pd decorated glassy carbon working electrode within a microchip electrochemical cell. **b,** Two-compartment electrochemical cell

consisting of a large-format Pd decorated glassy carbon working electrode for electrochemical CO_2R activity and selectivity measurements. **c,** SEM images of the *in-situ* TEM microchip working electrode coated with electrodeposited Pd particles. **d,** Micrograph of the large-format glassy carbon electrode and SEM image of the electrodeposited Pd particles. **e,** Cyclic voltammetry measurements of electrodeposited Pd particles measured in the *in-situ* TEM microchip electrochemical cell. **f,** Cyclic voltammetry measurements of electrodeposited Pd particles measured in the two-compartment cell using the large-format electrode. Note that all cyclic voltammetry measurements were collected in N_2 saturated 0.1M $KHCO_3$ at a scan rate of 50 mV/s.

SEM was employed to probe the morphology of electrodeposited Pd within the *in-situ* electrochemical TEM microchip reactor (**Figure 2a-c),** revealing semi-spherical particles covering the electrode surface and dendrimer-type structures at the electrode edges. **Figure 2d** and **e** show *in-situ* liquid phase high-angle annular dark-field scanning transmission electron microscopy (LP HAADF-STEM) images at various magnification and **Figure2f** shows *in-situ* LP-HAADF-STEM/EDX mapping of the deposited Pd . A similar morphology was observed for the Pd electrodeposited on the large-format glassy carbon electrodes prepared for CO_2R activity and selectivity measurements (**Figure S3**).
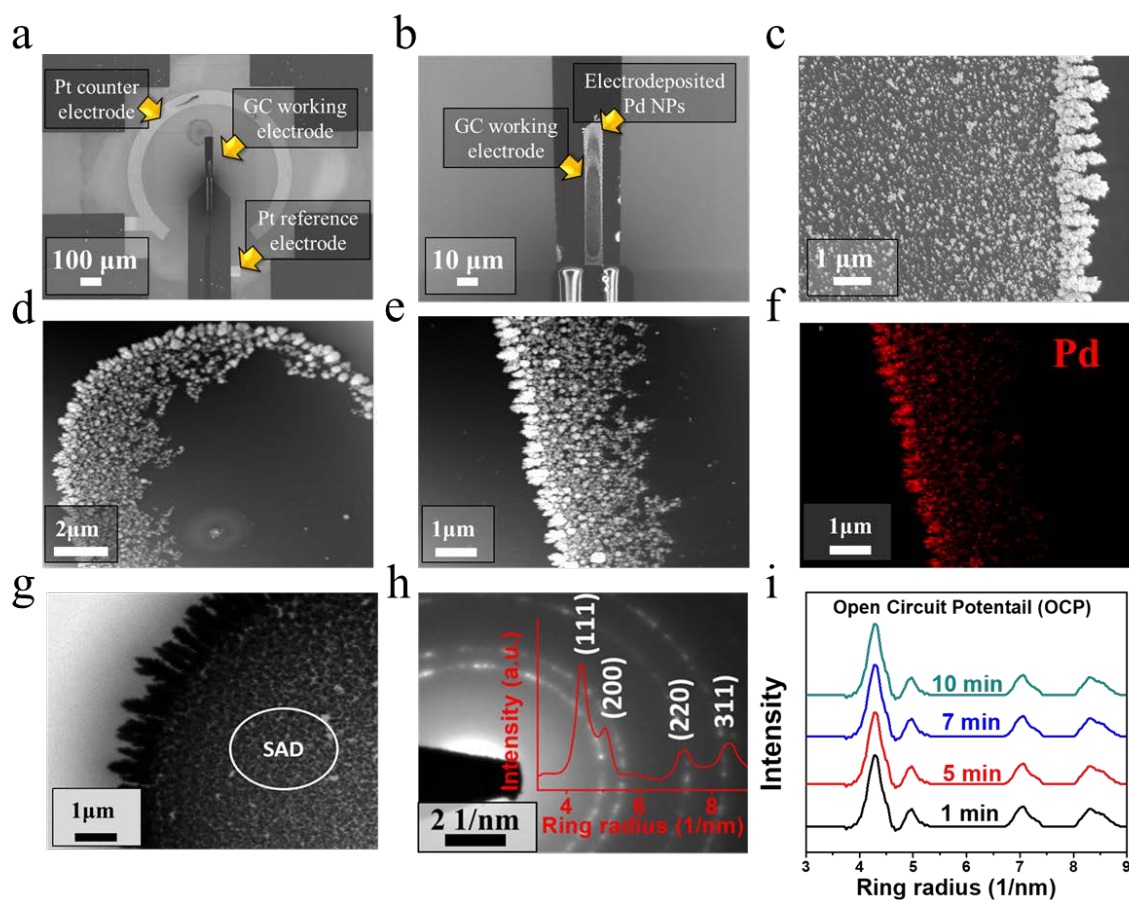
Figure 2. Structural characterization of Pd catalysts deposited on the electrochemical in-situ LP-(S)TEM microchip. **a,** SEM image of the three electrode-configuration of the *in-situ* LP-(S)TEM microchip cell. **b-c,** SEM of the working electrode showing electro-deposited Pd particles. **d-e,** *In-situ* LP-HAADF-STEM images of the working electrode at various magnification. **f,** *In-situ* LP-HAADF-STEM-EDX mapping of the electrodeposited Pd particles on the working electrode**.** **g,** *In-situ* LP-TEM imaging of Pd particles indicating the region where SAD patterns were measured. **h,** *In-situ* LP-TEM/SAD pattern of Pd particles at open circuit potential and radial intensity profiles of the diffraction patterns using the *in-situ* electrochemical TEM liquid reactor. **i,** Radial intensity profiles of the diffraction patterns at different beam irradiation times at a flow rate of 5 μL/min and a beam dose of 37 e$^-$/nm^2.s. The acquisition time for the SAD patterns was set to be 1sec.

In-situ **(S)TEM/SAD:**

In-situ LP-TEM and SAD (LP-TEM/SAD) characterization was conducted to investigate the morphology and phase structures of Pd particles under electrochemical CO_2R conditions. Prior to the measurements, *in-situ* LP-TEM images (**Figure 2g**) and *in-situ* LP-TEM/SAD patterns with radial intensity profiles (**Figure 2i**) were collected at open circuit potential. To ensure the diffraction patterns observed were from the Pd particles, *in-situ* LP-TEM/SAD patterns were also collected from an area of the electrode that did not contain any Pd particles (**Figure S4a**). No diffraction rings or spots were observed (**Figure S4b**), indicating that the glassy carbon working electrode, the SiN_x windows, and the electrolyte did not contribute to the measurements. Repeated *in-situ* LP-TEM/SAD measurements were conducted on the Pd particles at open circuit potential to evaluate if the electron beam dose applied (39.7 electron/nm^2.frame, whereby each frame = 1 second) had any impact on the phase of the Pd particles. No phase transformations as a function of beam dose were observed, in agreement with a recent report investigating the impact of beam dose on Pd/PdH_x interconversion, indicating no Pd to PdH_x transformations occurred at beam doses as high as ca. 3,900 electron/nm^2.sec.[45] In the present work no morphology changes in Pd were observed during LP-TEM measurements at open circuit potential, indicating the electron beam dose employed in does not induce morphology or phase structure changes.

In-situ LP-(S)TEM imaging of Pd particles in CO_2 saturated 0.1M $KHCO_3$ as a function of electrode potential was conducted, with results illustrated in **Figure 3**. HAADF-STEM images at 1.2 V vs RHE and after 27s of applying an electrode potential of -0.2 V vs. RHE (extracted from **Video S1**) are shown in **Figures 3a** and **b**, respectively. The corresponding *in-situ* LP-TEM/SAD patterns of the Pd particles are also shown for an electrode potential of 1.2 V vs RHE (**Figure 3c**) and -0.2 V vs RHE (**Figure 3d**). Going from 1.2 to -0.2 V vs RHE, the size of the Pd particles increased (**Figure 3b**, with images from additional locations shown in **Figure S5**) and the radial distance of the SAD patterns noticeably decreased, suggesting an expansion of the Pd crystal lattice (**Video S1**). To analyze collected *in-situ* LP-TEM/SAD patterns, radial intensity profiles were extracted using the CrysTBox-ringGUI[48] and the crystallographic information file (cif) acquired from the crystal structure database was used to index the patterns. Examples are shown in **Figures 3c, 3d, S6 and S7**. This method was used to calculate the d-spacing of the Pd-based particles from *in-situ* LP-TEM/SAD patterns, which increased upon applying an electrode potential of -0.2 V vs

RHE (**Video S2**). The observed lattice expansion is likely attributed to hydrogen absorption and intercalation into Pd, resulting in the formation of different PdH_x phases.

To more closely probe the phase transformations occurring under electrochemical CO_2R conditions, *in-situ* LP-TEM/SAD patterns of Pd-based catalysts were collected at several CO_2R relevant electrode potentials. Before applying CO_2R relevant potentials, a potential of 1.2 V vs. RHE (significantly more anodic than CO_2R conditions) was applied for 60 s to ensure the Pd catalyst was in the same starting state before all *in* measurements as hysteresis in the Pd/PdH_x conversion is a known phenomenon.[39] After 60sec at .2 V vs. RHE, the Pd particles were in their metallic state (**Figure S6**) and the electrode potential was stepped to progressively more negative values (although always returning back to 1.2 V vs. RHE between each potential). The electrode potential profiles used in this work are depicted in **Figure S8**, and *in-situ* LP-TEM/SAD patterns collected at each measurement potential are shown in **Figure 3e**. Peak locations from the *in-situ* LP-TEM/SAD patterns were used to calculate crystal lattice spacing values which are shown in **Figure 3f** for the (111) diffraction plane.

In-situ LP-TEM/SAD measurements indicated crystal lattice expansion and compression based on the applied electrode potential. At 0.6, 0.8 and 1.2 V vs. RHE, Pd is in the metallic fcc form with Pd(111) d-spacings of 2.27 Å, 2.26 Å and 2.25 Å, respectively, in alignment with the theoretical value of 2.25 Å obtained from the cif database using CrysTBox-ringGUI (**Figure S6** and **Table S1**)[48] shown as the dashed blue line in Figure 3f. At 0.3 V vs. RHE, an increase in the d-spacing value to 2.31 Å was observed, likely due to the formation of the α-PdH_x phase and consistent with the recent study *in-situ* XRD study by Landers et al.[39] In the present work, as the electrode potential was stepped more negatively to -0.1 V vs. RHE, a further lattice expansion to 2.34 Å was calculated from the diffraction pattern, likely attributed to the formation of a mixture of the α- and β-PdH_x phases in agreement with previously reported DFT calculation.[10] The dashed red line in **Figure 3f** represents the theoretical value for β-phase PdH_x, obtained from the cif database using CrysTBox-ringGUI; whereas **Figure S7 and Table S2** demonstrate the comparison of the theoretical and experimental values of PdH_x. At electrode potnetials below -0.2 V vs. RHE, β-PdH_x was found to be the predominant phase with further lattice expansion. Noted that all the experimental d-spacing calculations were estimated using the Crystal Box software with an accuracy $\pm$ 0.02 Å.
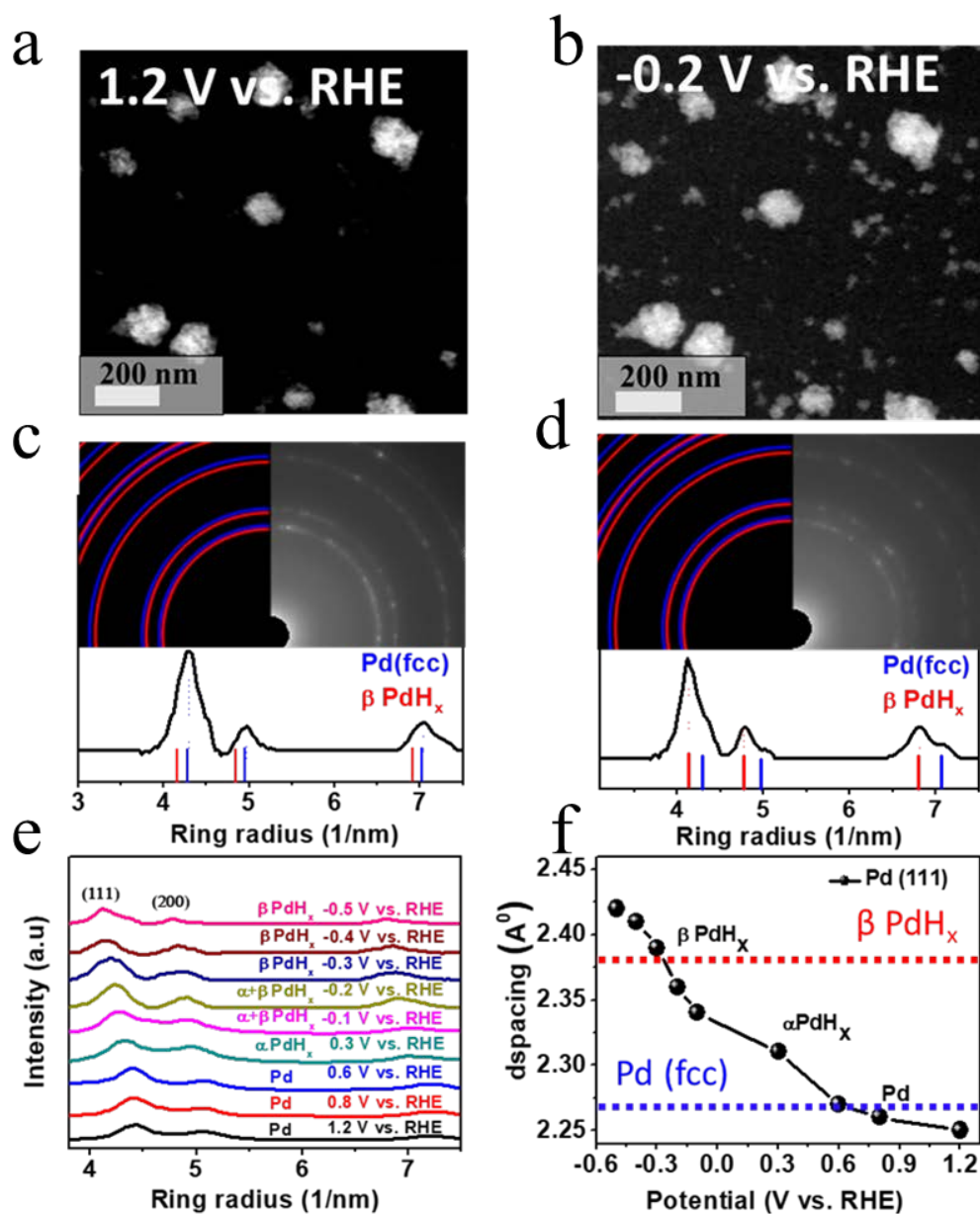
Figure 3. *In-situ* LP-HAADF-STEM imaging and SAD patterns that illustrate lattice expansion due to the phase transformation of metallic Pd to PdH_x under electrochemical CO_2 reduction conditions. **a** and **b,** *In-situ* LP-HAADF-STEM snapshots extracted from **Video S1** (Supporting information) revealing lattice expansion under applied potential (1.2 V and -0.2 V vs. RHE, respectively) in CO_2 saturated 0.1 M $KHCO_3$ electrolyte. **c** and **d,** *In-situ* LP-TEM-SAD patterns and corresponding radial intensity profiles revealing lattice expansion under applied electrode potentials of 1.2 V and -0.2 V vs RHE, respectively. **e,** Radial intensity profiles as a function of

applied electrode potential. **f,** Plot of average d-space values determined from the $Pd/PdH_x(111)$ diffraction peak fitting as a function of electrode potential, with the dashed **blue** and **red** lines representing the theoretical values for the metallic Pd and β-phase PdH_x, respectively, obtained from crystallographic information file (cif) databases. The d-space values were calculated based on the center of the electron diffraction peak using the Crystal Box software with an accuracy of ± 0.02 Å.

Morphology Changes During CO$_2$R Imaged by In-situ LP-TEM:

Under electrochemical CO_2R conditions, the morphology and behaviour of Pd particles evolve over time.[10,49] To investigate this phenomena, *in-situ* LP-(S)TEM measurements were condcuted on the PdH_x particles at -0.2 V vs. RHE (**Figure 4**, **Video S3**). At an applied potential of -0.2 V vs. RHE, some PdH_x particles were detached from the electrode surface after 5s and found to migrate to another region of the electrode (**Figure 4a**). For example, the particles in the region labelled P1 at t=5s migrated to the position labelled P2 after 16s and beyond, demonstrating that detachment and aggregation of Pd-based particles occurs under CO_2R conditions. The average PdH_x particle size was monitored in real time by *in-situ* LP-TEM (**Figure 4a and S9)** at -0.2 V vs RHE and after all *in-situ* LP-(S)TEM measurements were conducted, ex-situ TEM (**Figure 4b and S10**), HAADF-STEM (**Figure 4c and S11**), SEM (**Figure 4d**) and optical images (**Figure S12**) were conducted. Overall, an increase in Pd-based particle size from 80 ± 30 nm to 130 ± 30 nm was observed, indicating particle growth and agglomeration during electrochemical CO_2R. Additionally, the morphology of the Pd-based particles evolved into hollowed out sponge-like porous structures that are most clearly depicted in the HAADF-STEM images in **Figure S11** that provide contrast between the Pd atoms and void spaces. Post CO_2R ex-situ characterization additionally revealed that Pd/PdH_x particles detached from the electrode surface in various locations across the electrode (**Figure S10, S11, S12**). This detachment could possibly be linked to mechanical stresses arising from the phase transitions between PdH_x and Pd, which are accompanied by particle volume expansion/contraction and can induce deformation mechanisms.[50] This could also be impacted by changes to the surface chemistry of the carbon electrode under electrochemically reducing conditions, which may weaken the interactions between the Pd/PdH_x particles and the carbon electrode, rendering the particles more prone to detachment. A similar observation was previously shown for carbon supported Pt and Pd catalysts

investigated using identical location TEM.[51,52] **Figure 4e** provides a schematic depiction of the Pd/PdH$_x$ transformations and particle degradation processes observed by LP-(S)TEM imaging under CO$_2$R conditions. To confirm the changes observed in the Pd/PdH$_x$ particles were not influenced by contamination of the working electrode from the Pt-based counter electrode,[53] EDX mapping of the working electrode was conducted (**Figure S13**) and indicated the particles consisted of only pure Pd/PdH$_x$.
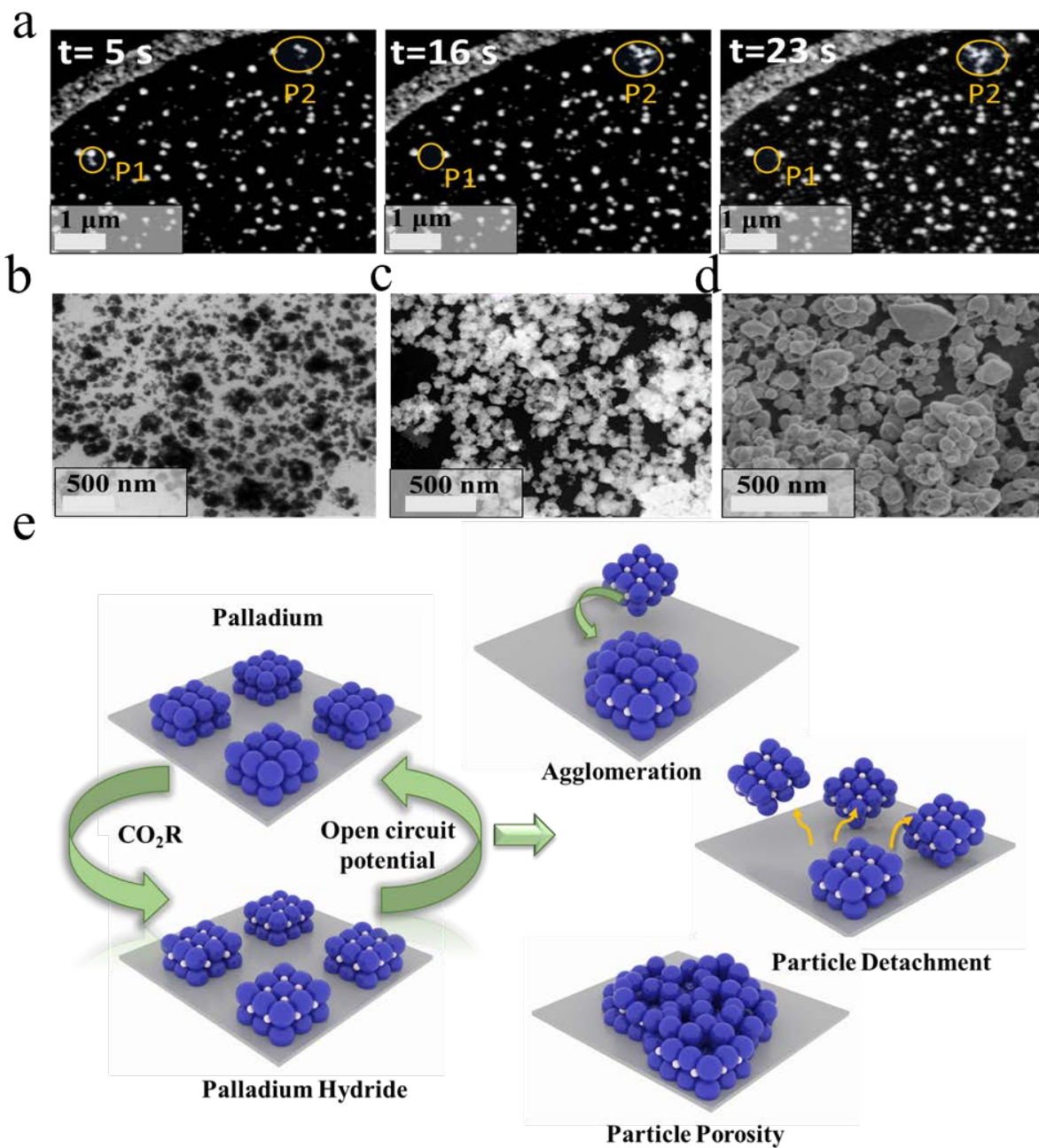
Figure 4. Morphological changes occurring in Pd/PdH$_x$ particles under electrochemical CO$_2$ conditions. **a**, *In-situ* LP-HAADF-STEM snapshots extracted from Video 3 illustrating Pd/PdH$_x$ particle migration, agglomeration, and detachment from the glassy carbon working electrode at different electrolysis times under an applied potential of -0.2 V vs. RHE (yellow circles indicate some areas where the agglomeration and detachment are more obvious). **b,** TEM **c,** HADDAF-

STEM, and **d,** SEM images of the Pd particle morphology on the *in-situ* glassy carbon electrode after in-situ imaging under CO_2 electrolysis conditions. **e,** Schematic depiction of the morphological evolution of Pd/PdH_x catalysts revealed by *in-situ* LP-TEM measurements.

Electrochemical CO_2R Activity and Selectivity:

The electrochemical CO_2R performance of Pd particles prepared by the same technique (electrodeposition) and with similar structural properties to those characterized by *in-situ* LP-(S)TEM/SAD was evaluated using large-format electrodes which enabled quantification of CO_2R activity and selectivity metrics. **Figure 5a** shows the Faradaic efficiency (selectivity) and current density (activity) of the Pd/PdH_x particles towards electrochemical CO_2R tested by 1-hour chronoamperometry measurements at electrode potentials between -0.1 to -0.5 V vs. RHE. The Pd/PdH_x particles showed the highest selectivity towards formate at -0.2 V vs RHE, with a Faradaic efficiency of 94%. At more negative applied potentials (-0.3 to -0.5 V vs. RHE), the selectivity of the Pd/PdH_x particles towards formate was reduced significantly, showing a Faradaic efficiency of only 6% at -0.5 V vs. RHE. The major products formed at this potential were H_2 (FE of 60 %) and CO (FE of 30%). Tafel plots of the partial current densities for H_2, CO and formate versus potential are shown in **Figure S14**. An increase in partial current density towards formate is observed from -0.1 to -0.2 V vs RHE, as would be expected for a reaction following Tafel behaviour. However, at potentials more negative than -0.2 V vs RHE, the partial current density towards formate plateaus and then decreases substantially, indicating catalyst surface poisoning or a shift in the electrochemical CO_2R mechanisms that results in modulated product selectivity. This dramatic shift in CO_2R selectivity coincides with the increased intercalation of protons into the PdH_x structure, with more insight into these phenomena analyzed by DFT and discussed in more detail in the proceeding sections.

Pd Surface Recovery After CO_2R:

The presence of *CO and **H species (* indicates adsorbed species) on the surface of Pd/PdH_x under CO_2R conditions has been shown to influence the activity, selectivity and structural evolution of the catalyst.[9,54,55] To investigate the presence of these species, CO_2 electrolysis was carried out on the Pd-decorated large-format electrode followed by cyclic voltammetry

15

measurements to determine the subsequent electrochemical responses of the particles. Initially, the electrodes were held for varying amounts of time at different electrochemical CO_2R relevant potentials in CO_2 saturated 0.1M $KHCO_3$. Without relaxing to open circuit potential, the electrode potential was then swept by linear sweep voltammetry up to 1.2 V vs RHE. Following this sweep, cyclic voltammetry was conducted until a steady state profile was collected, denoted as the "baseline CV" measurement. The results of these measurements are shown in **Figure 5b.** For each linear sweep voltammetry measurement that followed the chronoamperometric hold under CO_2R conditions (3 min hold at potentials from -0.1 to -0.5 V vs RHE), two oxidation peaks were observed and likely attributed to the oxidation of adsorbed surface *CO species or the desorption of H species.[56-61] As could be observed in **Figure 5b**, holding the potential at -0.1 V vs. RHE contributed to buildup of a *CO covered surface, as indicated by the oxidation peak observed at ca. 0.9 V vs RHE in the subsequent linear sweep voltammetry (inset of **Figure 5b**). The oxidation features observed at lower potentials (< 0.5 V vs RHE) are attributed to desorption of H species. When applying more negative electrode potentials during chronoamperometry, the subsequent linear sweep voltammetry measurements showed that the H desorption peaks shifted to higher potentials. This is likely due to the higher concentration of adsorbed *CO species accumulated at these more negative electrode potentials as claimed previously,[62] as well as an increased amount of H absorbed into the PdH_x lattice as demonstrated by *in-situ* LP-TEM/SAD measurements. To investigate further, the same measurements were carried out in N_2 saturated 0.1 M $KHCO_3$ to gain insights into the electrochemical response of the Pd/PdH_x particles in the absence of significant concentrations of CO_2 (and subsequent buildup of adsorbed *CO species), with results shown in **Figure S15**. After a 3-min electrolysis hold at potentials ranging from -0.1 to -0.5 V vs RHE, only one oxidation peak at ≤ 0.5 V vs RHE was observed in the subsequent linear sweep voltammetry measurement, attributed to desorption of H from PdH_x. Substantial shifts in the electrode potential of these oxidation features were not observed when more negative chronoamperometry potentials were applied, providing evidence that the shifts in the H-desorption peaks observed in the case of CO_2 saturated 0.1 M $KHCO_3$ were largely due to the presence of the adsorbed *CO species and to a lesser extent from the increased concentration of absorbed H in the PdH_x structure.

For electrochemical CO_2R measurements, an increased current density was observed at more negative electrode potentials (**Figure 5a**). Over the course of the electrolysis holds, a decrease in the current density for CO_2R was observed with time (**Figure S16**), potentially due to gradual

16

poisoning of the Pd/PdH$_x$ surface with *CO. In addition to surface poisoning by *CO, detachment and agglomeration of Pd/PdH$_x$ particles shown by in-situ (S)TEM measurements (**Figure 4**) represents another mechanism by which the active surface available for the electrochemical CO$_2$R can become diminished To gain insight into these simultaneous processes, electrochemically active surface area (ECSA) values were estimated using double layer capacitance at various stages throughout the chronoamperometry holds and subsequent linear sweep voltammetry measurements detailed in the previous paragraph. **Figure S17** and **Supplementary Note 5** in the supporting information provide more details of these measurements. The ECSA for the electrodeposited Pd/PdH$_x$ particles was calculated through double layer capacitance measurements before (ECSA$_{t=0}$) and after chronoamperometry electrolysis holds at -0.1 V vs RHE in CO$_2$-saturated 0.1 M KHCO$_3$ for durations ranging from 3 to 45 mins (ECSA$_{t=3 \text{ to } t=45}$). Following ECSA measurements, cyclic voltammetry scans from -0.1 to 1.3 V vs RHE were applied to remove adsorbed *CO species and restore the "clean" Pd surface. The cyclic voltammetry measurement immediately following the electrolysis holds are shown in **Figures 5c**, and the subsequent cyclic voltammetry measurement (2nd cycle) are shown in **Figure 5d.** It is worthwhile to note than subsequent cyclic voltammetry cycles showed negligible differences compared to the 2nd cycle, indicating the electrode had reached steady state. The first cyclic voltammetry cycle following the electrolysis hold (**Figure 5c**) showed the appearance of a *CO stripping peak between ca. 0.9 and 1.1 V vs RHE, with the magnitude of the peak increasing with increasing electrolysis hold times. This peak was not present in subsequent cyclic voltammetry measurements (Figure 5d), indicating that all adsorbed *CO species were successfully removed and a pristine Pd surface was recovered.

To track the impact of *CO* poising on the ECSA of the Pd/PdH$_x$ particles during the CO$_2$R, the ECSA$_{t=x}$/ECSA$_{t=0}$ was estimated (**Figure 5e**), where time (t) indicates the duration of the electrolysis hold at -0.1 V vs RHE. When the electrolysis period was prolonged from 3 min to 45 mins, the ECSA$_{t=x}$/ECSA$_{t=0}$ ratio was reduced from 1.01 to 0.8, demonstrating an approximately 20% loss in surface area. This reduction in the ECSA could be recovered after the subsequent cyclic voltammetry cycle to restore the pristine Pd surface, indicating the loss in ECSA following electrolysis hold likely arose due to *CO poisoning. It was then desirable to identify ECSA changes following longer electrolysis holds under CO$_2$R conditions. 1hr electrolysis holds were conducted sequentially at increasingly more negative electrode potentials, starting at -0.1 V vs RHE and

17

proceeding in increments of 100 mV down to -0.5 V vs RHE. Between each 1hr electrolysis hold, repeated cyclic voltammetry measurements were conducted to clean the Pd surface and ECSA values were measured by double layer capacitance to calculate the $ECSA/ECSA_{t=0}$ ratios shown in **Figure 5f**. The electrolyte was also replaced with fresh electrolyte to remove possible contaminants or liquid phase CO_2R products that could impact subsequent measurements before subquent electrolysis holds and electrochemical measurements were applied. The calculated $ECSA/ECSA_{t=0}$ after a 1hr electrolysis hold at -0.2 V vs RHE and cyclic voltammetry cleaning showed the highest value of 1.5. This increase was attributed to the introduction of porosity into the Pd/PdH_x particles revealed by ex-situ HAADF-STEM imaging of the electrodes after CO_2R (**Figure S11**) as discussed previously. ex-situ. At more negative electrode potential holds (electrolysis) from -0.3 to -0.5 V vs. RHE, the calculated $ECSA/ECSA_{t=0}$ decreased from 1.3 to 0.9, respectively. This subsequent decrease in ECSA is likely due to detachment of the Pd/PdH_x particles from the electrode surface, also as discussed previously*ex-situ*. Similar particle detachment morphological changes were also observed on the large-format electrodes after one hour of electrolysis at -0.5 V vs RHE (**Figures S18** and **S19**), reinforcing the fact that Pd/PdH_x particle detachment was prevalent at these conditions and responsible for the observed ECSA decrease.
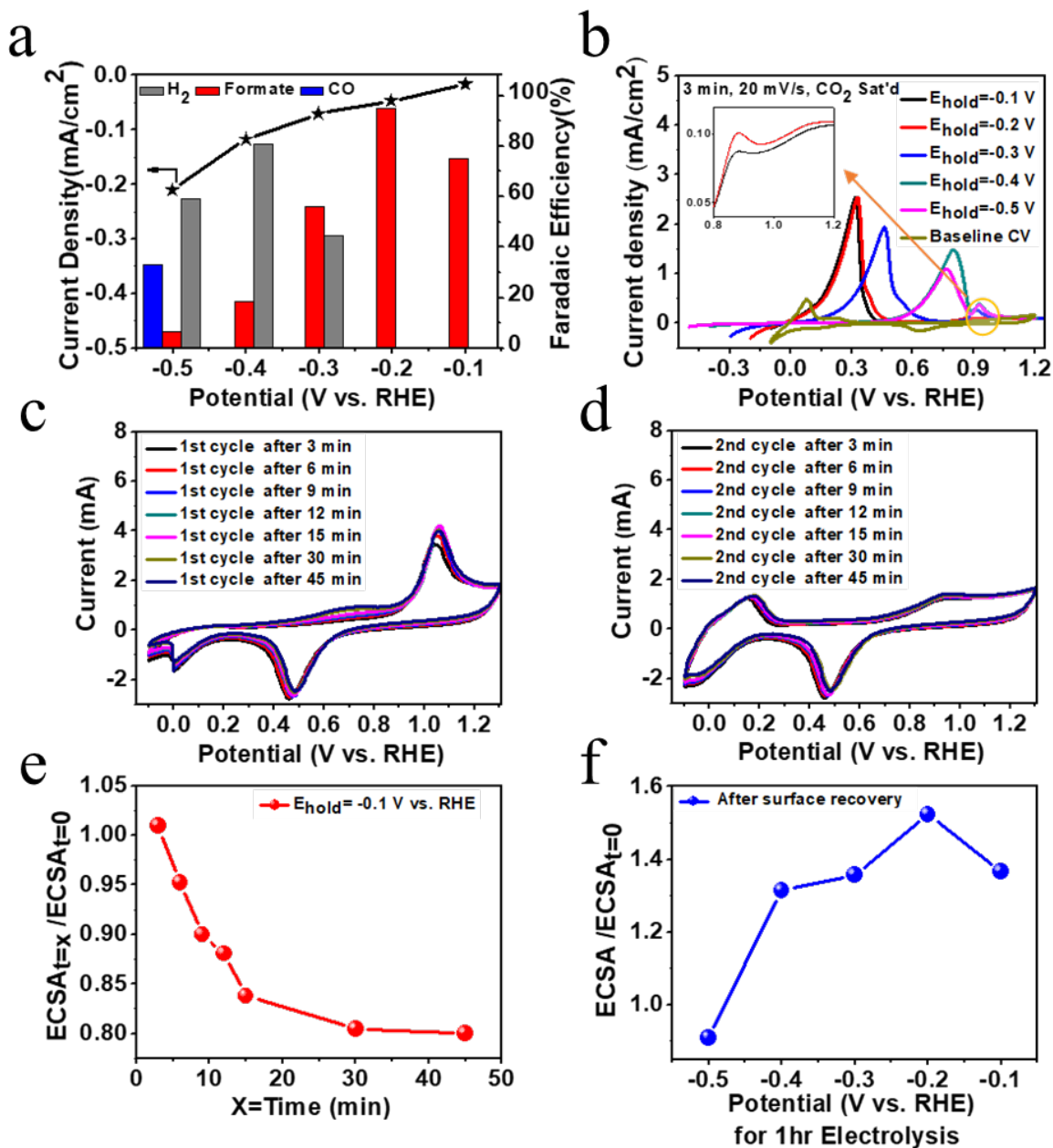
Figure 5. Electrochemical CO_2R selectivity and surface recovery of Pd particles after poisoning by adsorbed *CO species: **a,** Faradaic efficiencies (left y-axis) and partial current densities (right y-axis) for the production of formate, H_2 and CO. **b,** Positive linear sweep voltammetry following a 3min electrolysis hold at various CO_2R electrode potentials, along with baseline cyclic voltammetry curves collected in CO_2 saturated 0.1 M $KHCO_3$ electrolyte with a scan rate of 20mV/s. **c** and **d,** Cyclic voltammetry measurements including the 1st and 2nd cycle following

19

varying durations of an electrolysis hold at -0.1 V vs. RHE. **e,** ECSA estimations using electrochemical double layer capacitance measurements immediately following an electrolysis hold at -0.1 V vs RHE for varying time durations (x) normalized by the original ECSA of the catalyst particles (i.e., $ECSA_{t=x}/ECSA_{t=0}$), demonstrating the effect of *CO poisoning on the ECSA. **f,** ECSA estimations following a 1hr electrolysis hold at various electrode potentials and subsequent cyclic voltammetry sweeps to strip *CO species and recover a clean Pd surface. ECSA values are normalized by the original ECSA of the catalyst particles (i.e., $ECSA/ECSA_{t=0}$).

Mechanistic Insight into CO₂R Activity and Selectivity Through Density Functional Theory:

DFT calculations were performed to provide understanding of the structure-property-performance trends observed via *in-situ* LP-(S)TEM correlated with CO_2R activity/selectivity measurements on electro-deposited Pd/PdH_x particles. The constant potential methodology implemented in the Solvated Jellium Method (SJM)[63] was applied, enabling the simulation of adsorbed $*CO_2$, which is only possible when including explicit charging of the electrode. The (111) and (100) facets of the fully hydrogenated β-phase PdH_x were studied in accordance with the identification of this phase at potentials below -0.2 V vs RHE. Hydrogen atoms were located in the octahedral sites of bulk Pd, corresponding to hollow sites on the surface of Pd. The lattice parameters of the β-PdH_x bulk structure were optimized, leading to a 0.12 Å increase in the d-spacing compared to metallic Pd, in line with the experimental observations presented in **Figure 3f**. **Figure S20** shows the calculated adsorption free energies of H^+ from solution on a $PdH_x(111)$ surface at varying **H coverages. The calculated binding energies suggest an incomplete monolayer of **H is present at 0 V vs. RHE, with nearly thermoneutral binding energies up to a coverage of ¾ at -0.3 V vs. RHE a complete monolayer is present.

Figure 6a shows the calculated free energy pathways for electrochemical CO_2R towards formate and CO occurring on the $PdH_x(111)$ facet, while results for the $PdH_x(100)$ facet are shown in **Figure S21**. Particularly, the $PdH_x(100)$ facet is found to be poisoned with *CO adsorbates under reaction conditions and hence not active to produce CO or formate. All subsequent calculations discussed were therefore performed on the PdH_x (111) facet. The mechanism of CO_2R to produce CO was found to pass through a (bent) $*CO_2$ intermediate bound to PdH_x on a Pd top-site via the

carbon atom, as shown in the atomic scale schematic at the top of **Figure 6a**. On the other hand, the mechanism of CO_2R toward formate does not proceed through a stable $*CO_2$ intermediate. Rather, CO_2 is found to react with a surface bound hydrogen in a Heyrovsky-like mechanism[64] after being activated close to the PdH_x surface (**Figure S22**). This mechanism towards producing formate on PdH_x (and possibly other metal hydrides) is in stark contrast to proposed mechanisms of formate production on oxophilic post-transition metals (such as Pb[65] and Sn[66]) that have been proposed as capable of stabilizing CO_2 binding via the oxygen atoms ($*OCO$) followed by protonation to produce formate.[66-68] Conversely, stabilizing the $*OCO$ intermediate on PdH_x in the simulations was not successful, even upon rigorous sampling of various binding motifs. The fact that the key intermediate in formate production, $*OCO$, does not bind strongly on PdH_x suggests that the hydrogenation of the central carbon atom occurs via the weakly bound (sub-)surface hydrogen atoms. The reaction mechanism involving CO_2 hydrogenation towards producing formate was identified as an outcome of the transition state searches starting from both solvated (planar) and adsorbed (bent) CO_2. Both starting states for the reaction (i.e., solvated or adsorbed CO_2) led to the same transition state, where partially activated CO_2 reacts with a (sub)surface $*H$ ($*H-CO_2$). The potential response at the transition state was calculated to be 0.2 eV/V, while the majority of the charge injection leading to the formate occurred after the transition state (**Figure S22b**).

The formation of $*COOH$ was identified as the bottleneck towards producing CO with the formation calculated to exhibit a potential response of 1.13 eV/V **(Figure 6a).** As the energetics for forming $*COOH$ are more strongly dependent on potential that the formation of $*H-CO_2$, CO production becomes energetically favored at increasingly negative electrode potentials. At 0V vs. RHE, however, $*H-CO_2$ is 0.30 eV more stable than $*COOH$, rendering formate the preferentially formed product at this electrode potential. It should been noted that the reaction rate of $*CO_2$ to $*COOH$ is only limited by the thermodynamic barrier, as the negative partial charge on the O-end of $*CO_2$ enables facile oxygen protonation.[69] However, the appearance of a kinetic barrier for the step from $*CO_2$ to $*COOH$ would not change the qualitative behavior of a larger stabilization of the CO-path with more negative potentials. The 0.36 eV/V potential response of $*CO_2$ is still larger than the 0.2 eV/V of $*H-CO_2$, and the barrier from $*CO_2$ to $*COOH$ cannot exhibit a lower potential response than either of the end states.

Based on the described reaction energetics, a microkinetic model was constructed (**Figure 6b**). The calculated turnover frequencies (TOF) towards formate outweighs the TOF towards CO at electrode potentials between -0.2 and -0.35 V vs RHE. At more negative potentials, the TOF towards both CO and HCOO- increases, although the increase in TOF for CO is much more drastic $^-$. The selectivity for CO (TOF towards CO divided by the sum of the TOFs towards both CO and HCOO$^-$) increases as a result of the strong potential response calculated for *COOH as described above. Therefore, this analysis indicates the CO_2R selectivity towards CO should increase at more negative potentials owing to the electrode potential dependent energetics of the reaction relevant species. The results of this microkinetic modelling are in agreement with experimental CO_2R measurements that indicate a shift in selectivity from formate towards CO at increasingly negative potentials (**Figure 5a**). A quantitative agreement between experiment and theory is not always expected,[70] thus calculations were performed to understand the sensitivity the calculated microkinetic models have on the calculated free energy values of *H-CO. **Figure 6b** shows blue shaded areas that represent the variation in TOF and selectivity that would be expected with a difference in the calculated *H-CO free energy of ±0.1eV. This range in the energetic uncertainty leads to a ca. 0.2 V difference in the electrode potential at which a CO_2R selectivity change from producing HCOO- to producing CO would be expected. However, as discussed above, this uncertainty does not alter the qualitative finding that PdH_x produces formate almost exclusively at low overpotentials, followed by a sharp change in selectivity towards CO production at more negative potentials.

Discussion

The morphological and phase structure conversions occurring in Pd/PdH_x catalyst under electrochemical CO_2R conditions was revealed by *in-situ* LP-(S)TEM characterization and supplemented by *ex-situ* post-CO_2R characterization of the electrodes. As shown in **Figure 4e**, three primary changes to the Pd/PdH_x were observed under CO_2R conditions: (1) Particle agglomeration; (2) Particle detachment from the electrode surface; and (3) Hollowing out of the particles to form a sponge-like porous morphology.

To an extent, the particle agglomeration observed could follow Ostwald ripening or other sintering mechanisms. Localized *in-situ* particle tracking measurements could be applied to understand this process of particle sintering as well as the underlying kinetics,[9] which is outside the scope of the

present work. The particle agglomeration observed in the *in-situ* LP-(S)TEM measurements was found to occur by particle detachment from the electrode surface and subsequent deposition on another region of the electrode (**Figure 4a**) that was most prevalent at more negative electrochemical CO_2R conditions. It is speculated that particle detachment was largely induced by mechanical forces that arose due to the absorption of increased amounts of H into the PdH_x lattice at increasingly negative electrode potentials, which led to significant volume expansion (and contraction upon conversion back to metallic Pd). This could lead to mechanical instabilities at the catalyst/electrode interface, causing the detachment of catalyst particles.[50] It should also be noted that mechanical agitation from the formation of bubbles (H_2 and/or CO) at increasingly negative potentials could also influence particle detachment; however, there was no direct observation of this by *in-situ* LP-(S)TEM measurements.

The hollowing of Pd/PdH_x to form porous sponge-like particles also occurred under CO_2R conditions, likely due to thermodynamic driving forces.[71] Additionally, the evolution of porosity through morphological changes could arise due to adsorbate (i.e., *CO) induced restructuring.[72,73] The presence of *CO species on the surface of Pd/PdH_x under CO_2R conditions was demonstrated in this work (**Figure 5b**), with DFT calculations suggested *CO poisoning to be a facet dependent occurrence on Pd/PdH_x.

The phase structure of Pd/PdH_x was observed as a function of electrode potential under CO_2R conditions by *in-situ* LP-TEM/SAD. At potentials between -0.1 and -0.2 V vs RHE, the particles were in a mixed α/β-phase PdH_x, with complete formation of the β-PdH_x phase observed at more negative potentials. Interestingly, this conversion of mixed phase α/β-PdH_x to β-phase PdH_x coincided with a CO_2R selectivity shift from formate (at lower overpotentials) towards CO (at higher overpotentials), suggesting that the phase transformation may be underlying the catalytic trends. However, DFT calculations coupled with micro-kinetic modelling indicated the primary reason for the CO_2R selectivity change was due to the electrode potential dependent thermodynamic energetics of adsorbed reactive intermediate — *COOH in the case of CO or *H-CO_2 in the case of formate. For the production of formate, the hydrogenation of the C atom in CO_2 by (sub)surface *H was identified as a key step, in contrast to the formate production mechanism suggested previously for oxo-philic metals such as Sn and Bi, whereby the CO_2 molecules were found to adsorb on the catalyst surface via the O atoms.[66-68] Previous calculations also suggested

that Pd catalysts can produce formate through the mechanism where CO_2 is adsorbed via the O-atom, but this configuration was not found to be energetically possible on β-PdH_x. Formate production through the reaction of CO_2 with *H has been suggested in the past,[9] but has not been rigorously explored through the combination of *in-situ* catalyst characterization alongside DFT and micro-kinetic modelling. A The direct participation of (sub)surface *H in CO_2R towards formate suggests that PdH_x catalysts with a increased *H availability as a reactant (and a reduction in the binding strength of *H) is a desirable catalyst design principle . However, at -0.2 V vs RHE where the highest selectivity towards formate is observed, the catalyst is in a mixed α/βPdH_x phase. At lower electrode potentials complete conversion to the β-PdH_x phase and increased saturation of the lattice with hydrogen does not coincide with an increase in activity/selectivity towards formate. Instead, the opposite trend is observed. and DFT alongside micro-kinetic calculations show that at more negative electrode potentials, the formation of *COOH intermediate (for producing *CO) becomes energetically more favourable than the formation of the *H-CO_2 intermediate for producing formate. Therefore, the selectivity change of the CO_2R from producing formate toward CO at more negative electrode potentials is attributed to thermodynamic changes to the energetics of the reaction and not due to the phase transformation of increased content of absorbed H in the PdH_x structures present under reaction conditions.
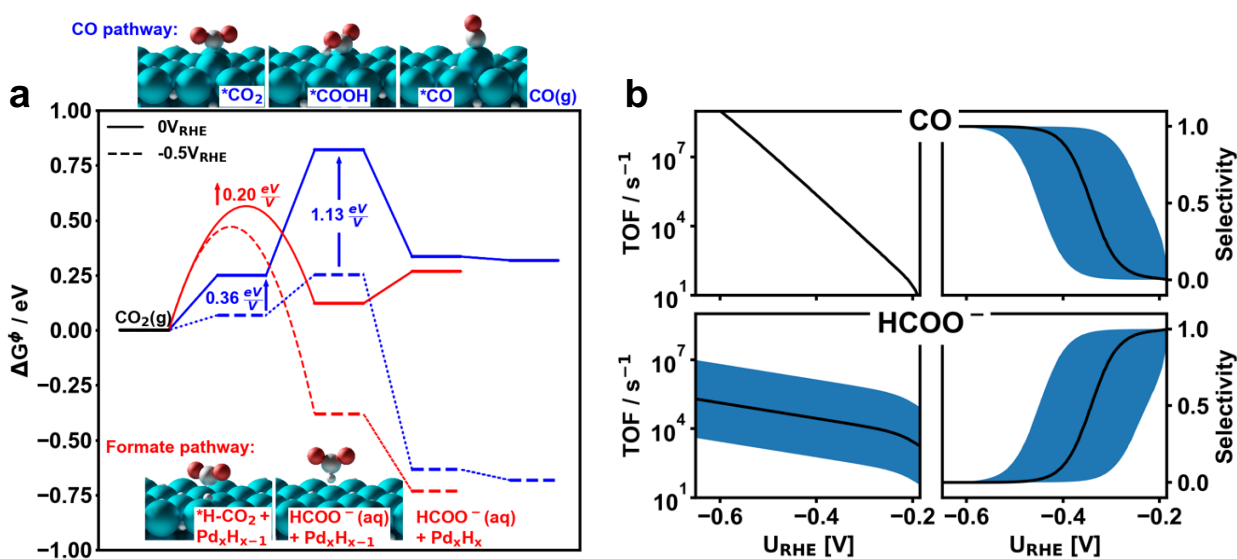
Figure 6. Density functional theory and micro-kinetic modelling analyses. **a,** Calculated DFT (constant potential) free energy diagram of the reaction pathways for CO_2R towards formate and CO, including the calculated reaction barrier of CO_2 hydrogenation (*$H-CO_2$) plotted at 0 and -0.5 V vs. RHE (solid lines and dashed lines, respectively). The optimized geometries of the associated reaction steps are shown explicitly next to the labels. **b,** Turnover frequency and selectivity results obtained from micro-kinetic modelling using the results from DFT analyses as inputs. The shaded blue region indicates the uncertainty in TOF and selectivity calculations that arise if the barrier for CO_2 surface hydrogenation varies by +/- 0.1eV.

Conclusion:

In-situ LP-(S)TEM and SAD measurements were conducted on electro-deposited Pd/PdH_x catalysts for the electrochemical CO_2R to identify morphological and phase structure changes. Under electrochemical CO2R conditions, the Pd/PdH_x catalysts underwent morphological changes, including: (i) particle agglomeration; and (ii) formation of a porous sponge-like morphology likely arising from adsorbate (i.e., *CO) induced restructuring. Additionally, particle detachment from the electrode surface was observed, likely due to mechanical agitation induced by the process of interconversion between the metallic Pd and PdH_x phase(s). Electrochemical CO_2R activity and selectivity measurements revealed that formate was produced almost exclusively at -0.2 V vs RHE, whereby the production of H2 and CO became prominent at more negative potentials. Correlation with LP-TEM-SAD measurements showed this selectivity shift coincided with increased H absorption into the PdH_x, forming a β-PdH_x phase. By coupling *in-situ* structural analysis and electrochemical evaluation of the Pd/PdH_x catalysts with DFT calculations and micro-kinetic modelling, it was demonstrated the CO_2R selectivity from formate to CO/H_2 changes occurred due to potential-dependent reaction energetic changes and not due to the observed PdH_x lattice expansion. DFT calculations on revealed the reaction mechanism towards formate on β-PdH_x involved hydrogenation of the C atom in the CO_2 molecule by (sub)surface *H present in PdH_x. This contrasts the formate production mechanism suggested previously for oxo-philic metals where the CO_2 molecule adsorbs on the catalyst surface via the oxygen atom and is subsequently protonated. At more negative electrode potentials, the *COOH intermediate for producing CO was stabilized in comparison to the *$H-CO_2$ intermediate for

25

producing formate, explaining the dramatic shift in selectivity from nearly-exclusive production of formate at -0.2 V vs RHE to the production of CO/H_2 at -0.5 V vs RHE. This work therefore provides mechanistic insight into the electro-catalytic mechanisms of CO_2R occurring on Pd-based catalysts that can be applied to understand and guide future catalyst designs. Furthermore *in-situ* LP-(S)TEM including SAD has been demonstrated as a powerful technique for gaining unprecedented insight into the morphological and phase structure changes occurring in catalysts under electrochemical CO_2R conditions.

Materials and Methods:

Materials:

Potassium bicarbonate (ACS reagent, 99.7%), palladium (II) chloride (99.9%), and hydrochloric acid (ACS reagent, 37%), were purchased from Sigma Aldrich and used without any further purification.

Methods:

Pd particle electrodeposition using *in-situ* LP-TEM electrochemical reactor:

The electrochemical setup for Pd electrodeposition onto the *in-situ* electrochemical TEM sample holder is shown in **Figure S1**. The Poseidon Select (Protochips) *in-situ* TEM sample holder was utilized, whereby the micro-chip electrochemical cell mounted in the tip of the TEM holder consists of a Pt reference and counter electrode, and a glassy carbon working electrode (**Figure S1**). The micro-chip reactor consists of a top and bottom chip that are sealed together with a gasket and fastened with screws. Both the bottom and top chips contain a thin silicon nitride (SiN_x) membrane viewing window that enables electron transmission for *in-situ* TEM measurements. As received, both the top and bottom chips are coated with a protective photoresist layer to prevent SiN_x membrane damage. The protective photoresist layer was removed prior to the two-step rinse process, whereby chips were submerged first in acetone and then methanol, each for 2 minutes. To enhance the hydrophilicity of the chips, a plasma cleaning (Gatan plasma system model 950 advanced plasma, with $Ne/H_2/Ar$ gas mixture and operating at 15 W) was used. The process was performed for 2 minutes for the small E-chip and 30 seconds or less for the large E-chip as the excessive plasma cleaning could damage the glassy carbon electrode. Following assembly of the

micro-chip electrochemical cell, a liquid solution of 5 mM $H_2 PdCl_4$ with 0.015 M HCl was introduced at a flow rate of 5 µL/min through the microfluidic channels of the sample Poseidon Select holder using an external syringe pump. Once the solution was introduced, electrochemical chronoamperometry was carried out at 0.2 V vs. RHE using a floating potentiostat (Gamry Reference 600+) for 120 seconds to ensure the electrodeposition of a sufficient amount of Pd particles on the working electrode. Following electrodeposition, the *in-situ* TEM holder was purged with Millipore water to remove the electrodeposition solution.

In-situ (S)TEM measurements under electrochemical CO_2R conditions:

In-situ electrochemical (S)TEM liquid cell measurements were conducted to investigate the phase and structural transformations of electrodeposited Pd particle catalysts under CO_2R conditions. For all *in-situ* TEM experiments, to avoid SiN_x window bulging due to the pressure difference between the electrochemical micro-chip cell and the vacuum in the TEM column, a perpendicular (crossed configuration) window strategy was utilized as recommended by previous studies.[74] After electrodeposition of Pd and purging of the Pd salt solution by Millipore water, the Millipore water was replaced by flushing the electrochemical cell TEM holder with freshly prepared CO_2 saturated 0.1 M $KHCO_3$ solution at a flow rate of 5 µL/min. Confirmation that the 0.1 M $KHCO_3$ had entered the sample holder was indicated when the open circuit potential was stabilized. Leak checking of the *in-situ* TEM sample holder was performed before insertion into the microscope using a custom-designed vacuum pump station. To establish a baseline, *in-situ* LP-TEM imaging and select area electron diffraction (*in-situ* LP-TEM/SAD) measurements were performed at different times: 1, 5,7, and 10 minutes before applying any electrode potential. After these measurements, chronoamperometry at different applied potentials in the range of 1.3 to -0.2 V vs. RHE was applied for 60 seconds at each potential, during which time *in-situ* LP TEM imaging and *in-situ* LP-TEM/SAD patterns were collected. Between each chronoamperometry experiment, a potential of 1.2 V vs. RHE was applied for 60 sec to recondition the particles to be in metallic Pd form, thereby avoiding any issues pertaining to Pd/PdH_x transformation hysteresis.[75] Detailed information about *in-situ* LP-TEM/SAD analysis and beam dose calculations are included in the Supporting Information.

Pd electrodeposition on large-format glassy carbon electrodes for CO_2R:

Electrodes to test the electrochemical CO_2R activity and selectivity of electro-deposited Pd were prepared using a large-format glassy carbon electrode with dimensions of 2cm by 5cm. Electrodeposition of Pd particles was performed by chronoamperometry at 0.2 V vs. RHE for 120 seconds in 5 mM H_2PdCl_4 mixed with 0.015 M HCl. A Pt foil counter electrode and Ag/AgCl reference electrode that was calibrated and converted to the RHE scale were used. After electrodeposition, the electrode was rinsed carefully with Millipore water and dried at room temperature under N_2 gas flow.

Electrochemical CO_2R activity/selectivity measurements:

Electrochemical CO_2R activity and selectivity of the electrodeposited Pd catalyst were investigated using a custom-built electrochemical cell (**Figure S2**) reported on previously,[76] which was designed and improved upon to provide high sensitivity for CO_2R product detection and quantification. On-line gas chromatography (SRI Multigas #5) was used to detect/quantify gas products while liquid products were quantified using the Bruker AVIII 700 NMR available at McMaster University's Nuclear Magnetic Resonance Facility. A mass flow control unit (pMFC, MKS Instrument) was used to maintain a CO_2 flow rate of 20 sccm through the catholyte chamber throughout the entire course of the reaction. A Pt foil was used as the counter electrode and Ag/AgCl as the reference electrode, which was calibrated and converted to the RHE scale by measuring the open circuit potential of the Ag/AgCl versus an in-house designed RHE. CO_2R electrolysis measurements were conducted by chronoamperometry at a potential between -0.1 V to -0.5 V vs. RHE for one hour each, while cyclic voltammetry measurements were conducted at 50mV/s before and after chronoamperometry. The geometric surface area of the large format electrode exposed to the electrolyte was 5.6 cm^2.

Materials Characterization:

To investigate the morphology and composition of Pd electrocatalysts immediately after electrodeposition and after CO_2R testing, optical microscopy (CLEMEX, Axioplan 2 imaging), scanning electron microscopy (JEOL JSM-7000F SEM), high-resolution transmission electron microscopy (HRTEM), high-angle annular dark-field scanning transmission electron microscopy (HAADF-STEM) imaging, along with energy dispersive X-ray (EDX) mapping were carried out. All TEM and HAADF-STEM imaging were performed using an image-corrected FEI Titan 80-

300LB operating at 300kV and a Thermo Scientific Talos 200X operate at 200kV available at the Canada Center for Electron Microscopy (CCEM) at McMaster University.

Computational details:

The reported DFT-based (constant potential) energies were calculated using the constant-potential mode of SJM [63] implemented in GPAW [77,78]. A real-space grid basis set was applied with a grid-spacing of 0.18 Å. The BEEF-vdW functional[79] was applied for approximating the XC contributions. All slab calculations were conducted with periodic boundary conditions parallel to the slab surface and a dipole correction in the-direction perpendicular to the surface was applied. 3x4x4 supercells were used, with the bottom two layer being constrained to the bulk lattice constants of Pt and PtH, respectively. Monkhorst−Pack k-point grids of 4 x 4 x 1 and 4 x 3 x 1 were applied for palladium and palladium hydride structures, respectively. The setup used a Fermi smearing of 0.1 eV / k_B. Forces were converged to 0.03 eV / Å and 0.05 eV / Å for stable intermediates and transition states, respectively.

SJM uses an effective potential cavity solvation model implemented into GPAW by Held and Walter [80]. The parameters used were: Bondi's van der Waals radii [81],Strength of the repulsion at the atomic radii controlling the cavity size, u0= 0.18eV, surface tension 0.001148 Pa*m (Both taken from [80], (maximal) dielectric constant (ϵ)=78.36 and temperature=298.15K. The tolerance for the electrode potential deviation from the target potential was set to 10mV.

All possible adsorbate binding configurations were sampled using the CatKit Surface module[82]. For the palladium hydride structures, hydrogens were placed in all the octahedral holes of a palladium bulk structure, corresponding to a 1:1 Pd:H ratio, resembling a β-PdH structure. The most stable structures were determined with a d-spacing of 2.42 and 2.09 for the 111 and 100 facets, respectively. Activation energies were calculated using the Climbing Image Nudge Elastic Band (CI-NEB) method[83] within the dynamic NEB (DyNEB) implementation[84]. Electronic energies are converted into free energies via a vibrational analysis within the harmonic approximation for adsorbates and an ideal gas approximation for gas phase species, as implemented in the Atomic Simulation environment (ASE) [75]

The free energy of $HCOO^-_{(aq)}$ was calculated from its equilibrium with HCOOH at the pK_a (3.75), following the relationship $G_{HCOO^-_{aq}} = G_{HCOOH_{(aq)}} - \ln(10)k_B T(pH - pK_a)$.[85] A partial pressure of 5728.86Pa was applied for the calculation of $G_{HCOOH_{(aq)}}$ from its equilibrium with $G_{HCOOH_{(g)}}$.

A free energy correction of +0.33eV was added for all molecules including an OCO-backbone, i.e. $CO_{2(g)}$, $*H\text{-}CO_2$, $*COOH$, $HCOO^-$ in order to correct systematic errors of DFT when applying the BEEF-vdW XC functional.[86,87]

Noted that, while in the transition state search of $*H\text{-}CO_2$, the unit cell explicitly contained CO_2 and $HCOO^-$ hovering in the implicit solvent above the electrode surface. However, **in Figure 6**, the states $CO_{2(g)}$ and $HCOO^-_{(aq)}$ represent the species in gas phase and bulk solution, respectively.

Data availability

The data that support the experimental findings of this study are available from the corresponding author upon request. The theoretical data and analysis routines will be made publicly available on https://github.com/CatTheoryDTU upon acceptance of the article.

Acknowledgements

References:

1   Benck, J. D., Jackson, A., Young, D., Rettenwander, D. & Chiang, Y.-M. Producing high concentrations of hydrogen in palladium via electrochemical insertion from aqueous and solid electrolytes. *Chemistry of Materials* **31**, 4234-4245 (2019).

2   Xia, R., Zhang, S., Ma, X. & Jiao, F. Surface-functionalized palladium catalysts for electrochemical CO 2 reduction. *Journal of Materials Chemistry A* **8**, 15884-15890 (2020).

3   Clark, E. L., Hahn, C., Jaramillo, T. F. & Bell, A. T. Electrochemical CO2 reduction over compressively strained CuAg surface alloys with enhanced multi-carbon oxygenate selectivity. *Journal of the American Chemical Society* **139**, 15848-15857 (2017).

4   Wang, L. *et al.* Selective reduction of CO to acetaldehyde with CuAg electrocatalysts. *Proceedings of the National Academy of Sciences* **117**, 12572-12575 (2020).

5   Li, F. *et al.* Molecular tuning of CO2-to-ethylene conversion. *Nature* **577**, 509-513 (2020).

6   Hahn, C. *et al.* Engineering Cu surfaces for the electrocatalytic conversion of CO2: Controlling selectivity toward oxygenates and hydrocarbons. *Proceedings of the National Academy of Sciences* **114**, 5918-5923 (2017).

7   Li, F. *et al.* Interplay of electrochemical and electrical effects induces structural transformations in electrocatalysts. *Nature Catalysis* **4**, 479-487 (2021).

8   Klinkova, A. *et al.* Rational design of efficient palladium catalysts for electroreduction of carbon dioxide to formate. *Acs Catalysis* **6**, 8115-8120 (2016).

9   Min, X. & Kanan, M. W. Pd-catalyzed electrohydrogenation of carbon dioxide to formate: high mass activity at low overpotential and identification of the deactivation pathway. *Journal of the American Chemical Society* **137**, 4701-4708 (2015).

10   Gao, D. *et al.* Switchable CO2 electroreduction via engineering active phases of Pd nanoparticles. *Nano Research* **10**, 2181-2191 (2017).

11   Gao, D. *et al.* Switchable CO 2 electroreduction via engineering active phases of Pd nanoparticles. *Nano Research* **10**, 2181-2191 (2017).

12   Bugaev, A. L. *et al.* In situ formation of hydrides and carbides in palladium catalyst: when XANES is better than EXAFS and XRD. *Catalysis Today* **283**, 119-126 (2017).

13   Kishore, S., Nelson, J., Adair, J. H. & Eklund, P. Hydrogen storage in spherical and platelet palladium nanoparticles. *Journal of Alloys and Compounds* **389**, 234-242 (2005).

14   Langhammer, C., Zhdanov, V. P., Zorić, I. & Kasemo, B. Size-dependent hysteresis in the formation and decomposition of hydride in metal nanoparticles. *Chemical Physics Letters* **488**, 62-66 (2010).

15   Jobic, H. & Renouprez, A. Formation of hydrides in small particles of palladium supported in Y-zeolite. *Journal of the Less Common Metals* **129**, 311-316 (1987).

16   Berube, V., Radtke, G., Dresselhaus, M. & Chen, G. Size effects on the hydrogen storage properties of nanostructured metal hydrides: a review. *International Journal of Energy Research* **31**, 637-663 (2007).

17   Johansson, M. *et al.* Hydrogen adsorption on palladium and palladium hydride at 1 bar. *Surface science* **604**, 718-729 (2010).

18   Griessen, R., Strohfeldt, N. & Giessen, H. Thermodynamics of the hybrid interaction of hydrogen with palladium nanoparticles. *Nature materials* **15**, 311 (2016).

19   McCaulley, J. A. In-situ X-ray absorption spectroscopy studies of hydride and carbide formation in supported palladium catalysts. *The Journal of Physical Chemistry* **97**, 10372-10379 (1993).

20   Shegai, T. & Langhammer, C. Hydride Formation in Single Palladium and Magnesium Nanoparticles Studied By Nanoplasmonic Dark-Field Scattering Spectroscopy. *Advanced Materials* **23**, 4409-4414 (2011).

21   Nag, N. K. A study on the formation of palladium hydride in a carbon-supported palladium catalyst. *The Journal of Physical Chemistry B* **105**, 5945-5949 (2001).

22   Syrenova, S. *et al.* Hydride formation thermodynamics and hysteresis in individual Pd nanocrystals with different size and shape. *Nature materials* **14**, 1236 (2015).

23   Bauer, M. *et al.* Structure–activity studies on highly active palladium hydrogenation catalysts by X-ray absorption spectroscopy. *The Journal of Physical Chemistry C* **116**, 22375-22385 (2012).

24   Soldatov, A., Della Longa, S. & Bianconi, A. Relevant role of hydrogen atoms in the XANES of Pd hydride: Evidence of hydrogen induced unoccupied states. *Solid state communications* **85**, 863-868 (1993).

25   Wadell, C. *et al.* Thermodynamics of hydride formation and decomposition in supported sub-10 nm Pd nanoparticles of different sizes. *Chemical Physics Letters* **603**, 75-81 (2014).

26   Langhammer, C., Larsson, E. M., Kasemo, B. & Zoric, I. Indirect nanoplasmonic sensing: ultrasensitive experimental platform for nanomaterials science and optical nanocalorimetry. *Nano letters* **10**, 3529-3538 (2010).

27   Tew, M. W., Nachtegaal, M., Janousch, M., Huthwelker, T. & van Bokhoven, J. A. The irreversible formation of palladium carbide during hydrogenation of 1-pentyne over silica-supported palladium nanoparticles: In situ Pd K and L 3 edge XAS. *Physical Chemistry Chemical Physics* **14**, 5761-5768 (2012).

28   Teschner, D. *et al.* Role of hydrogen species in palladium-catalyzed alkyne hydrogenation. *The Journal of Physical Chemistry C* **114**, 2293-2299 (2010).

29   Teschner, D. *et al.* The roles of subsurface carbon and hydrogen in palladium-catalyzed alkyne hydrogenation. *Science* **320**, 86-89 (2008).

30   Wang, X. *et al.* Morphology and mechanism of highly selective Cu (II) oxide nanosheet catalysts for carbon dioxide electroreduction. *Nature communications* **12**, 1-12 (2021).

31   Arán-Ais, R. M. *et al.* Imaging electrochemically synthesized Cu2O cubes and their morphological evolution under conditions relevant to CO2 electroreduction. *Nature communications* **11**, 1-8 (2020).

32   Schirber, J. & Morosin, B. Lattice constants of β− P d H x and β− P d D x with x near 1.0. *Physical Review B* **12**, 117 (1975).

33   Lewis, N. S. *et al.* Searches for low-temperature nuclear fusion of deuterium in palladium. *Nature* **340**, 525 (1989).

34   Felici, R., Bertalot, L., DeNinno, A., LaBarbera, A. & Violante, V. In situ measurement of the deuterium (hydrogen) charging of a palladium electrode during electrolysis by energy dispersive x-ray diffraction. *Review of scientific instruments* **66**, 3344-3348 (1995).

35   Fukada, Y., Hioki, T. & Motohiro, T. Multiple phase separation of super-abundant-vacancies in Pd hydrides by all solid-state electrolysis in moderate temperatures around 300° C. *Journal of Alloys and Compounds* **688**, 404-412 (2016).

36   Knies, D. *et al.* In-situ synchrotron energy-dispersive x-ray diffraction study of thin Pd foils with Pd: D and Pd: H concentrations up to 1: 1. *Journal of Applied Physics* **112**, 083510 (2012).

37   Fukada, Y., Hioki, T., Motohiro, T. & Ohshima, S. In situ x-ray diffraction study of crystal structure of Pd during hydrogen isotope loading by solid-state electrolysis at moderate temperatures 250–300° C. *Journal of Alloys and Compounds* **647**, 221-230 (2015).

38   Rahaman, M., Dutta, A. & Broekmann, P. Size-Dependent Activity of Palladium Nanoparticles: Efficient Conversion of CO2 into Formate at Low Overpotentials. *ChemSusChem* **10**, 1733-1741 (2017).

39 Landers, A. T. *et al.* Dynamics and Hysteresis of Hydrogen Intercalation and Deintercalation in Palladium Electrodes: A Multimodal In Situ X-ray Diffraction, Coulometry, and Computational Study. *Chemistry of Materials* **33**, 5872-5884 (2021).

40 Yuan, Y., Amine, K., Lu, J. & Shahbazian-Yassar, R. Understanding materials challenges for rechargeable ion batteries with in situ transmission electron microscopy. *Nature communications* **8**, 1-14 (2017).

41 Handoko, A. D., Wei, F., Yeo, B. S. & Seh, Z. W. Understanding heterogeneous electrocatalytic carbon dioxide reduction through operando techniques. *Nature Catalysis* **1**, 922-934 (2018).

42 Yang, J. *et al.* Liquid cell transmission electron microscopy sheds light on the mechanism of palladium electrodeposition. *Langmuir* **35**, 862-869 (2019).

43 Yang, J., Prabhudev, S., Andrei, C. M., Botton, G. A. & Soleymani, L. Deposition and morphological evolution of nanostructured palladium during potential cycling: a liquid-cell TEM study. *Chemical Communications* **55**, 9204-9207 (2019).

44 Baldi, A., Narayan, T. C., Koh, A. L. & Dionne, J. A. In situ detection of hydrogen-induced phase transitions in individual palladium nanocrystals. *Nature materials* **13**, 1143-1148 (2014).

45 Hong, J. *et al.* Metastable hexagonal close-packed palladium hydride in liquid cell TEM. *Nature* **603**, 631-636 (2022).

46 Wang, X. *et al.* Morphology and mechanism of highly selective Cu (II) oxide nanosheet catalysts for carbon dioxide electroreduction. *Nature communications* **12**, 1-12 (2021).

47 Beermann, V. *et al.* Real-time imaging of activation and degradation of carbon supported octahedral Pt–Ni alloy fuel cell catalysts at the nanoscale using in situ electrochemical liquid cell STEM. *Energy & Environmental Science* **12**, 2476-2485 (2019).

48 Klinger, M. & Jäger, A. Crystallographic Tool Box (CrysTBox): automated tools for transmission electron microscopists and crystallographers. *Journal of applied crystallography* **48**, 2012-2018 (2015).

49 Zhu, W., Kattel, S., Jiao, F. & Chen, J. G. Shape-controlled CO2 electrochemical reduction on nanosized Pd hydride cubes and octahedra. *Advanced Energy Materials* **9**, 1802840 (2019).

50 Bian, J., Yang, L., Yuan, W. & Wang, G. Influence of hydrogenation on the mechanical properties of Pd nanoparticles. *RSC advances* **11**, 3115-3124 (2021).

51 Zadick, A., Dubau, L., Sergent, N., Berthome, G. & Chatenet, M. Huge instability of Pt/C catalysts in alkaline medium. *Acs Catalysis* **5**, 4819-4824 (2015).

52 Zadick, A., Dubau, L., Demirci, U. B. & Chatenet, M. Effects of Pd nanoparticle size and solution reducer strength on Pd/C electrocatalyst stability in alkaline electrolyte. *Journal of The Electrochemical Society* **163**, F781 (2016).

53 Clark, E. L. *et al.* Standards and protocols for data acquisition and reporting for studies of the electrochemical reduction of carbon dioxide. *Acs Catalysis* **8**, 6560-6570 (2018).

54 Chen, X., Granda-Marulanda, L. P., McCrum, I. T. & Koper, M. How palladium inhibits CO poisoning during electrocatalytic formic acid oxidation and carbon dioxide reduction. *Nature communications* **13**, 1-11 (2022).

55 Guo, R.-H. & Hu, C.-C. The Relationships among Hydrogen Adsorption, CO Stripping, and Selectivity of CO2 Reduction on Pd Nanoparticles. *Journal of The Electrochemical Society* **168**, 054507 (2021).

56 Kolbe, D. & Vielstich, W. Adsorbate formation during the electrochemical reduction of carbon dioxide at palladium—A DEMS study. *Electrochimica acta* **41**, 2457-2460 (1996).

57 Hoshi, N., Noma, M., Suzuki, T. & Hori, Y. Structural effect on the rate of CO2 reduction on single crystal electrodes of palladium. *Journal of Electroanalytical Chemistry* **421**, 15-18 (1997).

58   Pérez-Rodríguez, S., Rillo, N., Lázaro, M. & Pastor, E. Pd catalysts supported onto nanostructured carbon materials for CO2 valorization by electrochemical reduction. *Applied Catalysis B: Environmental* **163**, 83-95 (2015).

59   Valenti, M. *et al.* Suppressing H2 evolution and promoting selective CO2 electroreduction to CO at low overpotentials by alloying Au with Pd. *ACS Catalysis* **9**, 3527-3536 (2019).

60   Grdeń, M., Paruszewska, A. & Czerwiński, A. Electrosorption of carbon dioxide on Pd☐ Pt alloys. *Journal of Electroanalytical Chemistry* **502**, 91-99 (2001).

61   Diercks, J. S. *et al.* Interplay between Surface-Adsorbed CO and Bulk Pd Hydride under CO2-Electroreduction Conditions. *ACS Catalysis* **12**, 10727-10741 (2022).

62   Diercks, J. S. *et al.* Interplay between Surface-Adsorbed CO and Bulk Pd Hydride under CO2-Electroreduction Conditions. *ACS Catalysis* **12**, 10727-10741 (2022).

63   Kastlunger, G., Lindgren, P. & Peterson, A. A. Controlled-potential simulation of elementary electrochemical reactions: proton discharge on metal surfaces. *The Journal of Physical Chemistry C* **122**, 12771-12781 (2018).

64   Santos, E., Hindelang, P., Quaino, P. & Schmickler, W. A model for the Heyrovsky reaction as the second step in hydrogen evolution. *Physical Chemistry Chemical Physics* **13**, 6992-7000 (2011).

65   Yoo, J. S., Christensen, R., Vegge, T., Nørskov, J. K. & Studt, F. Theoretical insight into the trends that guide the electrochemical reduction of carbon dioxide to formic acid. *ChemSusChem* **9**, 358-363 (2016).

66   Feaster, J. T. *et al.* Understanding selectivity for the electrochemical reduction of carbon dioxide to formic acid and carbon monoxide on metal electrodes. *Acs Catalysis* **7**, 4822-4827 (2017).

67   Sun, Z., Ma, T., Tao, H., Fan, Q. & Han, B. Fundamentals and challenges of electrochemical CO2 reduction using two-dimensional materials. *Chem* **3**, 560-587 (2017).

68   Zhao, S. *et al.* Advances in Sn-based catalysts for electrochemical CO2 reduction. *Nano-Micro Letters* **11**, 1-19 (2019).

69   Vijay, S. *et al.* Unified mechanistic understanding of CO2 reduction to CO on transition metal and single atom catalysts. *Nature Catalysis* **4**, 1024-1031 (2021).

70   Govindarajan, N., Kastlunger, G., Heenen, H. H. & Chan, K. Improving the intrinsic activity of electrocatalysts for sustainable energy conversion: where are we and where can we go? *Chemical Science* **13**, 14-26 (2022).

71   Huang, J. *et al.* Potential-induced nanoclustering of metallic catalysts during electrochemical CO2 reduction. *Nature communications* **9**, 1-9 (2018).

72   Zhao, Y. *et al.* Surface reconstruction of ultrathin palladium nanosheets during electrocatalytic CO2 reduction. *Angewandte Chemie* **132**, 21677-21682 (2020).

73   Avanesian, T. *et al.* Quantitative and atomic-scale view of CO-induced Pt nanoparticle surface reconstruction at saturation coverage via DFT calculations coupled with in situ TEM and IR. *Journal of the American Chemical Society* **139**, 4551-4558 (2017).

74   Wu, H. *et al.* Mapping and Controlling Liquid Layer Thickness in Liquid-Phase (Scanning) Transmission Electron Microscopy. *Small Methods* **5**, 2001287 (2021).

75   Larsen, A. H. *et al.* The atomic simulation environment—a Python library for working with atoms. *Journal of Physics: Condensed Matter* **29**, 273002 (2017).

76   Kuhl, K. P., Cave, E. R., Abram, D. N. & Jaramillo, T. F. New insights into the electrochemical reduction of carbon dioxide on metallic copper surfaces. *Energy & Environmental Science* **5**, 7050-7059 (2012).

77   Mortensen, J. J., Hansen, L. B. & Jacobsen, K. W. Real-space grid implementation of the projector augmented wave method. *Physical Review B* **71**, 035109 (2005).

78   Enkovaara, J. *et al.* Electronic structure calculations with GPAW: a real-space implementation of the projector augmented-wave method. *Journal of physics: Condensed matter* **22**, 253202 (2010).

79   Wellendorff, J. *et al.* Density functionals for surface science: Exchange-correlation model development with Bayesian error estimation. *Physical Review B* **85**, 235149 (2012).

80   Held, A. & Walter, M. Simplified continuum solvent model with a smooth cavity based on volumetric data. *The Journal of Chemical Physics* **141**, 174108 (2014).

81   Bondi, A. v. van der Waals volumes and radii. *The Journal of physical chemistry* **68**, 441-451 (1964).

82   Boes, J. R., Mamun, O., Winther, K. & Bligaard, T. Graph theory approach to high-throughput surface adsorption structure generation. *The Journal of Physical Chemistry A* **123**, 2281-2285 (2019).

83   Henkelman, G., Uberuaga, B. P. & Jónsson, H. A climbing image nudged elastic band method for finding saddle points and minimum energy paths. *The Journal of chemical physics* **113**, 9901-9904 (2000).

84   Lindgren, P., Kastlunger, G. & Peterson, A. A. Scaled and dynamic optimizations of nudged elastic bands. *Journal of chemical theory and computation* **15**, 5787-5793 (2019).

85   Ge, A. *et al.* On the coupling of electron transfer to proton transfer at electrified interfaces. *Journal of the American Chemical Society* **142**, 11829-11834 (2020).

86   Peterson, A. A., Abild-Pedersen, F., Studt, F., Rossmeisl, J. & Nørskov, J. K. How copper catalyzes the electroreduction of carbon dioxide into hydrocarbon fuels. *Energy & Environmental Science* **3**, 1311-1315 (2010).

87   Studt, F., Abild-Pedersen, F., Varley, J. B. & Nørskov, J. K. CO and CO2 hydrogenation to methanol calculated using the BEEF-vdW functional. *Catalysis letters* **143**, 71-73 (2013).

A.2 Paper II

Quantifying and Optimizing Electric Field Enhancement Effect on Carbon Dioxide Electroreduction

Junyu Ge[†], Oliver Wischmann Siig[†], Yang Yang, Liying Deng, See Wee Koh, Sudarshan Vijay, Manlin Luo, Xingli Wang, Donguk Nam, Georg Kastlunger, Hong Li
[†]*equal contribution*

To be submitted

Quantifying and Optimizing Electric Field Enhancement Effect on Carbon Dioxide Electroreduction

Junyu Ge,[1,6]† Oliver Wischmann Siig,[2]† Yang Yang, Liying Deng,[4] See Wee Koh,[1] Sudarshan Vijay,[2] Manlin Luo,[5] Xingli Wang,[5,6] Donguk Nam,[5] Georg Kastlunger,[2]* Hong Li[1,5,6]*

[1]School of Mechanical and Aerospace Engineering, Nanyang Technological University, Singapore 639798, Singapore

[2]CatTheory, Physics Department, Denmark Technical University, Kongens Lyngby 2800, Denmark

[4]College of Physics and Information Engineering, Institute of Micro-Nano Devices and Solar Cells, Fuzhou University, Fuzhou, 350108, China

[5]School of Electrical and Electronic Engineering, Nanyang Technological University, Singapore 639798, Singapore

[6]CINTRA CNRS/NTU/THALES, UMI 3288, Research Techno Plaza, 637553, Singapore

† equal contribution

*corresponding authors. geokast@dtu.dk; ehongli@ntu.edu.sg

Abstract

The enhancement of electrochemical carbon dioxide reduction reaction (CO_2RR) by concentrated electric field has been suggested in the past and reported, however, a quantitative study of electric field enhancement effect is lacking due to the paramount challenge in controlling the uniformity of electric field on catalyst surface. Herein, we (semi)quantify the electric field enhancement effect on the surface of ordered array of gold (Au) nanowires/nanoneedles made by an ultrasonic nanoimprinting technique followed by chemical etching, which results in uniform ordered gold nanostructures in a large area. Significant increases in ECSA normalized CO_2RR activity (64.7%) are observed when nanowire/nanoneedle diameter is decreased from 200 to sub-10 nm, although the largest enhancement occurs on the etched samples where steps/defects are introduced. Owing to the electric field-dependent electrochemical surface area, current density can be re-normalized by physical roughness factor to provide a precise estimate of the intrinsic activity of nanowires/nanoneedles that are thinner than 20 nm, where the electric field-enhancement is highest. Operando surface-enhanced Raman spectra reveals 7.4 cm^{-1} redshift of $v_1 CO_3^{2-}$ peaks when nanowire/nanoneedle diameter decreases to sub-10 nm, suggesting either an electric field enhancement or a site-density/coverage effect on a microscopic level. Complementary theoretical study decouples the contributions of concentrated electric field and relative site activities, both through continuum and *ab-initio* models and suggests that the steps/kinks are the active sites and it is changes in the site density of these sites, due to etching, that is the main contributor to the enhanced activity while electric field enhancements are very limited within the considered size ranges. Our work sheds light on the role of surface electric field in CO_2RR by a (semi)quantitative investigation, also suggests the route for further optimization of intrinsic activity of CO_2RR catalysts beyond Au.

Introduction

Electric field is able to change the energy landscape of a chemical reaction, similar to the roles of temperature and pressure in a chemical reaction. Electric field represents an emerging tool to promote catalysis in various chemical reactions.[1-6] For instance, in enzyme catalysis, it has been widely accepted that the electrostatic field from the protein environment stabilizes transition state species and intermediates at the active sites of enzyme.[6] As an important CO_2 transformation method for sustainable carbon recycling, CO_2RR has been widely studied owing to its environmental friendliness and good compatibility with other renewable energy.[7-10] Previous theoretical studies revealed that the electric fields, which appear "naturally" at the electrochemical interface following changes in potential, drive $*CO_2$ adsorption, the rate limiting step for CO_2RR to CO on Au, and that tuning these electric fields through e.g. cation size can lead to improvements in activity.[4,11] However, fundamental challenges remain to achieve high CO_2RR efficiency[12], including high overpotential,[13,14] poor catalytic activity[15,16] and low CO_2 concentration in the surroundings of catalysts.[17]

Sargent et al. recently proposed that on high curvature surfaces, a strong local field can be created without external electrical field. This field can promote CO_2RR by adsorbing potassium ions (K^+) on sharp nanoneedle electrodes, and the concentrated K^+ increase local CO_2 concentration[2]. This interpretation was based on the observation of significant activity increases between different structures although the effect varies for different metals. The possibility of taking advantage of such unique properties calls for a well-defined platform to quantify the enhancement effect and decouple it from other potential effects across different geometries. Nevertheless, such an electric field enhancement effect[2,18] can be effectively extended to CO_2 reduction to formate.[19] In principle, electric field at a given potential should primarily depend on the physical dimension of the nanoneedle. However, the synthesized nanoneedles via chemical routes has a large range of dimensions, and highly porous geometry resulting in significant mass transport limitation. Therefore, it is challenging to quantify electric field contribution on such catalysts and decouple it from other local or non-local effects despite the high activities of CO_2RR observed.

Herein, we strive to quantify the contribution of electric field in CO_2RR on a model system of ordered Au nanowire/nanoneedle vertical arrays made by a physical molding process (room-temperature nanoimprinting), which retains the polycrystalline nature of Au foil in Au nanowire/nanoneedle. When the diameter is below 30-nm, chemical etching is employed to further decrease the dimensions of the nanowires/nanoneedles. As such, the dimensions of Au nanowires/nanoneedles can be controllably decreased to sub-10 nm with well-defined topology. The lengths of the nanowires/nanoneedles are kept short to avoid mass transport limitation that

could significantly affect the activity of CO_2RR[22]. With this method, we can retain a similar surface morphology across different systems, while gradually varying the width of the nanowires/nanoneedles. Thus, we can focus solely on the effect of the nanowires' curvature, potentially responsible for field enhancements of activity. We do observe a slight increase in the electrochemical surface area (ECSA)-corrected CO_2RR activity upon reducing the nanowire width and more substantial increase upon creating the nanoneedles. To evaluate whether an enhanced local electric field is responsible for this increased activity we apply a combination of continuum modeling and density functional theory (DFT). Our simulations indicate that a field enhancement leading to significant activity increases is not achieved at the length scales of the nanoneedles. Therefore, the increase in activity can rather be attributed to an increase in (undercoordinated) active site density upon etching the samples. Our study reveals that local field enhancement by means of surface morphology optimization is challenging and should not be confused with atomistic enhancements due to the creation of surface steps.

Results and discussion

Ordered vertically aligned arrays of Au nanowires are fabricated in a nanoimprinting process (Figure S1). Briefly, an anodic aluminum oxide (AAO) mold was used to imprint Au nanowires on the surface of an Au foil (see Figure S2a for an untreated Au foil) using an ultrasonic embossing tool.[20] Scanning electron microscope (SEM) images of the as-imprinted Au nanowire arrays shows well-defined structure uniformly distributed across a large area (Figure 1), which offers a model system to study the electric field effect that solely depends on the dimension of nanowires.
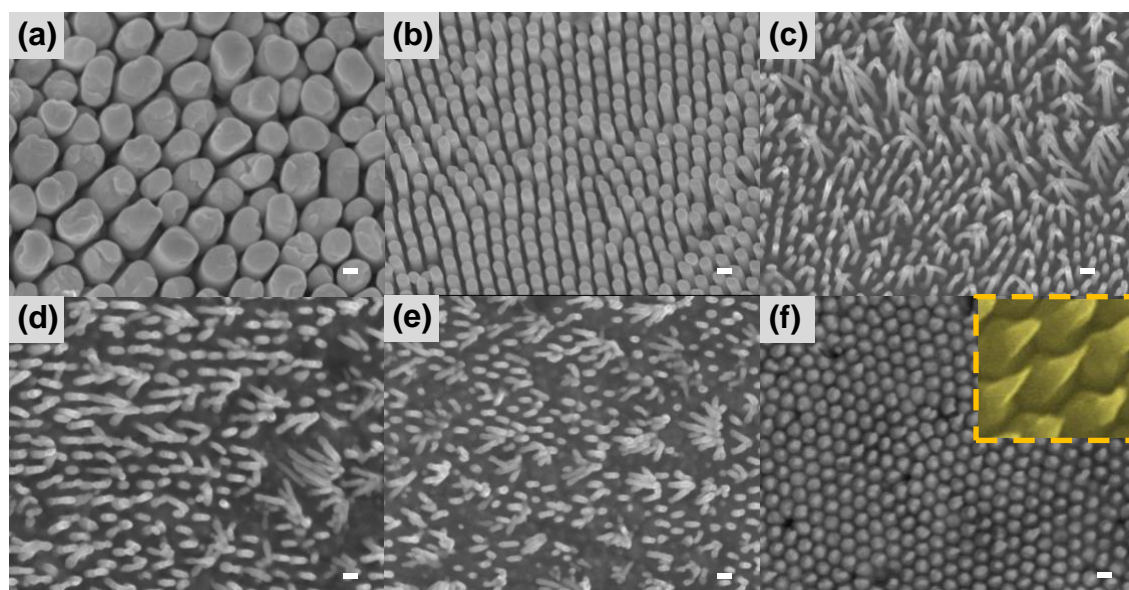

Figure 1 Surface morphologies of obtained Au nanowires. The diameter of nanowires from (a) to (f) are 200nm, 100nm, 30nm, 20nm,10nm, respectively. (f) is AuNN. inset of (f): zoom-in image of the nanoneedles. (d) to (f) Au nanowires and AuNN after etching of Au_30 for 3s, 5s, 7s in gold etchant, respectively. Scale bars, 100nm (a-f)

Moreover, the fabricated Au nanowires are directly rooted in the Au foil, resulting in negligible interface resistance. High-resolution transmission electron microscopy (TEM) (Figure S3) shows the polycrystalline nature of the nanowire inherited from the polycrystalline Au foil; indicating that the catalytic active sites on Au nanowires should be comparable to those on Au foil, which reduces the influence of enhanced active site densities on the measured total activity. The diameter of the nanowires can be easily controlled by the nanopore sizes in AAO mold, which is a commercial product with excellent uniformity in pore dimension. The thinnest nanowires that can be obtained using this imprinting method without compromising uniformity has a diameter of 30 nm. In order to further decrease the diameter of the Au nanowires from nanowire to nanoneedle, Au etchant was employed (Figure S2d-f). X-ray photoelectron spectroscopy (XPS) shows only Au^0 peaks on the etched sample (Figure S4), suggesting the chemical composition of the Au nanowire after etching remains unchanged. X-Ray diffraction (XRD) spectra also suggest the good crystallinity (face center cubic phase) of the as-imprinted nanowires was retained after etching (Figure S5). The length of the nanowires is kept small (~200 nm) to avoid the limited mass transport on catalyst surface. The short length of the nanowire also facilitates the easy demolding process (without AAO etching).
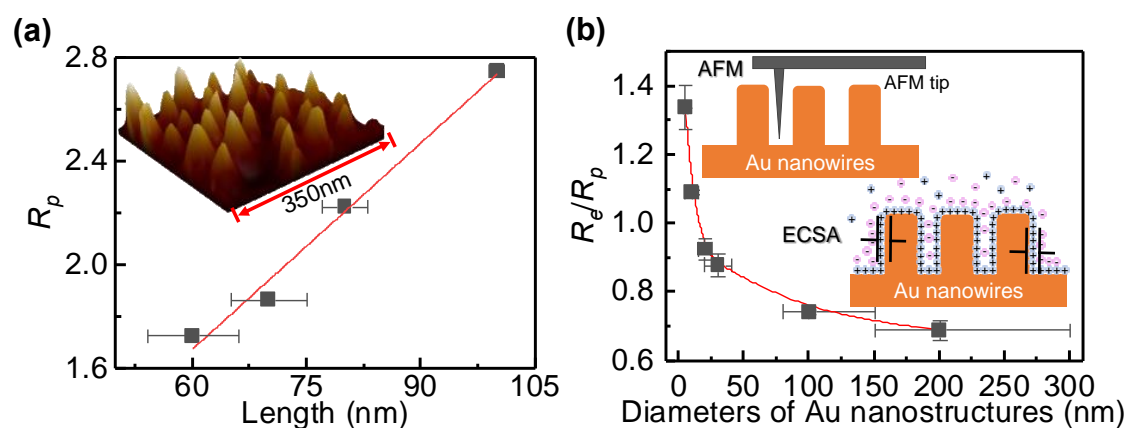

Figure 2 Computed electronic field and physical roughness factor. (a) Calibration line of physical roughness factor on Au_100, with an insert of an AFM image of AuNN. (b) Ratio of electrochemical roughness factor and physical roughness factor.

We measured the double-layer capacitance to obtain ECSA values, in order to obtain electrochemical roughness factor R_e that is calculated by normalizing the ECSA values of Au nanowire/nanoneedle samples to that of Au foil (See Methods and Figures S9-S15). However, validating the ECSA obtained from double layer capacitance measurements could be affected by the concentrated electric field, as it is based on ion absorption on unit catalyst surface area.[21] Thus, we propose an alternative estimate of physical surface area, R_p, obtained by atomic force

5

microscopy (AFM), which is independent of electric field. By normalizing the physical surface area with the projected geometric area, R_p can provide a fair basis for accessing intrinsic activity. However, the actual R_p of the sample is challenging to measure directly because AFM tip is not able to reach the lowest point, i.e., the valley among nanowires, on the nanowire catalyst though supersharp AFM tip is used here, because the inter-nanowire distance depends on the thickness of the nanowalls (about 100-nm-thick) of AAO mold. Thus, initially the AFM images of the nanowires made using the same type of AAO mode (i.e., same average diameter) but different lengths were obtained (see the insert in Figure 2a for the nanoneedle sample, and Figure S6 for other samples). Then, the measured R_p values were plotted against the lengths of the nanowires with the same average diameters, as illustrated in Figure 2a, where the measured R_p values of Au nanowires with average diameter of 100 nm is presented. The R_p value of the actual nanowire catalyst was then derived by extrapolating the linear curve of R_P versus nanowire length to the actual nanowire length (see Figure S8 and Table S1), which is measured by SEM (Figure S2). This approach of fitting R_p for the nanowire structures naturally bares uncertainty, but it serves as a viable benchmark for the ECSA estimates via R_e. Assuming both approaches give access to the true ECSA, the ratio of Re and Rp approaches one. As R_e can be overestimated due to changes in the field, on the other hand, this ratio should increase with the field enhancement. As we show in Figure 2b, we found that R_e/R_p is consistently <1 except for 10nm wide nanowires and etched nanoneedles, meaning that we either underestimate R_e or overestimate R_p at intermediate nanowire radii. R_e/R_p reaches about 1.3 for the sub-10 nm sample. Nevertheless, as the two estimates are generally close (ratio going from around 0.7 to 1.3), they give us a probable range for the "true" surface area, while the trend indicates that the sub-30-nm samples are somehow structurally different from the other samples.

The CO_2 reduction activities of Au samples were measured in CO_2-saturated 0.5 M potassium bicarbonate ($KHCO_3$) with pH of 7.2, as depicted in Figure 3 and Figure S16, where the carbon monoxide (CO) product was quantified using gas chromatography. The maximum Faradaic efficiency (FE) for CO production was found to be over 70% in all samples we have studied, as shown in Figure 3a. This comparison also indicates that selectivity of nanowires/nanoneedles are not significantly affected by short (~200 nm) nanowire diameters/densities, which rules out the influence of different mass transport limitation on various nanowires/nanoneedles. The CO partial current densities at -0.6 V vs. reversible hydrogen electrode (RHE) were firstly normalized to R_e, i.e., j_{CO_Re}, as shown in Figure 3b. All the measured samples fell into three groups on the plot, i.e., Au foil, as-imprinted samples (Au_200, Au_100, Au_30), and etched samples (Au_20, Au_10, and AuNN). The sharp current density increase from Au foil to the as-imprinted samples can be attributed to the higher surface roughness of the as-imprinted sample, which is beneficial for CO_2RR over hydrogen evolution reaction due to their different

6

mass transport responses to surface morphology, *i.e.*, more porous surface increases FE of CO_2RR[22,23]. This is consistent with the higher FE_{CO} (85.5% for Au_200 vs 68.6% for Au foil) observed in Figure 3a. Moreover, the kinetics of the CO2RR also increases greatly as shown in Figure 3c, where the Tafel slopes of the cylinders are significantly lower than that of Au foil (120 mV dec^{-1}). In contrast, the current densities and Tafel slopes of various as-imprinted sample remain similar despite the large difference of their diameters (from 200 to 30 nm). Such small variations of current density and Tafel slope suggest that the as-imprinted samples have similar activity and kinetics, originated from similar types of active sites and rate determining steps (RDS). Notably, another current density leap is seen from as-imprinted sample to the etched samples. The current density remains similar for etched samples despite their very different diameters of 20, 10 and sub-10 nm. Moreover, the Tafel slope at low current density generally decreases with nanorod diameter combined with a reduction in onset potential (-0.4V--0.2V) across the samples. A consistent change in Tafel slope appears upon increasing the overpotential for every system but the foil, particularly clear for the samples with an onset potential around -0.2V. It has been suggested previously that different kinetic regions exist, with CO production being limited by a PCET step (to form *COOH) at very low overpotentials, followed by a region limited by CO_2 adsorption at intermediate potentials, until finally a region limited by mass transport limitations.[24,25] The Tafel slopes and changes in slope for the low overpotential data present in this study would be consistent with this hypothesis.
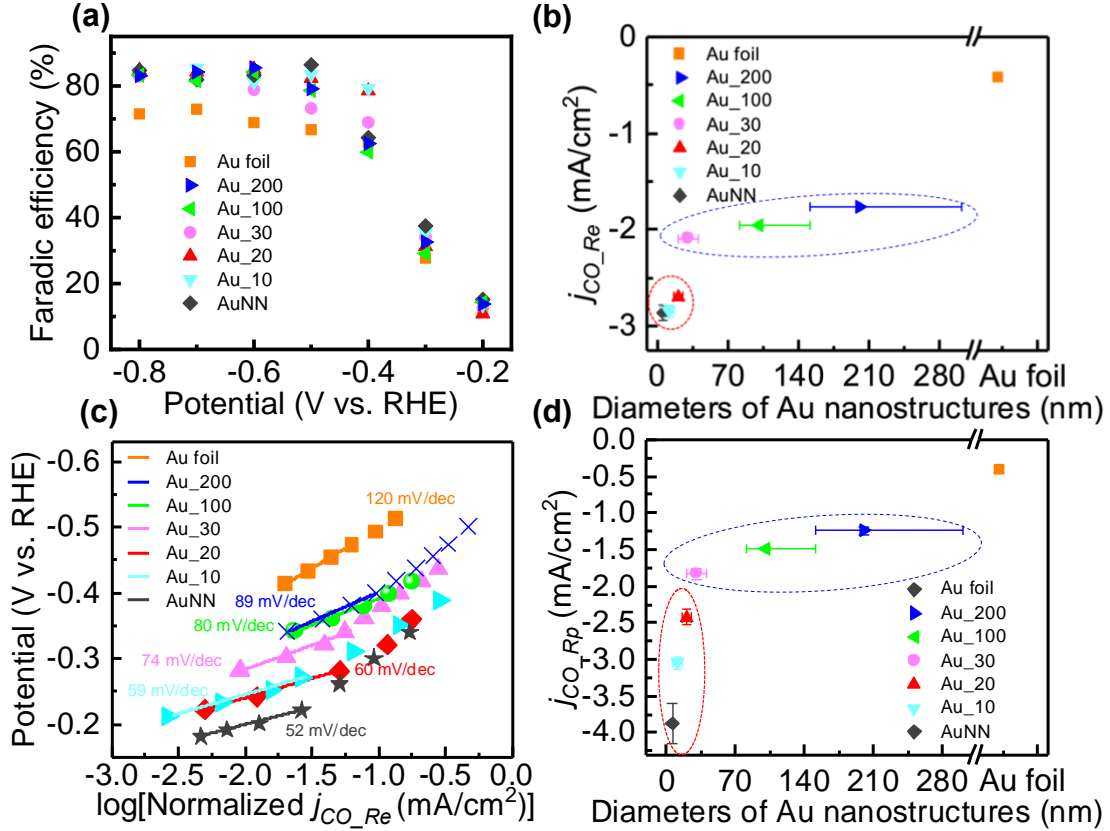
Figure 3 Electrochemical performance. (a) Faradaic efficiency of Au samples. (b) CO partial current density at -0.6 V vs. RHE normalized to electrochemical roughness factor. (c) Tafel slope normalized to electrochemical roughness factor. (d) CO partial current density at -0.6 V vs. RHE normalized to physical roughness factor. Each current density value in b, c, d was obtained by averaging the data from 3 different tests (see Table S2). The red and blue dashed circles in b, d indicate etched and unetched samples respectively.

The current density normalized via Rp, i.e., j_{co_Rp}, presented in Figure 3d, revealed the same qualitative trends as j_{co_Re}; (1) all the samples can be grouped into categories, i.e., Au foil, as-imprinted samples (Au_200, Au_100, Au_30), and etched samples (Au_20, Au_10, and AuNN) based on their locations in the plot; (2) there are obvious current density leaps from one group to the other; and (3) there are small differences among the as-imprinted samples. As the R_p estimates are lower for the etched samples (Table S1), we now also observe differences among these, as delineated by the red dashed oval in Figure 3d. Specifically, j_{co_Rp} increases from 2.4 to 3.9 mA/cm^2 when nanowire/nanoneedle diameter decreases from 20 nm to sub-10 nm, corresponding to roughly 60% increase in activity across the etched samples. This tuned activity could be the result of an enhancement of the electric field. However, it may also be a result of the synthesis process itself, at the activity appears to change abruptly once etching is introduced.

In order to confirm or exclude higher a higher density of active sites after etching. The surface of the etched samples are examined by TEM, as displayed in Figure 4. Obvious pits (yellow dashed curves) appear on the surface of etched samples including Au nanoneedle (Figure 4a and Figure S17) and nanowires (Figure 4b). Such pits are not observed to the same extent on

8

the as-imprinted Au nanowires that have a much more uniform and smooth surface (Figure 4c), suggesting that the as-imprinted samples have great crystallinity inherited from Au foil. A typical face-centered cubic (FCC) structure can be seen on all nanowires with plane spacings of 2.35 and 2.04 Å corresponding to facet (111) and (200), respectively, as depicted in both FFT spots (inset of Figure 4d) and high-resolution TEM (HRTEM) images (Figure 4d-f). When focusing on the pit area on the surface, stepped facets, beside facet (111) and (200), can be observed, as delineated by the red arrows in Figure 4d and 4e. In contrast, the kinked or stepped facets are not observed on large parts of the as-imprinted Au nanowire (Figure 4f). We note that, that lead deposition experiments have shown, that even on highly ordered surfaces, even the small numbers of "defects" in the form of kinks or steps are still overwhelmingly responsible for the CO_2 reduction activity on Au facets.[26] The much higher current density in both Figure 3b and 3d are attributed to an increase in the availability of these stepped facets and kinks, as will be discussed later.
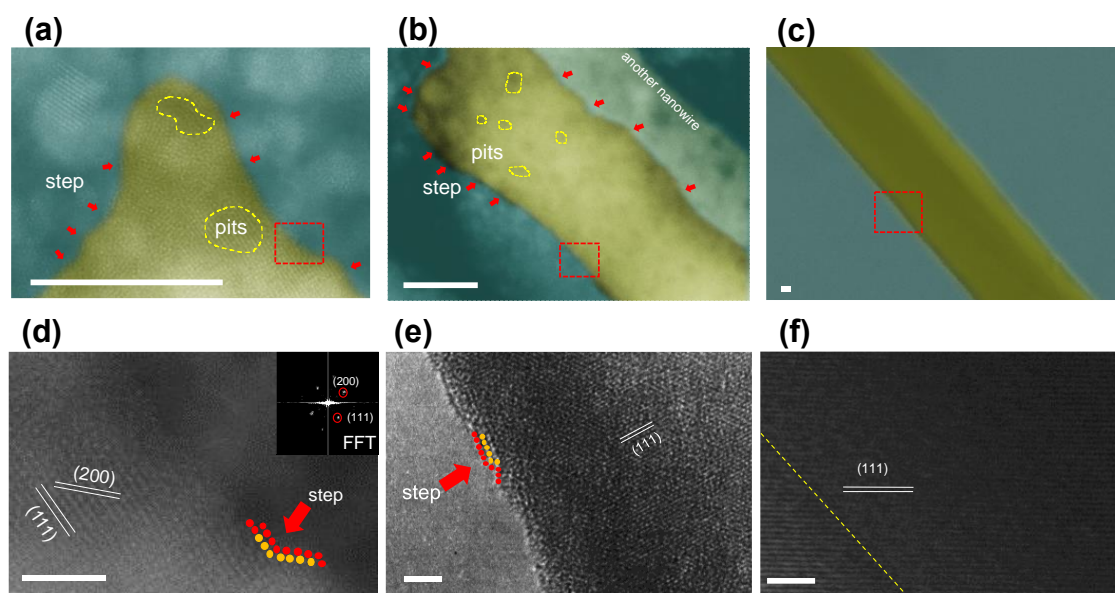

Figure 4 The microstructure characterization. (a-b) ADF-STEM image of Au nanoneedle and etched Au_20. (c) TEM image of Au_100. (d-f) High-resolution TEM images of AuNN, Au_20 and Au_100 surfaces respectively. Scale bars, 10nm (a-c) and 2nm (d-f).

To further verify the role of a concentrated electric field on a microscopic level, we employed *in situ* surface enhanced Raman spectroscopy (SERS), as depicted in Figure 5a and Figure S18. Briefly, the Au nanostructure electrode was assembled into a customized single chamber cell as a working electrode. Raman signal was collected to monitor the CO_2RR process when negative potentials were applied on the working electrode (See Methods for details). The changes in the local electric field can be reflected in the peak position of chemically absorbed carbonate (ν_s CO_3^{2-} at ~1065 cm^{-1}), which has previously been identified on copper during CO_2RR, probably stemming from the bicarbonate buffer (Figure 5b and Figure S19).[27] In our

case, the peak can be only observed when applying a potential of -0.4 V vs. RHE or lower, as depicted in Figure S18. Redshift to lower wavelength is observed when the diameter of the nanowires/nanoneedles decreases. Such a redshift is similar to the earlier report where redshift of this peak was seen when the applied potential increased and it was attributed in part to increased electric field in double-layer and in part to changes in the coverage of carbonate (dipole-dipole interactions)[27,28]. A redshift of ~7.7 cm^{-1}/V was observed on the 100-nm-thick Au nanowires, measuring the peak shift from -0.4 to -1.0 V vs RHE. In the copper study mentioned, changes in the dipole-dipole interactions appeared as the main contributor to the peak shift, when cathodic of the PZC (~7 cm^{-1}/V vs. ~5 cm^{-1}/V for the field effect). The two have not however been decoupled here. Across the different structures a redshift ~7.4 cm^{-1} was observed when comparing Au nanoneedles with 200-nm-thick Au nanowires kept at the same potential (Figure 5c). Notably, the trend in the peak shift does match the activity enhancements observed under the same applied potential. The observed Raman shift once again suggests that either of two effects are present, or a combination of the two; coverage effects and/or intrinsic enhancement of the electric field. If we assume the peak shift is entirely due to the enhanced electric field, the redshift of ~7.4 cm^{-1} this is equivalent to the field enhancement of a 1 V change in potential. As *CO$_2$, the RDS below -0.4 V vs. RHE, responds strongly to field, we would expect field enhancements of this size to translate into an improvement in the binding of 0.3-0.4 eV (see *ab-initio* calculations below of details). Such an enhancement would translate into 3-4 orders of magnitude increase in activity assuming it follows Arrhenius' law, which is much larger than the activity enhancements observed here. Alternatively, dipole-dipole interactions has been shown to lead to similar sized redshifts both on Cu with SERS[29] and for sulfate on Au with SEIRAS.[30] Looking at the trend in Figure 5c, it is noticeable that the redshift is larger for the etched samples. If we attribute the redshift to dipole-dipole interactions, this would mean that the etched samples have a lower carbonate coverage, as lower coverage weakens the dipole-dipole interactions, thus lowering their collective vibrational frequency. By etching the samples, we are changing the distribution of flat/stepped/defect sites which might in itself lead to intrinsically poorer chemisorption of carbonate (or better), while the improved binding of *CO$_2$ may further limit the carbonate coverage, both of which would lead to a redshift of the peak relative to the unetched samples. Once again our results suggest that there are multiple simultaneous effects convoluting the trends in activity, and while we may have enhanced the field slightly by increasing the curvature, the main contribution to the activity increases comes from changes in the surface morphology, i.e. active site density.
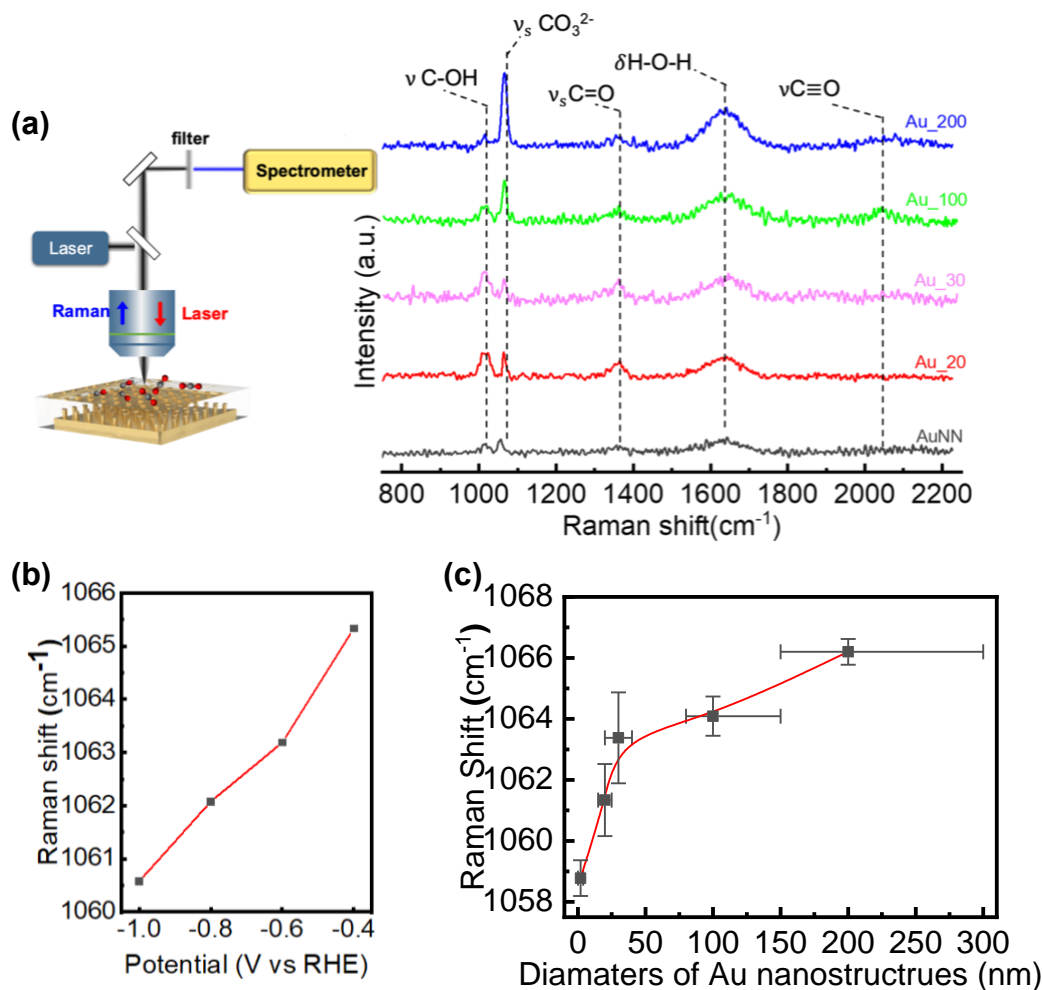
Figure 5 Raman spectra. (a) Raman schematic and spectra on Au samples. (b) Raman shift of 1066 cm^{-1} peak on Au_100 sample at varying potential. (c) Raman shift of 1066 cm^{-1} peak on Au samples at -0.6 V vs RHE.

The electric fields of Au nanowires with various diameters were calculated from COMSOL Multiphysics,[2] as displayed in Figure 6a (See also Figure S6). The electric field strength is inversely proportional to the diameter of the nanowire. However, significant electric field enhancement is observed only when the diameter is below 2-4 nm, i.e., corresponding to about 10% activity increase from 200 to 4 nm, a further 11% from 4 nm to 2 nm and ultimately below 2 nm, a >450% increase can be observed at 0.2 nm, relative to the activity of the 200 nm rod. It is worth noting that the activity increases are exponentially dependent on the field enhancement, and translating the increases into activity increases, we find that the actual field enhancements calculated are all essentially negligible, compared to potential-induced changes for instance, except for the 0.2 nm system. However, we stress that the 0.2 nm result is only included to illustrate the length scales necessary to achieve significant enhancement, as it would essentially correspond to a single-atom string of gold atoms (the Au-Au distance of bulk Au is around 0.3 nm).
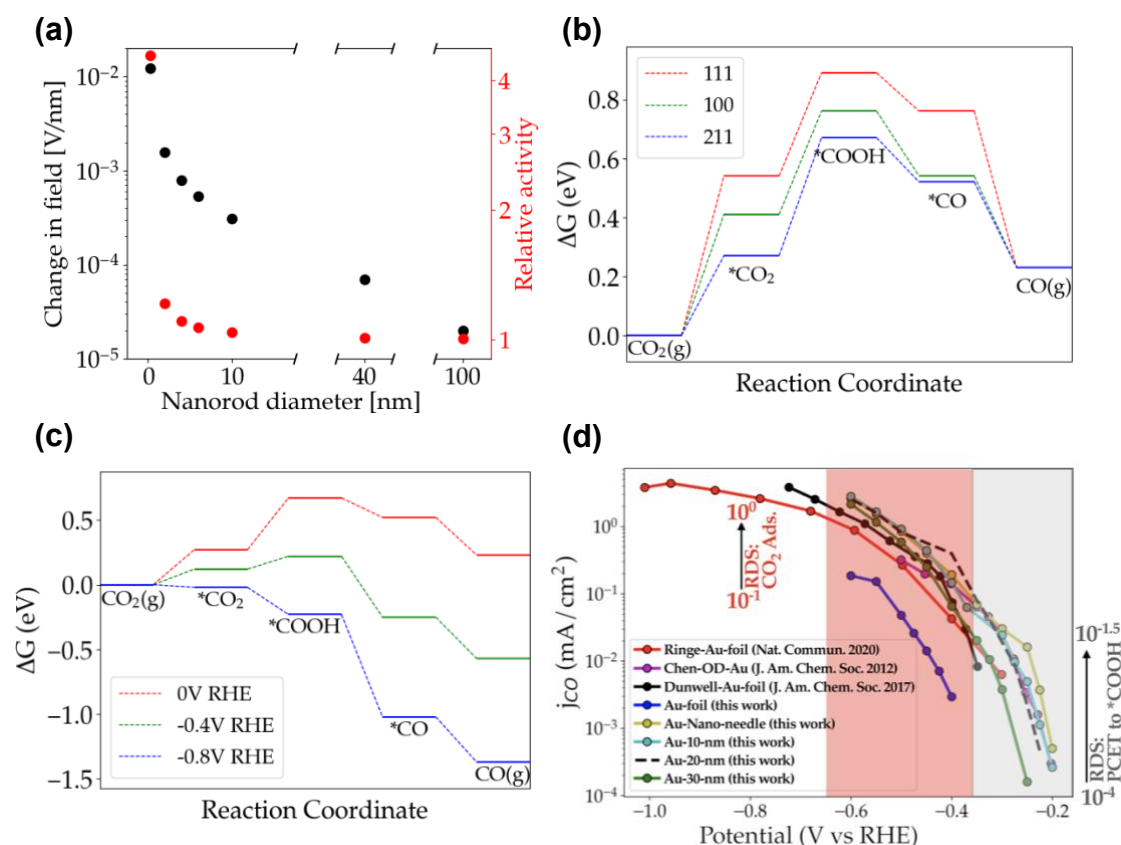
Figure 6 Modeling of electric field and active sites. (a) Changes in the electronic field on the surface of the Au structures relative to the field on the Au foil, along with their respective relative activities (b) Free energy diagram for the reaction of CO_2 to CO on Au, for the 111, 100 and 211 facets at 0V vs. RHE. (c) Free energy diagram for the reaction of CO_2 to CO on Au(211) at varying potential vs. RHE. (d) Comparison of ECSA normalized partial current densities towards CO for this study and several other experimental studies, including other attempts to nanostructure gold. Data from Ringe et. al[25], Chen et. al[13] and Dunwell et. al[38].

Next, in order to understand the implications of the surface morphology changes, we obtain more insight on the activity, active sites as well as rate determining step(s) through density functional theory (DFT) calculations. As CO was the major product for most of the potential range across all samples studied, we focused on the pathway towards CO, and compared for a range of different facets. Specifically, the reaction energetics were studied on the two most dominant facets, (111) and (100), along with the (211) facet as a proxy for the stepped and kinked defects introduced. As the free energy diagram in Figure 6b shows, the *CO_2 and *COOH are substantially stabilized on the stepped (211)-surface. From the FED's, we observe that the RDS is predicted to be *COOH formation at low reducing potentials, until a switch of RDS to *CO_2 adsorption happens around −0.4 V vs RHE. Additionally, it is worth noting that the only intermediate that exhibits a significant response to changes in potential due to changes in the interfacial field is *CO_2 with a potential response of 0.36 eV/V. *COOH and *CO do exhibit potential responses of 1.12 eV/V and 1.93 eV/V, but here the main contribution is the destabilization of the proton-electron pair with negative potentials, while the response to a change in electric field only amounts to 0.12 eV/V and -0.07 eV/V for *COOH and *CO,

12

respectively. Consequently, even if any field enhancement did occur across the nanorods, the effect should be small for any CO_2 reduction where the formation of *COOH is the RDS. At overpotentials where the formation of *CO_2 is the RDS, the effect should be much more pronounced. This does not seem to be the case, regardless of whether the change in RDS is determined based on the FED energetics or Tafel analysis of Figure 6d, which shows an apparent change in Tafel slope at potentials slightly less cathodic than −0.4 V vs. RHE. Additionally, what we can ultimately deduce from Figure 6c, which shows the data of this study plotted together with ECSA normalized CO production currents for other select studies, is that the activities of all four studies are quite close. Even with distinctly different synthesis methods for high curvature structures (this study) as well as oxygen-derived structures (Cheng et. al), suggesting that the intrinsic enhancement is largely absent. What can also be observed however, is the absence of detailed probing of the low overpotential regime of CO production (−0.2 to −0.4 V vs RHE) available in the literature, where this study offers a unique insight into this region, confirming the hypothesis from theory that there is indeed a region where CO_2R on gold is limited by the formation of *COOH.

Conclusion

Ordered vertical Au nanowire arrays were fabricated by room-temperature nanoimprinting, which retains the similar crystallinity and thus surface properties of nanowire as that of the starting Au foil. Such a platform offers a model system to investigate the role of concentrated electric field on CO_2RR activity. Au etching further decreases the feature size of nanowires and amplifies the enhancement effects of concentrated electric field on CO_2RR, while simultaneously increasing the site density of the active stepped sites. Two different approaches were employed to access intrinsic CO_2 activity; ECSA as well as physical surface area obtained by AFM. These both yielded similar roughness factors and thus same qualitative trends. The intrinsic activity does increase with reduced nanorod diameter, particularly below the 30 nm samples where etching is employed. The results of these particular rods are however convoluted, as the etching method introduced to reduce the diameter below 30 nm introduces a significant increase in the density of stepped defects/sites. As shown with DFT, (211) step sites are significantly more active than the flat (111) and (100) sites, and coupled with continuum modeling of the electric field, it seems that the former is the major driver of the increased activity observed. Steps and kinks introduced by Au etching optimize the activity of Au nanoneedle, as verified by DFT calculations. Crucially, this study is able to thoroughly probe the low overpotential region of CO_2R on gold, which reveals that the reaction undergoes a change in RDS going from low to intermediate overpotentials. The activity enhancement however, seems to be largely similar across the potential range investigated, which again

indicates that the field enhancement is in fact not the main contributor to the activity enhancement, as different potential regions should exhibit markedly different field responses based on changes in the RDS. This insight can be leveraged in future studies of potential field effects, to deconvolute the effect from others by probing and measuring the activity response in regions that exhibit different responses to the electric field. With this work, we shed light on the elusive role of concentrated electric field on CO_2RR, which could be applicable on catalysts beyond Au and reactions beyond CO_2RR.

Experiments and methods

Materials Preparation

Gold nanowires were prepared through an ultrasonic nanoimprinting method we previously reported. Gold foils with the purity of 99.99% were washed by immersion and sonication for 15min in acetone, isopropyl alcohol, ethanol and deionized water, sequentially. The AAO template and one piece of washed Au foil were placed in the ultrasonic nanoimprinting machine. 20 nm-Au nanowires, 10nm-Au nanowires, and Au nanoneedles were prepared by etching 30 nm-Au-nanowires in gold etchant (Sigma) for 3 sec, 5 sec and 7 sec, respectively.

Material characterization

All SEM images were obtained using a JEOL 7600F instrument. TEM images were obtained by JEOL-2100F, Japan. The structural characteristics of samples were measured by X-ray diffraction at room temperature on a Paralytical Xpert Pro instrument. Compositions were investigated by Kratos Axis Supra. Park System NX10 was used to obtain AFM images. Raman spectroscopy was carried out on a WITec CRM200 confocal Raman microscopy system with the excitation line of 633 nm and an air-cooling charge-coupled device (CCD) as the detector.

Electrochemical Measurements

Electrochemical experiments were conducted in a customized H-cell, separated by an ion exchange membrane (AMV from AGS, Japan). Certain amounts of $KHCO_3$ (99.7%, Sigma-Aldrich) were dissolved in Millipore water (18.2 MΩ cm) to prepare the 0.5 M electrolyte. A pre-electrocatalysis process was conducted for 24 h to remove contaminants in the electrolyte. Before reaction, the electrolyte was purged continuously with CO_2 for 30 min. A Pt wire (Sigma-Aldrich, 99.99%) was used as counter electrode and Ag/AgCl as reference electrode.

For product analysis, CO_2 reduction experiments were started by a chronoamperometric step applied by a BioLogic VMP3 workstation. After 30 min of electrocatalysis at a constant potential, a sample of gas was analyzed by gas chromatography (Agilent 7890B) to detect the products.

Physical roughness factor measurement

AFM (Park System NX 10) was employed to obtain the surface topography of the samples. Since the inter-nanowire distances are very small due to the ultrathin nanowalls of AAO mold (100-nm-thick for AAO with 200nm-wide pores, and 35-nm-thick for AAO with 100 nm or smaller diameter pores.), it is impossible to reach the valley between nanowires on the as-imprinted sample with height of ~200 nm. We thus used the high-aspect ratio tip with 125 μm

length and >10:1 aspect ratio (NanoWorld, AR10-NCHR-3) to obtain the most accurate topography possible. A typical resonant frequency of ~287 kHz, and tapping mode were used to get 1 μm by 1 μm AFM images. All scans on the samples were performed under a constant amplitude (50 nm) and a low scan rate (1 Hz).

Electrochemical roughness factor measurement

Double-layer capacitances of Au samples were measured at potential windows with no faraday reactions occur in 0.5 M Argon-purged potassium chloride (KCl) aqueous solution. The scan rates are set as 5, 20, 40, 60, 80, 100 mV/s. The slope of linear fitting result is the double layer capacitance of each sample. After dividing the double layer capacitance by the value of Au foil measured in this work, the electrochemical roughness factor could be obtained.

COMSOL Multiphysics simulations

To study the charge behavior at Au nanowires, electric field and current density were simulated with COMSOL. The electric field was modeled as the gradient $\nabla\varphi$ of the electrostatic potential φ which was found using Poisson's equation. In cylindrical 1D coordinates this is given as:

$$\frac{1}{r}\frac{\partial}{\partial r}\left(r\frac{\partial\phi}{\partial r}\right) = \frac{\kappa^2}{e\cdot\beta}\cdot\sinh(e\cdot\beta\cdot\phi)$$

With r being the cylinder radius, e being the elementary charge, β the thermodynamic temperature $1/(k_BT)$, where k_B is the Boltzmann constant and T the temperature. κ is the inverse Debye length given as $\kappa = \sqrt{\frac{2\cdot e^2\cdot n\cdot\beta}{\epsilon}}$, with n being the number density and ϵ being the permittivity, in this case of water.

It was implicitly assumed from this 1D cylinder model that the cylinder was infinite and uniform such that $\phi(r,\theta,z) \approx \phi(r)$. The model calculated the potential/field on the surface of the side of the cylinder. Additionally, a set of boundary conditions were required to solve the system. Trivially, it was assumed that the electric field in the bulk is constant, referenced as 0:

$$\lim_{r\to\infty}\phi(r) = \phi^0 = 0$$

Furthermore, the total capacitance of the double layer separating the surface and the bulk was split into two components, c_H, for the Helmholtz layer, and c_{GC} for the Gouy Chapman (or *diffuse*) layer with $c_H = \frac{d\sigma}{d(\phi^m-\phi^\ddagger)}$ and $c_{GC} = \frac{d\sigma}{d(\phi^\ddagger-\phi^0)}$. σ is the surface change density and $\phi^m, \phi^\ddagger$ is the potential of the metal and at the reaction plane respectively.

Using Gauss' law $\sigma(r) = \lim_{r\to R}\epsilon\frac{d\phi(r)}{dr}$ and assuming a constant Helmholtz capacitance c_H, a

16

Robin boundary condition emerges on the surface of the cylinder[31]:

$$\lim_{r \to R} \epsilon \frac{d\phi(r)}{dr} = c_H\left((\phi^m - \phi^{pzc}) - (\phi(R) - \phi^0)\right)$$

This allowed us to iteratively solve for the potential as a function of the radial distance numerically, with the following assumptions:

- $z \to \infty$; infinite length, $\therefore$ no z-component
- $\phi^{pzc} = 0.4\, V$; PZC of gold
- $c_H = 20\, \mu F/cm^2$; constant Helmholtz/Stern layer capacitance
- Adequately separated rods; $\therefore$ no overlapping fields
- No diffusion limitations

Finally, the field was found from the gradient of the potential at $r = R$, at -0.6 V vs. RHE.

Next, in order to convert the field to an adsorption energy, we need to know how the electrostatics of the system relates to the energetics/activity. This has been quantified from fitting a parabola to a range of formation energies of *CO_2 (ΔE) on (211) at varying surface charge densities (σ):[24]

$$\Delta E_\sigma = \Delta E_{\sigma=0} + \Delta a_\sigma \cdot \sigma + \Delta b_\sigma \cdot \sigma^2$$

$$\Delta E_\sigma = 0.74\text{eV} + 2.98 \cdot 10^{-2} \frac{cm^2}{\mu C \cdot eV} \cdot \sigma - 2.87 \cdot 10^{-4} \left(\frac{cm^2}{\mu C \cdot eV}\right)^2 \cdot \sigma^2$$

We can directly relate the field to the surface charge density through Gauss' law above. Additionally, we can relate activity to energetics, assuming it follows an Arrhenius Relationship:

$$k = A e^{\frac{-E_A}{k_b T}}$$

Where k is the rate constant, E_A the activation energy and A the pre-exponential factor. As we are interested specifically in any activity *enhancements*, we can calculate the rate of a cylinder with radius "i" relative to that of the foil ("∞ radius cylinder"):

$$k_{rel,i} = \frac{k_i}{k_\infty} = \frac{A_i e^{\frac{-E_{A,i}}{k_b T}}}{A_\infty e^{\frac{-E_{A,\infty}}{k_b T}}} \approx e^{\frac{E_{A,\infty} - E_{A,i}}{k_b T}}$$

Assuming that the pre-factors are similar, i.e., $A_i \approx A_\infty$, which includes the assumption that the adsorbates are similar in structure and as a result has largely the same change in entropy.

Now, if we assume that the adsorption barrier is low, such that $E_A \approx \Delta E$, we can relate the relative rate to ΔE_σ and thus the field through σ:

$$k_{rel,i} \approx e^{\frac{\Delta E_{\sigma(\infty)} - \Delta E_{\sigma(i)}}{k_b T}}$$

DFT simulation details

The energetics reported in this paper are all calculated using GPAW,[32,33] using the Solvated

Jellium Method (SJM)[34] to get constant-potential free energies. The systems were all optimized on a real-space grid with a grid-spacing of 0.18 Å. The exchange-correlation contributions were approximated using the BEEF-vdW functional.[35] All surface calculations employed periodic boundary conditions in the xy-plane and a dipole correction in the z-direction perpendicular to the surface. 3 x 4 x 4 unit cells with the two bottom layers fixed were used for all facets. Monkhorst-Pack k-point grids of 5 x 3 x 1 and 4 x 3 x 1 were applied for the 211 and the other facets respectively. A 0.1 eV / k_B Fermi smearing was used. Forces were converged to 0.03 eV / Å. SJM uses an effective potential cavity solvation model implemented into GPAW by Held and Walter.[36] The parameters used were: Bondi's van der Waals radii [37] multiplied by a factor of 1.1 following a benchmark of the capacitance to 20 μF/cm². Strength of the repulsion at the atomic radii controlling the cavity size, u0=0.18eV, surface tension 0.001148 Pa*m (Both taken from[36]), (maximal) dielectric constant (ϵ) of 78.36 and temperature of 298.15 K. The counter charge in SJM was chosen as a 2.5 Å thick jellium slab at z=25 Å in each unit cell. The tolerance for the electrode potential deviation from target potential was set to 10mV.

Operando SERS measurement

The CO_2RR on Au nanowires/nanoneedles was performed in a customized single chamber cell filled with 0.5M $KHCO_3$ for operando SERS measurements. Before measurements, CO_2 was continuously bubbled into the electrolyte for 30 min. The wavelength of the excitation laser was 633 nm, and Raman shift was calibrated by using a silicon wafer. Each Raman spectrum was recorded with three accumulations over an acquisition time for 30 s.

Reference

1   Aragonès, A. C. *et al.* Electrostatic catalysis of a Diels–Alder reaction. *Nature* **531**, 88-91, doi:10.1038/nature16989

http://www.nature.com/nature/journal/v531/n7592/abs/nature16989.html#supplementary-information (2016).

2   Liu, M. *et al.* Enhanced electrocatalytic CO_2 reduction via field-induced reagent concentration. *Nature* **537**, 382-386, doi:10.1038/nature19060 (2016).

3   Gorin, C. F., Beh, E. S. & Kanan, M. W. An Electric Field–Induced Change in the Selectivity of a Metal Oxide–Catalyzed Epoxide Rearrangement. *Journal of the American Chemical Society* **134**, 186-189, doi:10.1021/ja210365j (2012).

4   Chen, L. D., Urushihara, M., Chan, K. & Nørskov, J. K. Electric Field Effects in Electrochemical CO_2 Reduction. *ACS Catalysis* **6**, 7133-7139, doi:10.1021/acscatal.6b02299 (2016).

5   Clark, M. L. *et al.* CO_2 Reduction Catalysts on Gold Electrode Surfaces Influenced by Large Electric Fields. *J Am Chem Soc* **140**, 17643-17655, doi:10.1021/jacs.8b09852 (2018).

6   Fried, S. D. & Boxer, S. G. Electric Fields and Enzyme Catalysis. *Annu Rev Biochem* **86**, 387-415, doi:10.1146/annurev-biochem-061516-044432 (2017).

7   Liu, S. *et al.* Shape-Dependent Electrocatalytic Reduction of CO_2 to CO on Triangular Silver Nanoplates. *J Am Chem Soc* **139**, 2160-2163, doi:10.1021/jacs.6b12103 (2017).

8   Zhang, L., Zhao, Z.-J. & Gong, J. Nanostructured Materials for Heterogeneous Electrocatalytic CO_2Reduction and their Related Reaction Mechanisms. *Angewandte Chemie International Edition* **56**, 11326-11353, doi:10.1002/anie.201612214 (2017).

9   Zhu, W. *et al.* Active and selective conversion of CO_2 to CO on ultrathin Au nanowires. *J Am Chem Soc* **136**, 16132-16135, doi:10.1021/ja5095099 (2014).

10   Ge, J. *et al.* Vertical Silver@Silver Chloride Core–Shell Nanowire Array for Carbon Dioxide Electroreduction. *ACS Applied Energy Materials* **2**, 6163-6169, doi:10.1021/acsaem.9b01286 (2019).

11   Sandberg, R. B., Montoya, J. H., Chan, K. & Nørskov, J. K. CO-CO coupling on Cu facets: Coverage, strain and field effects. *Surface Science* **654**, 56-62, doi:http://dx.doi.org/10.1016/j.susc.2016.08.006 (2016).

12   Li, Q. *et al.* Tuning Sn-Catalysis for Electrochemical Reduction of CO_2 to CO via the Core/Shell Cu/SnO_2 Structure. *Journal of the American Chemical Society* **139**, 4290-4293, doi:10.1021/jacs.7b00261 (2017).

13   Chen, Y., Li, C. W. & Kanan, M. W. Aqueous CO_2 reduction at very low overpotential on oxide-derived Au nanoparticles. *J Am Chem Soc* **134**, 19969-19972, doi:10.1021/ja309317u (2012).

14   Kahsay, A. W. *et al.* Selective and Low Overpotential Electrochemical CO_2 Reduction to Formate on CuS Decorated CuO Heterostructure. *Catalysis Letters* **149**, 860-869, doi:10.1007/s10562-019-02657-2 (2019).

15   Grills, D. C. *et al.* Electrocatalytic CO_2 Reduction with a Homogeneous Catalyst in Ionic Liquid: High Catalytic Activity at Low Overpotential. *J Phys Chem Lett* **5**, 2033-2038, doi:10.1021/jz500759x (2014).

16   Liu, A. *et al.* Current progress in electrocatalytic carbon dioxide reduction to fuels on heterogeneous catalysts. *Journal of Materials Chemistry A* **8**, 3541-3562, doi:10.1039/c9ta11966c (2020).

17   Wagner, A., Sahm, C. D. & Reisner, E. Towards molecular understanding of local chemical environment effects in electro- and photocatalytic CO_2 reduction. *Nature Catalysis*, doi:10.1038/s41929-020-00512-x (2020).

18   Saberi Safaei, T. *et al.* High-Density Nanosharp Microstructures Enable Efficient CO2

Electroreduction. *Nano Letters* **16**, 7224-7228, doi:10.1021/acs.nanolett.6b03615 (2016).

19   Zheng, X. *et al.* Sulfur-Modulated Tin Sites Enable Highly Selective Electrochemical Reduction of CO₂ to Formate. *Joule* **1**, 794-805, doi:10.1016/j.joule.2017.09.014.

20   Junyu Ge , B. D., Shuai Hou , Manlin Luo , Donguk Nam , Prof. Hongwei Duan , Prof. Huajian Gao , Prof. Yee Cheong Lam. Rapid Fabrication of Complex Nanostructures using Room-Temperature Ultrasonic Nanoimprinting. (2020).

21   Connor, P., Schuch, J., Kaiser, B. & Jaegermann, W. The Determination of Electrochemical Active Surface Area and Specific Capacity Revisited for the System MnOx as an Oxygen Evolution Catalyst. *Zeitschrift für Physikalische Chemie* **234**, 979-994, doi:doi:10.1515/zpch-2019-1514 (2020).

22   Hall, A. S., Yoon, Y., Wuttig, A. & Surendranath, Y. Mesostructure-Induced Selectivity in CO2 Reduction Catalysis. *Journal of the American Chemical Society* **137**, 14834-14837, doi:10.1021/jacs.5b08259 (2015).

23   Yu, Q. *et al.* Morphology controlling of silver by plasma engineering for electrocatalytic carbon dioxide reduction. *Journal of Power Sources* **453**, 227846, doi:https://doi.org/10.1016/j.jpowsour.2020.227846 (2020).

24   Ringe, S. *et al.* Double layer charging driven carbon dioxide adsorption limits the rate of electrochemical carbon dioxide reduction on Gold. *Nature Communications* **11**, 33, doi:10.1038/s41467-019-13777-z (2020).

25   Vijay, S. *et al.* Unified mechanistic understanding of CO2 reduction to CO on transition metal and single atom catalysts. *Nature Catalysis* **4**, 1024-1031, doi:10.1038/s41929-021-00705-y (2021).

26   Mezzavilla, S., Horch, S., Stephens, I. E., Seger, B. & Chorkendorff, I. Structure sensitivity in the electrocatalytic reduction of CO2 with gold catalysts. *Angewandte Chemie International Edition* **58**, 3774-3778 (2019).

27   Chernyshova, I. V., Somasundaran, P. & Ponnurangam, S. On the origin of the elusive first intermediate of CO2 electroreduction. *Proc Natl Acad Sci U S A* **115**, E9261-E9270, doi:10.1073/pnas.1802256115 (2018).

28   Iwasita, T., Rodes, A. & Pastor, E. Vibrational spectroscopy of carbonate adsorbed on Pt(111) and Pt(110) single-crystal electrodes. *Journal of Electroanalytical Chemistry* **383**, 181-189, doi:https://doi.org/10.1016/0022-0728(94)03708-B (1995).

29   Chernyshova, I. V., Somasundaran, P. & Ponnurangam, S. On the origin of the elusive first intermediate of CO(2) electroreduction. *Proc Natl Acad Sci U S A* **115**, E9261-e9270, doi:10.1073/pnas.1802256115 (2018).

30   Pfisterer, J. H. K., Zhumaev, U. E., Cheuquepan, W., Feliu, J. M. & Domke, K. F. Stark effect or coverage dependence? Disentangling the EC-SEIRAS vibrational shift of sulfate on Au(111). *The Journal of Chemical Physics* **150**, doi:10.1063/1.5047941 (2018).

31   Chan, K. & Eikerling, M. A Pore-Scale Model of Oxygen Reduction in Ionomer-Free Catalyst Layers of PEFCs. *Journal of The Electrochemical Society* **158**, B18, doi:10.1149/1.3505042 (2011).

32   Mortensen, J. J., Hansen, L. B. & Jacobsen, K. W. Real-space grid implementation of the projector augmented wave method. *Physical Review B* **71**, 035109, doi:10.1103/PhysRevB.71.035109 (2005).

33   Enkovaara, J. *et al.* Electronic structure calculations with GPAW: a real-space implementation of the projector augmented-wave method. *Journal of Physics: Condensed Matter* **22**, 253202, doi:10.1088/0953-8984/22/25/253202 (2010).

34   Kastlunger, G., Lindgren, P. & Peterson, A. A. Controlled-Potential Simulation of Elementary Electrochemical Reactions: Proton Discharge on Metal Surfaces. *The Journal of Physical Chemistry C* **122**, 12771-12781, doi:10.1021/acs.jpcc.8b02465 (2018).

35   Wellendorff, J. *et al.* Density functionals for surface science: Exchange-correlation

model development with Bayesian error estimation. *Physical Review B* **85**, 235149, doi:10.1103/PhysRevB.85.235149 (2012).

36   Held, A. & Walter, M. Simplified continuum solvent model with a smooth cavity based on volumetric data. *The Journal of Chemical Physics* **141**, doi:10.1063/1.4900838 (2014).

37   Bondi, A. v. van der Waals volumes and radii. *The Journal of physical chemistry* **68**, 441-451 (1964).

38   Dunwell, M. *et. al.* The Central Role of Bicarbonate in the Electrochemical Reduction of Carbon Dioxide on Gold. *Journal of the American Chemical Society* **139**, 3774-3783, doi:10.1021/jacs.6b13287 (2017).